SCIENTIFIC REPORTS

OPEN

Single-Molecule 3D Images of "Hole-Hole" IgG1 Homodimers by Individual-Particle Electron Tomography

Received: 13 February 2018
Accepted: 30 May 2019
Published online: 20 June 2019

Dongsheng Lei[1], Jianfang Liu[1], Hongbin Liu[2], Thomas E. Cleveland IV[3], John P. Marino[3], Ming Lei[2] & Gang Ren[1]

The engineering of immunoglobulin-G molecules (IgGs) is of wide interest for improving therapeutics, for example by modulating the activity or multiplexing the specificity of IgGs to recognize more than one antigen. Optimization of engineered IgG requires knowledge of three-dimensional (3D) structure of synthetic IgG. However, due to flexible nature of the molecules, their structural characterization is challenging. Here, we use our reported individual-particle electron tomography (IPET) method with optimized negative-staining (OpNS) for direct 3D reconstruction of individual IgG hole-hole homodimer molecules. The hole-hole homodimer is an undesired variant generated during the production of a bispecific antibody using the knob-into-hole heterodimer technology. A total of 64 IPET 3D density maps at ~15 Å resolutions were reconstructed from 64 individual molecules, revealing 64 unique conformations. In addition to the known Y-shaped conformation, we also observed an unusual X-shaped conformation. The 3D structure of the X-shaped conformation contributes to our understanding of the structural details of the interaction between two heavy chains in the Fc domain. The IPET approach, as an orthogonal technique to characterize the 3D structure of therapeutic antibodies, provides insight into the 3D structural variety and dynamics of heterogeneous IgG molecules.

Immunoglobulin-G molecules (IgGs) are the predominant component of humoral immunity. In clinical practice, recombinant IgGs have been used to treat a wide array of diseases, including cancer[1–3], rheumatoid arthritis[4–6], and many auto-immune diseases[7–10]. Recently, advances in IgG engineering have enabled the development of monoclonal antibodies with the potential to recognize more than one antigen, such as bispecific and multi-specific antibodies[11–13]. Among them, bispecific antibodies are being evaluated for the treatment of cancer through activation of T-cell killing[14–16] and potential reduction of the non-target toxicities of loaded antibodies such as antibody-drug conjugates (ADCs)[17,18]. Over the past 20 years, many platforms have been designed and evolved to produce bispecific IgG, such as strand-exchange engineered domain (SEED)[19], electrostatic steering[20], IgG4 Fab-arm exchange[21], Diabodies[22], and CovX-Bodies[23,24]. However, the main challenge remains to improve the yield of heterodimer and suppress homodimerization. One approach to address this challenge is the "knob-into-holes" system that involves a "knob" mutation (T366W) in one-half of the Fc C_H3 domain and "hole" mutations (T366S, L368A and Y407V) in the other half. This system promotes hetero-dimerization through the pairing of the "knob" and the "hole". Thus far, this system has been successfully implemented in the production and purification of several therapeutic bispecific antibodies at various clinical stages[25,26].

The main variants generated from this system are hole-hole homodimers and, to a lesser extent, knob-knob homodimers, which are both product-related impurities and should be mostly removed through assembly and purification steps. To evaluate the performance of the purification, the levels of these homodimers were monitored. These homodimers showed unexpected behavior not normally observed in conventional monoclonal IgG antibodies (mAbs)[27], such as a pH-dependent interchange between several peaks, which were separated

[1]The Molecular Foundry, Lawrence Berkeley National Laboratory, Berkeley, CA, 94720, USA. [2]Protein Analytical Chemistry, Genentech Inc., South San Francisco, CA, 94080, USA. [3]Institute for Bioscience and Biotechnology Research, National Institute of Standards and Technology and the University of Maryland, Rockville, MD, 20850, USA. Correspondence and requests for materials should be addressed to M.L. (email: lei.ming@gene.com) or G.R. (email: gren@lbl.gov)

on hydrophobic interaction chromatography and represented different forms of the hole-hole homodimer with the same mass[27]. The unexpected behavior of the hole-hole homodimers are related to the mutations in the C_H3 domain and challenge the development of suitable analytical methods to monitor and understand the difference in the homodimer forms. Therefore, various modes of chromatography, native mass spectrometry (MS) and hydrogen-deuterium exchange MS (HDX-MS) were used to identify the structural basis for the pH-dependent interchange of the hole-hole homodimer forms[27]. The analytical results indicate that higher-order structure-related changes are responsible for the different hole-hole homodimer forms. The HDX-MS data showed a local increase in deuterium exchange in the C_H2 and C_H3 regions, but understanding its impact on the overall conformation of the homodimer will require further study. Additional higher-order structure differences that were not observed by HDX-MS may remain to be discovered.

The traditional methods used to determine the three-dimensional (3D) structure of proteins include X-ray crystallography and nuclear magnetic resonance (NMR) spectroscopy. Each method has certain disadvantages: flexible molecules such as IgGs are difficult to crystallize and IgGs are also too large to be amenable to *de novo* NMR structural determination. In recent years, single particle cryo-electron microscopy (cryo-EM) has become an important technique to determine the averaged 3D structure of a type of protein[28,29].

Single particle cryo-EM now has the capability for structure determination of protein at atomic resolution under near-native buffer conditions[30]. However, this method also has its own limitations, such as difficulties in imaging small proteins (<50 kDa) and in achieving low-resolution 3D maps of flexible macromolecules. These flexible macromolecules include DNA and RNA, lipoprotein, antibodies[31] and human immunodeficiency virus among many others. The problem for imaging using this technique originates from the averaging concept, in which the tens of thousands and more atoms within each particle are assumed to have identical arrangements. This assumption is largely suitable for rigid particles but becomes less so with increasing conformational flexibility and dynamics. Averaging over hundreds of thousands of particles can often cause anisotropic resolution[32] and the loss of domains[28] in the final 3D reconstruction, although other portions of the molecule may show atomic resolution. Moreover, even in cryo-EM, sample preparation artifacts can be present. The thin water film used for cryo-EM specimens can often cause proteins to adopt a preferred orientation in the ice, which can be unduly influenced by the air-water interface[33]. In addition, the air-water interface can induce proteins to denature or aggregate, and complexes to dissociate[34]. In comparison, although negative staining (NS) remains useful as a supplementary method to study small and flexible proteins at a low-resolution, but with high contrast. Some disadvantages of NS remain, such as stain artifacts, complex dissociation, stain-induced chemical reactions and substrate interaction. Therefore, no sample preparation method is perfect.

Preliminary NS-EM 2D images showed that the hole-hole homodimers are heterogeneous in structure[27]. Unlike in the conventional Y-shaped conformation, it was observed that in some particles, the C_H2 and C_H3 domains of the Fc of the homodimers were distant from each other[27], displaying an "X-shaped" conformation. However, geometric analysis based on these 2D images was insufficient to uncover the detailed 3D structure or the extent of the structural flexibility.

To obtain the 3D structure of the hole-hole homodimers, the optimized negative-staining (OpNS)[35–38] method was used to prepare the EM specimen, and both conventional single-particle class averaging and then the individual-particle electron tomography (IPET) method[24,39,40] was used to obtain the 3D reconstructions. Reconstructing 64 IPET 3D density maps of the IgG hole-hole homodimers at a resolution of ~15 Å were used to derive 64 conformations of the IgG homodimers via flexible docking ("hand-in-glove") of a crystal structure of IgG (PDB entry 1HZH[41]) into the envelope of each IPET 3D density map. Additional statistical analysis on the geometry of the IgG homodimers (domain distance and angle) investigated the conformational variety and flexibility among the domains and provided a mean to quantitatively understand the differences in structural flexibility between a regular antibody and the hole-hole homodimer.

Results

Morphology of IgG hole-hole homodimers. The IgG hole-hole homodimers produced as a side product from the assembly of the knob-into-hole bispecific antibody were examined by OpNS EM (Fig. 1A–D)[35–38]. The OpNS protocol was refined from conventional NS protocols by introducing three additional steps: (i) filtering the thawed staining solution (1% Uranyl formate, UF) using the smallest available filter (0.02 μm) to remove the precipitated particles immediately before usage (the newly prepared 1% UF was aliquoted into 2 mL/vial and stored at −20 °C), (ii) incubating and then staining the EM grid within a black box to prevent the stain reagent from the light-exposure, and (iii) drying the specimen with nitrogen gas to prevent sample oxidation. The OpNS protocol can limit certain artifacts, such as Rouleau formation for lipoprotein particles[35–38], and has been used to examine many biological macromolecules[24,27,35–38,40,42–62], including antibodies[24,27,49,53], cholesteryl ester transfer protein (CETP)[46], phospholipid transfer protein (PLTP)[63], liposome-CETP complex[42], lipoproteins and their antibody complexes[35,38,43,58], GroEL and Proteosome[37], Contactin-associated Protein-like 2 (CNTNAP2)[59], Calsyntenin-3[40], Neurexin 1α[51], 84-base pair dsDNA conjugated with 5 nm nanogold[57], and DNA origami[52]. These studies demonstrate that OpNS is a suitable and reliable protocol to examine the structure and morphology of small, and/or flexible proteins.

OpNS-EM images of the IgG hole-hole homodimer showed evenly distributed particles (Fig. 1A, after band-pass filtering between 8 Å and 2,000 Å). Most particles had a dimension of ~150–190 Å, which is similar to that of regular IgGs[49]. Zoom-in images showed that most particles have a Y-shape (~60.6%) (Fig. 1B). Unexpectedly, many particles (~26.9%) displayed as X-shape (Fig. 1C, Supplementary Video 1), bow-tie shape (~10.0%) or even i-shape (~2.5%) (Fig. 1D). The Y-shaped particles had a similar structure to regular IgGs[49], while the X-shaped particles contained four apparent domains: two large ring-shaped domains and two small rod-shaped domains (Fig. 1E). The two ring-shaped domains, likely to be Fab domains, were similar to each other in size (overall diameter) and shape (aspect ratio). The two small rod-shaped domains were similar to each other and were likely

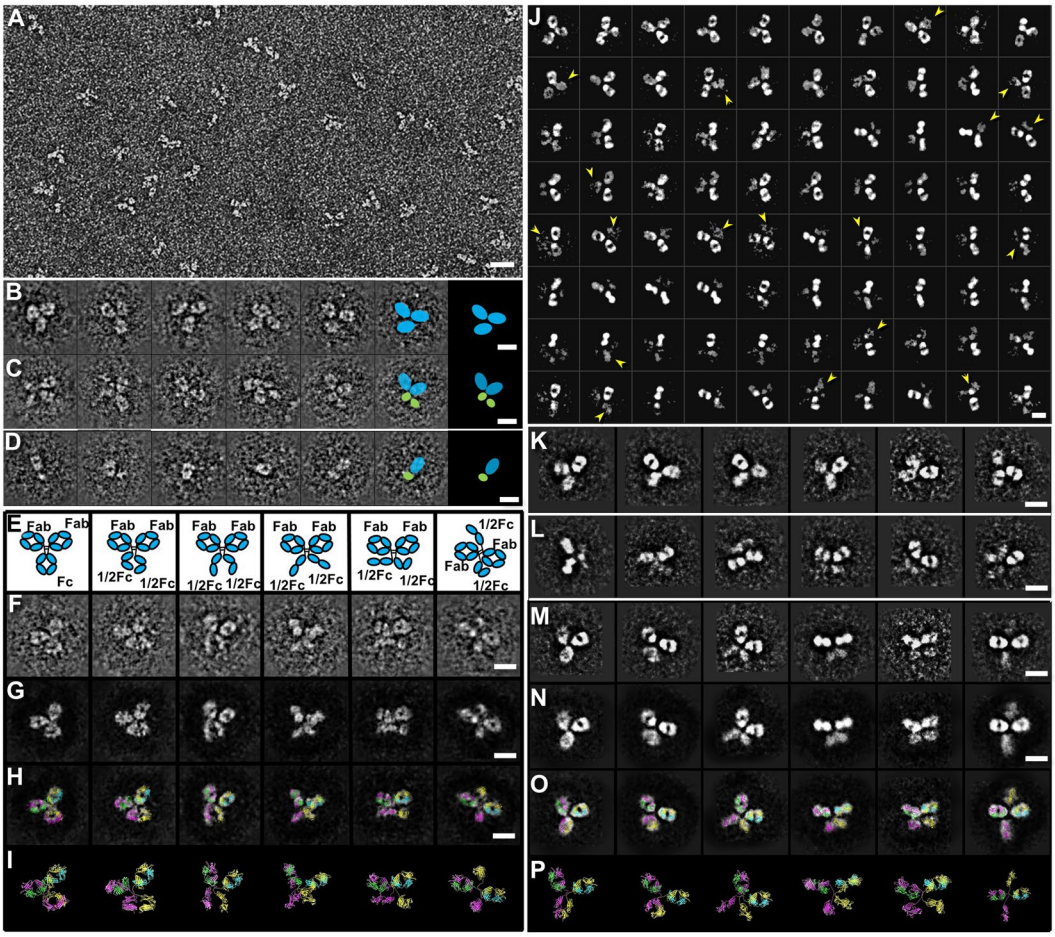

Figure 1. OpNS-EM images of IgG hole-hole homodimer sample. (**A**) A survey OpNS image of the IgG hole-hole homodimer sample. Representative images of (**B**) Y-shaped, (**C**) X-shaped, and (**D**) i-shaped particles are shown. The last images of the Y-, X-, and i-shaped particles were superposed with diagrams to show the overall location of large domains (cyan ellipses) and small regions (green ellipses) within each particle. (**E**) Diagram of various conformations of IgG homodimer. (**F**) Representative raw images showing conformations in (**E**). (**G**) After erasing the noise areas outside particles, (**H**) images were superposed by using an IgG model (crystal structure of regular IgG, PDB entry 1HZH) to show the overall location of domains. (**I**) Obtained models show various conformations of IgG homodimer. All models are shown in ribbon representation, in which heavy chains are in yellow and magenta, and light chains are in cyan and green. (**J**) Representative reference-free class averages from 13,546 particles. Arrows indicate averages with fuzzy or blurry domains (**K**) Representative Y-shaped class averages. (**L**) Representative X-shaped class averages. (**M**) Class averages of Y- and X-shaped particles in various conformations. (**N**) After erasing noise areas outside particles, (**O**) the averages were superposed using the IgG model to show the overall location of Fab, Fc or half Fc domains (detail provided in Methods section). During superposing, the location and orientation of domains within models were required to be adjusted to fit to each average. (**P**) Obtained models show overall conformations of IgG homodimer. Scale bars = 20 nm in A and 10 nm in (**B**–**P**).

the C_H2 and C_H3 domains of the heavy chain, *i.e.*, an Fc domain in which the two heavy chains were separated from each other (Fig. 1E). Two domains of the bow-tie shaped particles have a similar size and shape to each other and Fab domains, while the Fc domain is apparently absent, possibly denatured. The i-shaped particles were similar to half of an X-shaped particle in size and shape, likely composed of a Fab domain and half of an Fc domain (Fig. 1E–I).

To evaluate whether the observed X-shaped particle was statistically significant in its abundance, we performed a reference-free classification based on 13,546 particles. The high-contrast 2D class averages confirmed all Y-shaped, X-shaped, i-shaped and bow-tie shaped particles (Fig. 1J–L). The difference between the Y- and X-shaped particles was within the conformation of the Fc domains, in which one of three domains in the Y-shaped particles converted into two small rod-shaped domains in the X-shaped particles.

The size and shape of domains within Y- and X-shaped class averages were similar to those of an IgG crystal structure (PDB entry 1HZH[41]), except for the split Fc domain of the X-shaped averages. The similarity allowed us to map 3D models to the 2D class averages following methods previously used in EM[64–67] and AFM[68,69]. Although the class averages are insufficient for determining the 3D particle structures, they help us to understand the

overall shape and conformational variety in terms of the domain locations (Fig. 1M–P). During the mapping, we found that no matter how we changed the orientations of the antibody, the projection of the model could not match well with some Y-shaped and all X-shaped averages, unless we adjusted the structure of the hinge region to allow the domains to move and change their orientations. The new locations and orientations allowed us to match the Y-shaped particle easily (Fig. 1M–P, first column). For X-shaped particles, an additional operation was needed; *i.e.*, the two halves of the heavy chains of the Fc domain (two copies of C_H2 and C_H3 domains) must be separated from each other to match to the rod-shaped densities in the 2D averages of the X-shaped particles (Fig. 1M–P, last four columns). The wide range of orientations between the two copies of the C_H2 and C_H3 domains of the Fc suggested that X-shaped particles were more flexible than Y-shaped particles. Similarly, the above mapping method was also applied to the raw images of Y-shaped and X-shaped particles to confirm the flexibilities of particles (Fig. 1F–I).

Evaluation of potential artifacts from NS and substrate interactions using the NISTmAb. Although the OpNS protocol has been used to examine more than 20 types of macromolecules for high-contrast imaging[37,53], one may still question whether the antibody-substrate interaction or the low pH of the uranyl formate NS causes noticeable artifacts. These artifacts could include conformational changes or the domain dissociation observed in the X-shaped particles.

In principle, cryo-EM is the ideal approach to examine the proteins in near-native solution conditions without artifacts from NS. Practically, however, it is very challenging to image the antibody by itself (not antibody-antigen complex) due to its low molecular weight and floppy structure (three relatively isolated ~50 kDa domains linked by a flexible hinge region). Generally, proteins of molecular weight less than 50 kDa are beyond current limitations of cryo-EM structural determination. Although antibodies comprise more than 10% of human plasma proteins, and are highly desired for pharmaceutical drug design, no cryo-EM 3D reconstruction has been reported according to our best knowledge. While cryo-electron tomography (ET) 3D reconstructions have been reported[70,71], no raw data or intermediate results have been shown in the publications. Moreover, one publication using the same approach was retracted due to low reliability (more than 90% of the reconstructions were invalid based on third-party evaluation using IMOD reconstructions)[72,73]. Thus, cryo-EM is still challenging as a practical approach for studying antibody structure. We therefore supported our NS methodology using identical studies of a control antibody.

To examine whether the X-shaped particles were related to artifacts from the NS or substrate interaction, we used the same NS protocol and supporting substrate to examine the NISTmAb, a standard monoclonal antibody provided by National Institute of Standard Technology (NIST), which is available as a reference material (RM 8671)[74]. NISTmAb is an IgG1 antibody performance standard useful for evaluation/development of state-of-the-art and emerging analytical measurement technologies[75,76]. The material has been used extensively to evaluate current best practices for mAb characterization and develop innovative analytical technologies. The survey image showed evenly distributed NISTmAb particles with a "Y" shape with dimensions of ~150–180 Å (Fig. 2A). The particles were composed of three ring-shaped domains of ~55–75 Å in diameter (Fig. 2B), which were similar to those of crystal structures (PDB entry, 1HZH[41]). No X-shaped particle was observed. The reference-free class averages from ~4,961 particles confirmed that a "Y"-shaped structure was the only species in the sample (Fig. 2C). The result was consistent to the early reports; *i.e.*, no X-shaped particles were observed in other IgG samples by using same NS protocol[24,27,37–39]. Although the pH of the staining is as low as ~4.5, which is different from the pH of the samples, it has been reported that UF can fix protein structure within a few milliseconds[77], which may explain the lack of apparent of pH induced artifacts.

Although we could not exclude the possibility that the flexibility of antibodies could be influenced by the substrate interactions, we find it unlikely that the X-shaped antibody was solely an artifact of NS, and conclude that the X-shape is an intrinsic conformation of the hole-hole IgG homodimer. This result is also consistent with multiple orthogonal methods, including chromatography, native MS and HDX-MS[27].

The limitations of conventional single-particle averaging in 3D reconstruction. To understand the detailed structure of the X-shaped particles, a 3D structure was required as projections were often insufficient. Although single-particle class averaging is the dominant technique for 3D structural determination, the method has limitations in the reconstruction of flexible proteins. This is because it requires not only an initial model but also the assumption of identical particles in 3D structure (or at least, a small number of discrete structures)[78]. Using this averaging method, the 3D reconstructions were either significantly dependent on the given initial models or gave structurally impossible solutions[49]. To demonstrate the limitations of single-particle reconstruction on the hole-hole homodimer, we used the EMAN software package[78] for reconstruction. Since the underlying methodology of single-particle reconstruction is similar in other software packages, the phenomenon illustrated in the example is also expected from other software packages.

For 3D reconstruction by single-particle averaging, two types of initial models were used: a cluster of ellipsoids representing domains and a single Gaussian blob representing an entire antibody (Supplementary Fig. S1)[78]. In the domain models, four arrangements of ellipsoids were tried: two models consisted of three ellipsoidal blobs forming a Y-shape with angles of 150° and 45° respectively (Supplementary Fig. S1A, left two); while the other two models consisted of two large and two small ellipsoidal blobs forming an X-shape and cross-shape, respectively (Supplementary Fig. S1A, right two). In the full-antibody models, the initial models consisted of a single featureless ellipsoidal Gaussian blob at four noise levels (Supplementary Fig. S1C).

Through a multi-reference refinement process, the final single-particle 3D reconstructions achieved from the domain models showed domains having similar angles to the initial models (Supplementary Fig. S1B), suggesting an initial model bias. The final 3D reconstructions from the full-antibody models showed significantly different structures from the initial models, but none of them was consistent with the crystal structure (PDB: 1HZH). This

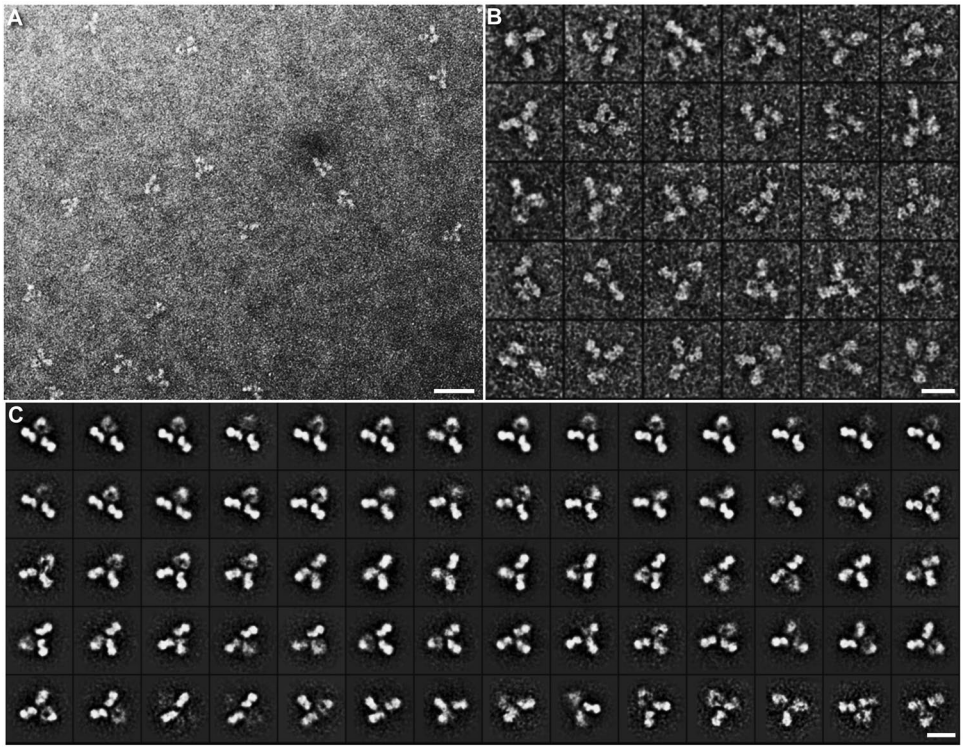

Figure 2. OpNS-EM images of NISTmAb sample. (**A**) A survey OpNS image of NISTmAb sample. (**B**) Representative images of particles, and (**C**) representative class-averages from 4,961 particles. Scale bars = 30 nm in **A**, 10 nm in (**B**,**C**).

result demonstrates the limitations of single-particle 3D reconstruction on flexible proteins is consistent with the problems reported in previous publications on IgG1 molecules[49]. Furthermore, these phenomena are anticipated for single-particle 3D reconstructions regardless of which software packages are used. It has been reported that common artifacts in single-particle 3D reconstruction (averaging) include the presence of blurry domains[79], smaller than the expected dimensions of domains, uneven distribution of resolutions[32], and the absence of protein domains/regions[80], such as two ankyrin repeat regions, which were absent in the atomic structure of TRPV1[28]. Given the limitations of the single-particle averaging reconstruction method in the structural determination of flexible proteins, we studied the hole-hole homodimer using the IPET approach, which has been tested on small and flexible macromolecules[24,39,40,42,49–55,57–59,62].

IPET 3D reconstruction of individual particles. The IPET 3D reconstruction method was used to obtain the 3D map from each individual particle of the X-shaped, Y-shaped and i-shaped isomers (Figs 3 and 4). This method has demonstrated its ability to reconstruct 3D structures of flexible proteins[49,52,57–59], including IgG1[49], peptide-conjugated IgG1[24], cholesteryl ester transfer protein (CETP) bound to lipoprotein[54], and antibody bound to lipoproteins[58,81]. In IPET approach, particles were imaged from a series of tilt angles from −45° to 45° in 1.5° increments by electron tomography (ET) (Fig. 3A). The targeted particle was tracked and selected from each tilt series after contrast transfer function (CTF) correction. Unlike the single-particle 3D reocnstruction (an averaging approach), no initial model was required. The first *ab initio* 3D reconstruction was directly generated from the experimental tilt images via a back-projection algorithm. These tilt images were iteratively aligned to their global centers to achieve a final 3D reconstruction via IPET approach. During the iterative alignment process, automatically generated Gaussian low-pass filters and particle shaped soft-boundary masks were used to reduce the noise. A missing-wedge correction was also applied during the process (see Methods). The step-by-step refinement procedures and intermediate results are shown in Fig. 3B. The final 3D density map showed an overall Y-shaped particle (Fig. 3C) at a resolution of ~13.2 Å (Fig. 3E) based on the Fourier shell correlation (FSC) analysis as described[49].

In the IPET reconstructions, the Y-shaped particle had an overall diameter of ~195 Å, and two of the three domains were similar to each other in size and shape (approximately 90 Å in diameter), suggesting that they were Fab domains. The third domain, which was different from other two domains in size, was likely the Fc domain. This IPET structure was consistent with the IgG crystal structure in overall size, domain shape and domain size, which allowed us to determine the overall particle conformation by flexibly docking the crystal structure (PDB: 1HZH) into the map (details provided in the Methods section). To understand molecular conformation, we used an established method, flexible fitting of the high-resolution crystal structure into the low-resolution EM density map using molecular dynamics[82–89]. Although the docked model could not reveal the atomic resolution structure, it was sufficient to reveal the low-resolution conformation[82,89,90].

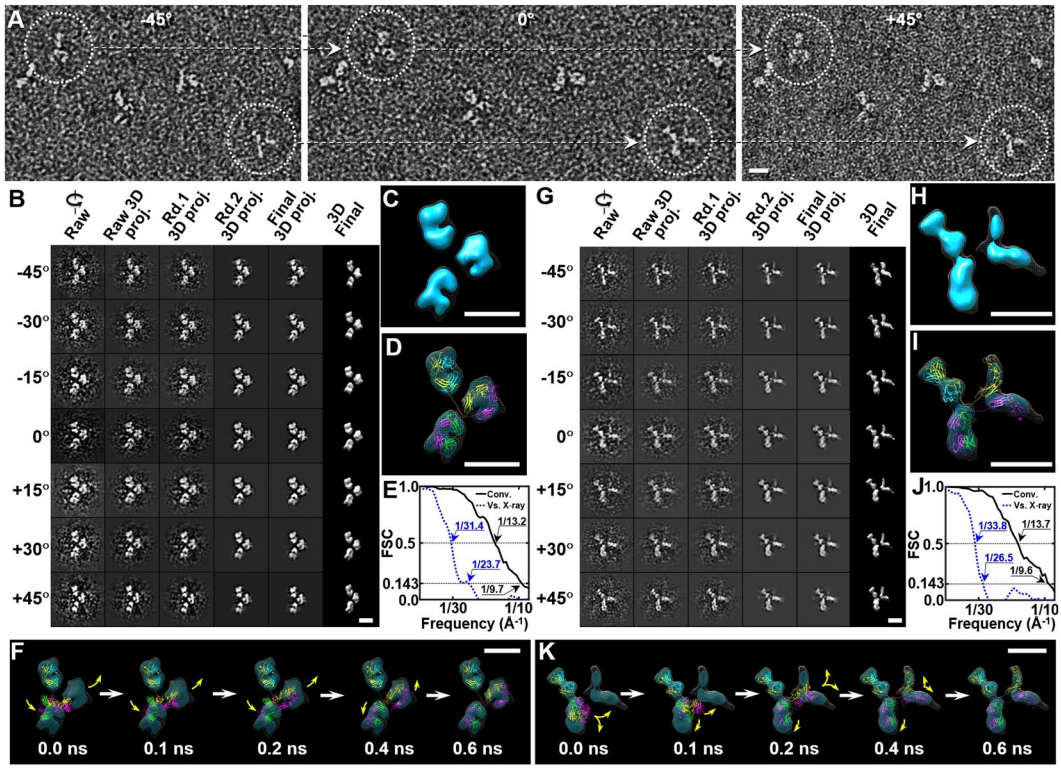

Figure 3. 3D reconstruction of two representative IgG homodimers by IPET. (**A**) OpNS samples of the IgG homodimer were imaged using ET from a series of tilt angles (from −45° to +45° at 1.5° intervals). Two homodimer particles (white circled) with orthogonal views are indicated by linked dashed arrows in three selected ET tilt micrographs. (**B**) Seven representative tilt images of an individual Y-shaped particle are displayed in the first column from the left. Using IPET, the tilt images (after CTF correction) were gradually aligned to a common center for 3D reconstruction via iterative refinement. Projections of raw, intermediate and final 3D reconstructions at corresponding tilt angles are displayed in the next five columns according to their corresponding tilt angles. (**C**) Final IPET 3D density map of targeted individual particle. The density map was low-pass filtered to 20 Å to reduce over-interpretation of high frequency or local noise. The 'hide dust' function was applied by Chimera. (**D**) The final 3D density map was flexibly docked with IgG crystal structure by using TMD simulation. (**E**) The resolution of IPET reconstruction was estimated by two Fourier shell correlation (FSC) curves. The first FSC curve (black solid line) was computed from two 3D maps that were back-projected from two sets of self-aligned tilt images (with even and odd tilt order numbers). The FSC curve fell below 0.5 at ~13.2 Å, and fell below 0.143 at ~9.7 Å. The second FSC curve (blue dash line) was computed from the IPET reconstruction and the atomic resolution density map calculated from the fitted model. The FSC curve fell below 0.5 at ~31.4 Å and 0.143 at ~23.7 Å. (**F**) Five snapshots illustrated the conformational changes of the IgG model during TMD simulation. (**G**–**K**) The 3D density map of a second individual IgG homodimer was reconstructed from the tilt images using IPET. FSC analysis between the reconstructions from odd and even tilt images showed that FSC curve fell below 0.5 at ~13.7 Å and fell below 0.143 at ~9.6 Å (black solid line). The FSC analyses between the IPET final map and the map from the fitting model showed the FSC curve fell below 0.5 at ~33.8 Å and fell below 0.143 at ~26.5 Å (blue dash line). IgG models are shown in ribbon representation, in which heavy chains are in yellow and magenta, and light chains are in cyan and green. Scale bars = 10 nm.

During the docking process, which was similar to what has been reported[49], the IPET 3D map was used as a constraint. The Fab domains and half Fc domain of the crystal structure were treated as rigid bodies to be oriented and inserted into the EM envelope through the rotation operator, maximizing the overlap between the domain structure and map (notably, the heavy chain and light chain in Fab domains are not distinguishable at the current resolution). The hinge region was treated as a flexible structure to respond to the domain position changes, but under the constraints of chemical bonds and energy minimization. The final 3D conformation of the IgG homodimer was achieved by targeted molecular dynamics (TMD) simulations, maximizing the overlap between the structure and the density map while minimizing the energy of the structure. The quality of the fitting to the envelope was evaluated by the FSC curve computed between the model and density map (Fig. 3E,J).

By repeating the IPET 3D reconstruction on an X-shaped particle, we reconstructed a 3D map at ~13.7 Å resolution (Fig. 3G–K, Supplementary Video 1). The intermediate results of the iterative tilt series alignment (Fig. 3G) and the final 3D reconstruction showed a particle with an overall diameter of ~190 Å, containing two large dumbbell-shaped domains and two smaller domains (Fig. 3H). The two large domains, with similar lengths

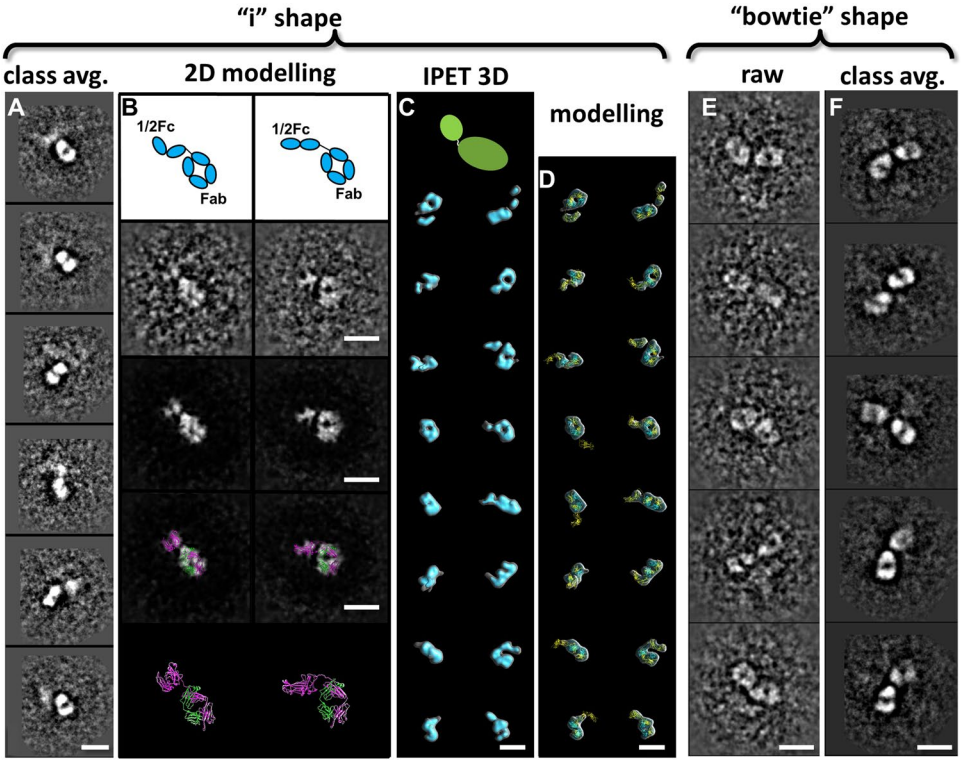

Figure 4. Minor species, i-shaped and bow-tie-shaped particles, presented in IgG homodimer. (**A**) Six representative class averages of i-shaped particle based on OpNS images. (**B**) Two representative i-shaped particles were superposed by using a half-IgG model. (**C**) Sixteen density maps of i-shaped particle were reconstructed by using IPET. These density maps are presented in double contours. The inner contours are shown in cyan; outer contours are shown in transparent gray. (**D**) The density maps were flexibly docked with half-IgG models. (**E**) Five representative bow-tie-shaped particles. (**F**) Five representative bow-tie-shaped class averages. Scale bars = 10 nm.

of ~80–90 Å and widths of ~40–50 Å, were likely the Fab domains. The small domains, with a length of ~80 Å and width of ~30 Å, were likely to be two halves of the Fc domain.

After flexibly docking the crystal structure into this map, the 3D conformation of the X-shaped particle (Fig. 3I,K, Supplementary Video 1) showed that the two halves of the Fc domain formed an angle of ~100° with a distance between the far ends of ~44 Å. This distance was rather large compared to the distance between two C_H3 domains in the Y-shaped particle, where two C_H3 domains were attached to each other. This large distance between two C_H3 domains suggested a weak interaction.

By further repeating the above process, a total of 80 particles were targeted for IPET 3D reconstruction from a pool of ~250 particles acquired from four tilt series (Figs 3, 4 and 5, Supplementary Figs 2–45, Supplementary Table 1). A large number of particles were excluded due to particle-particle overlapping at certain tilt angles, missing tilted views, uneven surrounding stain backgrounds or already sufficient examples to present each species. The 80 IPET 3D maps included 16 maps from the Y-shaped particles, 48 maps from the X-shaped particles and 16 maps from the i-shaped particles. The map resolutions were within a range of ~12 to ~15 Å. By flexibly fitting the crystal structure into these maps, we obtained 16 conformations for Y-shaped antibodies (Fig. 5B, Supplementary Figs 2–11), 48 conformations for X-shaped antibodies (Fig. 5D, Supplementary Figs 12–35) and 16 conformations for half antibodies (Fig. 4A–D, Supplementary Figs 36–45).

Resolution analysis on IPET 3D reconstruction. The resolution of IPET reconstruction was estimated by the following methods as reported[49]. (i) The single-particle method[91,92], in which the resolution of the IPET reconstruction was estimated based on the matching of data to themselves by splitting the tilted images into two halves for reconstruction independently. The points where the FSC curve fell below 0.5 were used to represent the reconstruction resolution[91,92]. In this case, the resolution of the first reconstructed Y-shaped antibody was ~13.2 Å, while that of the first reconstructed X-shaped antibody was 13.7 Å (black solid lines in Fig. 3E,J). However, if we chose the "gold-standard" criteria[93], *i.e.* using the point where the FSC curve fell below 0.143 as the resolution, the resolution of the Y-shaped antibody was ~9.7 Å, while that of the X-shaped antibody was ~9.6 Å (black solid lines in Fig. 3E,J). (ii) A model-to-map method, in which the resolution was estimated based on the matching of data to the best fitted model. The 3D density map of the best fitted structure using *pdb2mrc* software (EMAN package)[78] was used to calculate the FSC curve against the IPET 3D map. The resolutions at which the FSC curves fell below 0.5 were ~31.4 Å for the Y-shaped antibody and ~33.8 Å for the X-shaped antibody (blue dash line in Fig. 3E,J). If we used "gold standard" criteria[93], the resolutions were ~23.7 Å for the Y-shaped antibody

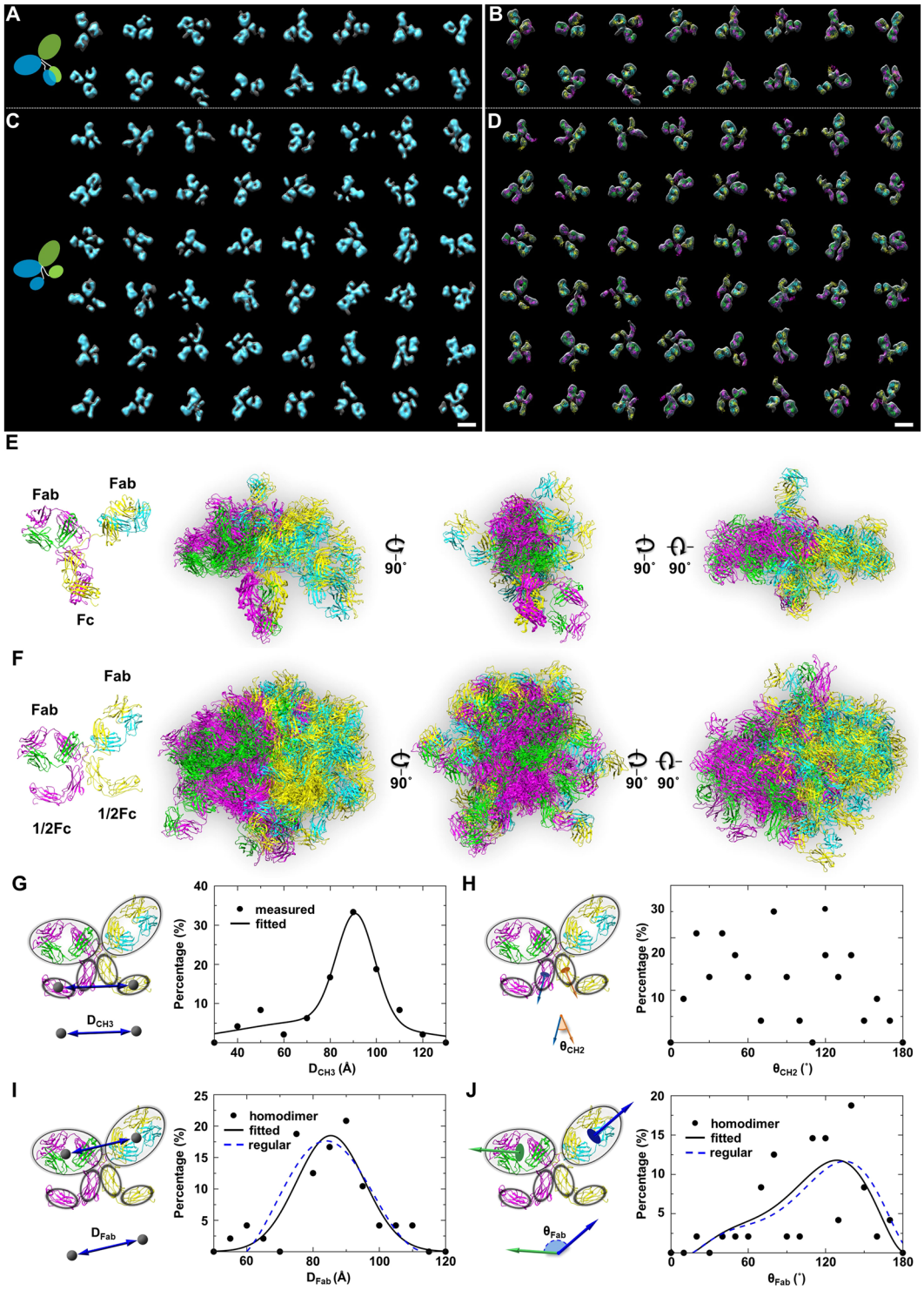

Figure 5. 3D conformation and conformational flexibility of IgG homodimer. (**A**) Sixteen density maps of Y-shaped IgG homodimers by IPET. (**B**) The density maps were flexibly docked using the crystal structure of a IgG to determine the overall conformations of corresponding maps. (**C**) Forty-eight density maps of X-shaped IgG homodimers by IPET. (**D**) The density maps were flexibly docked using the crystal structure of a IgG to determine the overall conformations of corresponding maps. The density maps are presented in double contours. The inner contours contoured surfaces are shown in cyan; outer contours are shown as transparent gray surfaces. (**E**) Sixteen Y-shaped conformations were aligned based on their C_H2 domains. (**F**) Forty-eight X-shaped conformations were aligned based on their C_H2 domains. Distributions of Y- and X-shaped IgG homodimers are shown from three orthogonal views. (**G**) Schematic model illustrating the distance between centers of C_H3 domains (left) and the histogram of measured distance from 48 X-shaped homodimers (right). The histogram was fitted by using 2-term Gaussian model. (**H**) Schematic model illustrating the angle between the C_H2 domains (left) and the histogram of the measured angle (right). (**I**) Schematic model illustrating

the distance between centers of Fab domains (left) and the histogram of the measured distance (right). The histogram was fitted by using Gaussian model, and compared with the distance curve reported for Y-shaped IgG[49]. (**J**) Schematic model illustrating the angle between Fab domains (left) and the histogram of the measured angle (right). The histogram was fitted by using sixth degree polynomial curve and compared with the angle curve reported for regular IgG[49].

and ~26.5 Å for the X-shaped antibody. Notably, because the domains in the crystal structure were docked into the IPET maps as rigid bodies, the flexibility within the Fab and half Fc domains was not included in the resolution estimation, which may lead to an underestimated resolution. iii) A structural feature comparison method. The structural features included the maps of two heavy chain segments (C_H2 and C_H3) in the Fc domain. Since the dimension of C_H2/C_H3 was ~17 × ~18 × ~35 Å, the success in reconstructing the domains suggested the resolutions were roughly ~20 Å, consistent with the previous study of IgG1[49]. To simplify estimation, we chose the frequency at which the FSC curve from single particle method fell below 0.5 (instead of 0.143) as an estimate of the resolution, as the previous publications[24,39,40,49,52,57–59].

Statistical analysis of the conformational flexibility of 64 conformations. To reveal the flexibility of the newly found X-shaped particles, the 48 X-shaped particles were aligned to each other based on the structure of their C_H2 domains. This alignment yielded an overall ball-like distribution in which both Fab domains and Fc domains adopted a wide range of angles and orientations (Fig. 5F). Compared to the aligned 3D conformations of the Y-shaped particles (Fig. 5E), the Fc domains in the X-shaped particles presented with a wider distribution of spatial orientations, suggesting that the X-shaped particles have increased flexibility, particularly in the Fc domain.

To quantify the conformational flexibility of the Fc domains, we analyzed the distribution of distances between the centers of the C_H3 domains and the distribution of angles between the C_H2 domains of the 48 X-shaped particles. The histogram of the distances (fitted by a 2-term Gaussian model) showed that ~72.1% of the X-shaped particles have C_H3 distances ranging from 70–110 Å (Fig. 5G). The angles measured between two C_H2 domains were distributed in a range of 0° to 180° (Fig. 5H). The histogram of the angles showed no obvious peak population, suggesting that two halves of the Fc domains can move and rotate freely, with little constraint or force against each other.

Likewise, to quantify the conformational flexibility between two Fab domains of X-shaped particles, and to compare it to that of regular Y-shaped particles reported before[49], the distances and angles between Fab domains were measured. The histogram of the distances from ~50 to ~115 Å (Fig. 5I, fitted by a 1-term Gaussian model) showed a peak population at a distance of ~85 Å. The histogram of the angles from ~10° to 180° (Fig. 5J, mostly asymmetrical, therefore fitted by a sixth-degree polynomial curve) showed a peak at ~130°. The distributions of distances and angles were similar to those of the published IgG1[49] by IPET (Fig. 5I,J, dashed lines). In addition, the peak distance and angle of the X-shaped particles (~85 Å and ~130°) were similar to the distance and angle measured between two Fab domains in the IgG1 crystal structure (~89 Å and ~140°, PDB entry 1HZH). These results suggested that the flexibility of the two C_H3 domains within the Fc domain does not influence the flexibility of the two Fab domains. This may result from the highly flexible hinge region that decouples conformational changes in the Fc domain from the F domains.

Discussion

EM images give insight into the structural variety of the IgG homodimer, especially the interactions between the heavy chain segments forming the Fc domain (C_H2 and C_H3 domains). In addition to the Y-shaped conformations seen in the reported IgG1 molecules[49], X-shaped conformations were also observed, in which the two heavy chain segments of the Fc domain are apart. These results are also consistent with previous biophysical studies[27].

Structural interpretation of the interaction between two C_H3 chains. The IPET reconstructions show that the interaction between the two halves of the Fc domain in X-shaped IgG hole-hole homodimers is weakened compared to that of Y-shaped particles, which allows the two halves to move freely. To aid in the structural interpretation of this observation, we used the crystal structure of an IgG1 (PDB: 1HZH) as a template, as well as an Fc fragment with hole-hole mutations (PDB entry 4NQT)[94] as a template to construct a homology model of the IgG hole-hole homodimer (see Methods). The crystal structure of IgG1 shows that multiple residues contribute to the interaction between two C_H3 domains in forming the Fc domain. The interactions include (i) hydrogen bonding between T366 and Y407[95], which are within hydrogen-bonding distance, as reported[95]; (ii) π-stacking between Y407 residues, where the benzene rings of two Y407 residues in the two halves of the Fc domain are located side-by-side with a distance of 4.31 Å, as an energetically stable conformation from π-stacking[96]; and (iii) inter-domain hydrogen bonding mediated by a network of water molecules[97].

In the hole-hole homodimer, mutations were introduced into the Fc domain (T366S, L368A and Y407V[27]), located at the C_H3-C_H3 interface (Supplementary Fig. 46A). These mutations seem to reduce the interactions between two C_H3 domains (Supplementary Fig. 46B). It is plausible that upon mutation, V407 and S366 become too far from each other to maintain the original hydrogen bond. Additionally, the mutation from tyrosine to valine removes the original π-stacking interaction between the two Y407 residues. Together, these mutations lead to reduced interactions between C_H3 domains, thus the two C_H3 domains can move freely from each other and lead to the observation of X-shaped particles in the homodimer. Hydrogen-deuterium exchange mass spectrometry also shows decreased protection of the same regions in the C_H3 domains, consistent with fewer interactions[27].

Interestingly, Y-shaped homodimer particles with intact Fc domains were still observed in the homodimer sample, suggesting that the two halves of the Fc domain still maintain some interactions after mutation, but with

reduced strength. For example, the mutation of hydrophilic Y407 to hydrophobic V407 increases the hydrophobicity of the local surface (Supplementary Fig. 46C,D), and therefore may increase the nonspecific hydrophobic interactions between the two halves of the Fc domain. The observation of both X- and Y-shaped particles may relate to the equilibrium between the conformations.

Minor components in the hole-hole homodimer sample. In addition to Y- and X-shaped particles, low percentages of bow-tie-shaped particles (~10.0%) and i-shaped particles (~2.5%) were also observed in the sample of IgG hole-hole homodimer (Figs 1D and 4A,E,F). The bow-tie-shaped particles contain two domains that are similar to each other in size and shape, and similar to the Fab domains in the Y- and X-shaped particles. However, the third domain, likely the Fc domain, is not seen. Given that physically truncated homodimers were not detected by chromatography, native MS or HDX-MS[27], the apparently absent Fc domain is likely still present but denatured or disordered, resulting in a lack of visibility in EM images.

The i-shaped particles have an overall diameter of ~110 Å, with a similar size and shape to half of an X-shaped IgG. These particles are likely formed by Fab domain and half of an Fc domain (Fig. 4A,B), *i.e.* a single heavy and light chain. This hypothesis is consistent with our previous study in which a species with half of an intact IgG mass was identified in the hole-hole homodimer sample by native MS[27]. However, in that study the species observed by native MS could not be reliably detected by SEC, possibly due to its low abundance. Our 16 IPET maps of i-shaped particles showed that the particle is composed of a large and a small globular domain, which are similar to half of the X-shaped antibody in size and shape (Fig. 4C and Supplementary Figs 36–45). By flexibly fitting a half-antibody model into each map (Fig. 4D and Supplementary Figs 36–45), the agreement in overall size and shape strongly supports the hypothesis that the i-shaped particles are halves of antibodies. The observation of half-antibodies, especially the half Fc domain (approximately 25 kDa), is far below the limitations of EM imaging using other methods, suggesting that the combination of the OpNS and IPET methods can be used as a supplementary tool to study the structure of small and flexible proteins, including therapeutic IgGs.

Conclusion

In this study, we characterized the newly discovered X-shaped particles in a hole-hole homodimer using NS-EM with IPET technology. Through the 3D reconstruction of 64 individual particles, we confirmed that the apparent X-shape was due to the weakened interaction between the two halves of the Fc domain of this homodimer. The X-shaped particle was not observed in regular IgG1 samples. The weakened interaction between the two halves of the Fc domain in the homodimer appears to be due to the mutations in the C_H3 domain. We also observed several minor species using the IPET method. Our study demonstrates the capability of the IPET with NS-EM method in the topological study of small and flexible proteins in heterogeneous samples, as a supplementary tool for future engineering optimization of therapeutic antibodies.

Methods

Production of the hole—hole homodimer and NISTmAb. The hole-hole homodimer was produced as described in literature[27]. In brief, the harvested cell culture fluid containing the hole half antibody was first purified on protein-A affinity chromatography. The pH of the protein-A pool was adjusted from 3.3 to 5.0, and Poros cation exchange chromatography was used to separate the hole-hole homodimer from the half antibody and other species. The resulting solution was then eluted at pH 5.5. The solution was finally submitted to ultrafiltration/diafiltration and conditioned at pH 5.8 in 20 mM histidine acetate buffer. Intact mass analysis confirmed that the hole-hole homodimer was a covalent homodimer. The NISTmAb is a recombinant, humanized IgG1 expressed in a murine suspension culture[74], and is available as a reference material (RM 8671). As supplied, the reference material (lot 14HB-D-002) typically contains approximately 3% oligomers (dimer/trimer) by mass. For EM studies, monomeric NISTmAb was isolated by size exclusion chromatography in phosphate buffered saline (PBS) using a Superdex 200 16/60 Prep Grade column (GE Healthcare) and flash-frozen until needed.

Preparation of OpNS-EM specimens. The OpNS specimens of IgG hole-hole homodimers and the NISTmAb were prepared by using the protocol as described[35–38]. In brief, IgG samples were diluted to ~0.04 μg mL^{-1} with Dulbecco's phosphate-buffered saline (DPBS). An aliquot (approximately 4 μL) of diluted sample was placed on an ultra-thin carbon-coated 200-mesh copper grid (CF200-Cu-UL, Electron Microscopy Sciences, Hatfield, PA, USA, and Cu-200CN, Pacific Grid-Tech, San Francisco, CA, USA) that had been glow-discharged for 15 s. After 1-min incubation, the excess solution on the grid was blotted with filter paper. The grid was then washed with water and stained with 1% (w/v) uranyl formate (UF) before air-drying with nitrogen.

TEM un-tilted data acquisition and image processing. OpNS samples were examined by using a Zeiss Libra 120 Plus TEM (Carl Zeiss NTS) operated at 120 kV high tension with a 10–20 eV energy filter. The OpNS micrographs were acquired under defocus at ~0.6 μm to ~0.9 μm and a dose of ~40–90 $e^{-}Å^{-2}$ using a Gatan UltraScan 4 K X 4 K CCD under a magnification of 80 kx (each pixel of the micrographs corresponds to 1.48 Å in specimens). The contrast transfer function (CTF) of each micrograph was examined by using *ctffind3* software[98] and corrected by using the "*TF CTS*" command in SPIDER[99] software or GCTF[100] after the X-ray speckles were removed. Particles were then selected from the micrographs with a box size of 192 × 192 by using *boxer* (EMAN[78] software). All particles were masked by using a round mask generated from SPIDER software after a Gaussian high-pass filtering. The reference-free class averages of particles were obtained by using *refine2d* (EMAN software) based on 13,546 particles of hole-hole homodimer and 4,961 particles of NISTmAb.

Overall structure of X-shaped particles in IgG homodimer and half-IgG by 2D mapping. Although individual images or class averages provide only 2D information of the particles and are insufficient to determine

their 3D structures, raw images and class averages with high contrast could still provide important clues about the 3D orientation or even the overall structure of the particles. Here, we tried to determine the overall structure of the X-shaped particles in IgG homodimer by flexibly superposing an IgG model (the crystal structure of a human IgGl, PDB entry 1HZH[41]) onto images or class averages via the following protocol. First, the missing residues in the crystal structure were recovered using UCSF Chimera software. Next, the two Fab domains and the two heavy chain Fc regions in the crystal structure were separately rigid-body translated/rotated to obtain the best-fit for the corresponding domains obtained from images or class averages. To distinguish Fab domains from Fc regions obtained from the images and averages, the following criteria were used: i) two Fab domains are similar in size and shape; ii) the two halves of the Fc are both distinguishably smaller than an Fab domain. The above protocol was also used for determining the overall structure of half-IgG.

Conformations of IgG homodimer and half-IgG. The resolution (approximately 12–15 Å) of the IPET 3D reconstructions was insufficient to determine the high-resolution atomic structure of each individual IgG. However, the reconstructions were sufficient to determine the overall domain orientations and positions and reveal the structural heterogeneity and dynamics of the homodimer with mutations in the Fc region. We chose the crystal structure of human IgG (PDB entry 1HZH[41]) as a model to reflect the IgG structural dynamics and flexibly docked it into the reconstruction of homodimer and half-IgG by using the following protocol. After the missing residues in the crystal structure were recovered by using Chimera, the Fab domains and heavy chain Fc regions were truncated from the crystal structure and separately rigid-body docked into the density map envelope using Chimera. Finally, the positions and orientations of the docked domains were used as guides for performing targeted molecular dynamics (TMD) simulations.

To distinguish Fab domains from the heavy chain Fc region and determine their overall location and orientation in the 3D density maps, the following criteria were used in addition to these in the previous section: the distance between the Fab domain and corresponding heavy chain Fc region should be allowed by the length of central loop.

By using the best-fit positions as the target positions, we drove the model to correlate with the density map by using a TMD simulation technique. The dragging and moving forces were pre-calculated and applied to all backbone atoms in each domain of the crystal structure to gradually steer the domains toward their corresponding best-fit positions and orientations. During this process, the domain structure and the chemical structure, including disulfide bonds, were constrained as the original crystal structure, whereas the loop regions were left flexible, allowing conformational changes to occur. As a result, the newly modeled structure of the IgG had the same domain structure as in the crystal structure, but had different relative domain positions and orientations.

The TMD simulation was performed using the NAMD2[101] software and CHARMM27[102] force fields. A cut-off distance for van der Waals interactions was set to 12 Å. The whole system was heated from 0 K to 310 K over a 62-ps simulation using weakly coupled Langevin dynamics, and the temperature was then maintained at 310 K. The pressure was maintained at 1 atm using a Langevin piston Nose-Hoover barostat (with a piston period of 100 fs and a decay time of 50 fs). It took 300 k steps to complete the conformational changes, and the simulation length was 0.6 ns.

ET data acquisition and image pre-processing. The TEM holder was tilted at angles ranging from −45° to +45° in 1.5° increments, and imaging was controlled using Gatan tomography software (Zeiss Libra 120 Plus TEM). The TEM was operated at 120 kV high tension with a 20-eV energy filter. The tilt series was acquired under low defocus conditions (<1 μm) using a Gatan UltraScan 4 K X 4 K CCD under a magnification of 80 kx (each pixel of the micrographs corresponds to 1.48 Å in specimens). The total electron doses were 2,800–6,600 $e^{-}Å^{-2}$. The micrographs were initially aligned using the IMOD[103] software package. The CTF was then corrected using TomoCTF[104]. The tilt series of the particles in square windows of 256 × 256 pixels (~38 nm) were semi-automatically tracked, windowed using IPET software[39], and finally binned by 2 to reduce computation time in the subsequent reconstruction.

IPET 3D reconstruction. In the IPET reconstruction process[39], a tilt series of CTF-corrected images (~38 nm) containing a single IgG homodimer or half-IgG particle was directly back-projected into an *ab initio* 3D density map as an initial model based on the corresponding goniometer tilt angles of images. The refinement was started using this initial model to align each tilt image via translational alignment to the projections of the initial model. During refinement, automatically generated low-pass filters, a circular-shaped mask with a Gaussian boundary, and particle-shaped masks with a Gaussian boundary were sequentially applied to the tilt images and references to increase the alignment accuracy[39]. The resolution was defined based on Fourier shell correction (FSC) calculation, in which the aligned images were split into two halves based on an odd- or even-numbered index to generate two 3D reconstructions for computing their FSC curve against the spatial frequency shells in Fourier space. The frequency at which the FSC curve first fell to a value of 0.5 was used to represent the resolution of the IPET 3D density map. All IPET density maps presented in the figures were low-pass filtered to 20 Å.

Notably, a tilt angle range of ±45° was used for IPET 3D reconstruction, which could lead to missing wedge artifacts, such as elongation, blurring, and distracting caustics[105]. However, the effects of the missing wedge can be reduced via computational algorithms as reported by numerous groups[105–108]. Agard and Stroud reported a computational approach to fill the missing data in 2D electron crystallography[109]. Recently, Kovacik, *et al*. used a simple Fourier angular filter[106], Ruotsalainen *et al*. developed a statistical reconstruction method[110], Sun *et al*. reported an iterative compressed-sensing[107], and Miao *et al*. proposed a generalized Fourier iterative reconstruction algorithm (GENFIRE) to reduce the missing wedge artifact to achieve a 3D structure with more isotropic resolution[108]. In our IPET 3D reconstruction, we used our real-Fourier space iteration algorithm to fill the missing wedge[51,52,57,58]. The related methodology paper is in preparation.

Statistical analysis of IgG homodimer dynamics. To quantify the conformational dynamics of the IgG homodimers, all 64 IgG homodimer conformations were aligned based on their C_H2 domains using VMD software[111]. The distribution of distance and angle between Fab domains, distance between C_H3 domains and angle between C_H2 domains were then measured to study the fluctuations and dynamic features of the IgG homodimer. To measure distance, we first calculated the mass center of each Fab and C_H3 domain and then measured the distance between the mass centers of the Fab domains (Fig. 5I), and between the mass centers of the C_H3 domains (Fig. 5G). To measure angles, we first introduced vectors to determine the orientation of each Fab domain and each C_H2 domain (Fig. 5H,J), and then measured angles between the vectors. These vectors were defined by using backbone atoms at the two far ends of Fab domains and C_H2 domains.

The measured distances and angles from 48 X-shaped IgG homodimers were plotted onto histograms and fitted with polynomial or Gaussian curves using MATLAB. These histograms represented the conformational space of the IgG homodimer and indicated the extent of the structural dynamics of the homodimer.

Construction of a homology model for IgG homodimer Fc domain. To study contacts between C_H3 domains after hole mutations, a homology model for the Fc domain of the hole-hole homodimer was constructed. First, the two halves of the Fc region with hole mutations were derived from the crystal structure of homodimeric hole Fc fragment (PDB entry 4NQT[94]). The two halves were then separately superposed onto the corresponding halves of Fc region in the typical IgG using Chimera.

Data deposition. The TEM 3D density maps of 64 IgG homodimers and 16 half-IgGs are available from the EM data bank as EMDB IDs 7353–7368, 7369–7417 and 7418–7433.

References

1. Gordon, L. I. *et al*. Durable responses after ibritumomab tiuxetan radioimmunotherapy for CD20+ B-cell lymphoma: long-term follow-up of a phase 1/2 study. *Blood* **103**, 4429–4431, https://doi.org/10.1182/blood-2003-11-3883 (2004).
2. Cohen, M. H., Gootenberg, J., Keegan, P. & Pazdur, R. FDA drug approval summary: bevacizumab (Avastin) plus Carboplatin and Paclitaxel as first-line treatment of advanced/metastatic recurrent nonsquamous non-small cell lung cancer. *Oncologist* **12**, 713–718, https://doi.org/10.1634/theoncologist.12-6-713 (2007).
3. Bou-Assaly, W. & Mukherji, S. Cetuximab (erbitux). *AJNR. American journal of neuroradiology* **31**, 626–627, https://doi.org/10.3174/ajnr.A2054 (2010).
4. Venkiteshwaran, A. Tocilizumab. *Mabs* **1**, 432–438 (2009).
5. Cohen, S. B. *et al*. Rituximab for rheumatoid arthritis refractory to anti-tumor necrosis factor therapy: Results of a multicenter, randomized, double-blind, placebo-controlled, phase III trial evaluating primary efficacy and safety at twenty-four weeks. *Arthritis Rheum* **54**, 2793–2806, https://doi.org/10.1002/art.22025 (2006).
6. Moreland, L., Bate, G. & Kirkpatrick, P. Abatacept. *Nat Rev Drug Discov* **5**, 185–186, https://doi.org/10.1038/nrd1989 (2006).
7. Humbert, M. *et al*. Omalizumab in asthma: an update on recent developments. *The journal of allergy and clinical immunology. In practice* **2**, 525–536 e521, https://doi.org/10.1016/j.jaip.2014.03.010 (2014).
8. Polman, C. H. *et al*. A randomized, placebo-controlled trial of natalizumab for relapsing multiple sclerosis. *The New England journal of medicine* **354**, 899–910, https://doi.org/10.1056/NEJMoa044397 (2006).
9. Kornbluth, A. Infliximab Approved for Use in Crohn's Disease: A Report on the FDA GI Advisory Committee Conference. *Inflammatory Bowel Diseases* **4**, 328–329, https://doi.org/10.1097/00054725-199811000-00014 (1998).
10. Demko, S., Summers, J., Keegan, P. & Pazdur, R. FDA drug approval summary: alemtuzumab as single-agent treatment for B-cell chronic lymphocytic leukemia. *Oncologist* **13**, 167–174, https://doi.org/10.1634/theoncologist.2007-0218 (2008).
11. Nunez-Prado, N. *et al*. The coming of age of engineered multivalent antibodies. *Drug Discov Today* **20**, 588–594, https://doi.org/10.1016/j.drudis.2015.02.013 (2015).
12. Bournazos, S., Gazumyan, A., Seaman, M. S., Nussenzweig, M. C. & Ravetch, J. V. Bispecific Anti-HIV-1 Antibodies with Enhanced Breadth and Potency. *Cell* **165**, 1609–1620, https://doi.org/10.1016/j.cell.2016.04.050 (2016).
13. Spiess, C., Zhai, Q. & Carter, P. J. Alternative molecular formats and therapeutic applications for bispecific antibodies. *Mol Immunol* **67**, 95–106, https://doi.org/10.1016/j.molimm.2015.01.003 (2015).
14. Oberg, H. H. *et al*. Novel bispecific antibodies increase gammadelta T-cell cytotoxicity against pancreatic cancer cells. *Cancer Res* **74**, 1349–1360, https://doi.org/10.1158/0008-5472.CAN-13-0675 (2014).
15. Baeuerle, P. A. & Reinhardt, C. Bispecific T-cell engaging antibodies for cancer therapy. *Cancer Res* **69**, 4941–4944, https://doi.org/10.1158/0008-5472.CAN-09-0547 (2009).
16. Topp, M. S. *et al*. Safety and activity of blinatumomab for adult patients with relapsed or refractory B-precursor acute lymphoblastic leukaemia: a multicentre, single-arm, phase 2 study. *Lancet Oncol* **16**, 57–66, https://doi.org/10.1016/S1470-2045(14)71170-2 (2015).
17. Timur, S. S., Bhattarai, P., Gursoy, R. N., Vural, I. & Khaw, B. A. Design and *In Vitro* Evaluation of Bispecific Complexes and Drug Conjugates of Anticancer Peptide, LyP-1 in Human Breast Cancer. *Pharm Res* **34**, 352–364, https://doi.org/10.1007/s11095-016-2066-2 (2017).
18. Peters, C. & Brown, S. Antibody-drug conjugates as novel anti-cancer chemotherapeutics. *Biosci Rep* **35**, https://doi.org/10.1042/BSR20150089 (2015).
19. Davis, J. H. *et al*. SEEDbodies: fusion proteins based on strand-exchange engineered domain (SEED) CH3 heterodimers in an Fc analogue platform for asymmetric binders or immunofusions and bispecific antibodies. *Protein Eng Des Sel* **23**, 195–202, https://doi.org/10.1093/protein/gzp094 (2010).
20. Gunasekaran, K. *et al*. Enhancing antibody Fc heterodimer formation through electrostatic steering effects: applications to bispecific molecules and monovalent IgG. *J Biol Chem* **285**, 19637–19646, https://doi.org/10.1074/jbc.M110.117382 (2010).
21. Labrijn, A. F. *et al*. Efficient generation of stable bispecific IgG1 by controlled Fab-arm exchange. *Proc Natl Acad Sci USA* **110**, 5145–5150, https://doi.org/10.1073/pnas.1220145110 (2013).
22. Holliger, P., Prospero, T. & Winter, G. "Diabodies": small bivalent and bispecific antibody fragments. *Proc Natl Acad Sci USA* **90**, 6444–6448, https://doi.org/10.1073/pnas.90.14.6444 (1993).
23. Doppalapudi, V. R. *et al*. Chemical generation of bispecific antibodies. *Proc Natl Acad Sci USA* **107**, 22611–22616, https://doi.org/10.1073/pnas.1016478108 (2010).
24. Tong, H. *et al*. Peptide-conjugation induced conformational changes in human IgG1 observed by optimized negative-staining and individual-particle electron tomography. *Sci Rep-Uk* **3**, 1089, https://doi.org/10.1038/srep01089 (2013).
25. Bacac, M. *et al*. A Novel Carcinoembryonic Antigen T-Cell Bispecific Antibody (CEA TCB) for the Treatment of Solid Tumors. *Clin Cancer Res* **22**, 3286–3297, https://doi.org/10.1158/1078-0432.CCR-15-1696 (2016).

26. Spiess, C. *et al*. Development of a human IgG4 bispecific antibody for dual targeting of interleukin-4 (IL-4) and interleukin-13 (IL-13) cytokines. *J Biol Chem* **288**, 26583–26593, https://doi.org/10.1074/jbc.M113.480483 (2013).
27. Zhang, H. M. *et al*. Structural and Functional Characterization of a Hole-Hole Homodimer Variant in a "Knob-Into-Hole" Bispecific Antibody. *Anal Chem* **89**, 13494–13501, https://doi.org/10.1021/acs.analchem.7b03830 (2017).
28. Liao, M., Cao, E., Julius, D. & Cheng, Y. Structure of the TRPV1 ion channel determined by electron cryo-microscopy. *Nature* **504**, 107–112, https://doi.org/10.1038/nature12822 (2013).
29. Bai, X. C., McMullan, G. & Scheres, S. H. How cryo-EM is revolutionizing structural biology. *Trends Biochem Sci* **40**, 49–57, https://doi.org/10.1016/j.tibs.2014.10.005 (2015).
30. Cheng, Y. Single-Particle Cryo-EM at Crystallographic Resolution. *Cell* **161**, 450–457, https://doi.org/10.1016/j.cell.2015.03.049 (2015).
31. Vidarsson, G., Dekkers, G. & Rispens, T. IgG subclasses and allotypes: from structure to effector functions. *Front Immunol* **5**, 520, https://doi.org/10.3389/fimmu.2014.00520 (2014).
32. Zhang, W., Kimmel, M., Spahn, C. M. & Penczek, P. A. Heterogeneity of large macromolecular complexes revealed by 3D cryo-EM variance analysis. *Structure* **16**, 1770–1776, https://doi.org/10.1016/j.str.2008.10.011 (2008).
33. Tan, Y. Z. *et al*. Addressing preferred specimen orientation in single-particle cryo-EM through tilting. *Nature methods* **14**, 793–796, https://doi.org/10.1038/nmeth.4347 (2017).
34. Cabra, V. & Samso, M. Do's and don'ts of cryo-electron microscopy: a primer on sample preparation and high quality data collection for macromolecular 3D reconstruction. *J. Vis. Exp*. 52311, https://doi.org/10.3791/52311 (2015).
35. Zhang, L. *et al*. An optimized negative-staining protocol of electron microscopy for apoE4 POPC lipoprotein. *J Lipid Res* **51**, 1228–1236, https://doi.org/10.1194/jlr.D002493 (2010).
36. Zhang, L. *et al*. Morphology and structure of lipoproteins revealed by an optimized negative-staining protocol of electron microscopy. *J Lipid Res* **52**, 175–184, https://doi.org/10.1194/jlr.D010959 (2011).
37. Rames, M., Yu, Y. & Ren, G. Optimized negative staining: a high-throughput protocol for examining small and asymmetric protein structure by electron microscopy. *J. Vis. Exp*. e51087, https://doi.org/10.3791/51087 (2014).
38. Zhang, L., Tong, H., Garewal, M. & Ren, G. Optimized negative-staining electron microscopy for lipoprotein studies. *Biochimica et biophysica acta* **1830**, 2150–2159, https://doi.org/10.1016/j.bbagen.2012.09.016 (2013).
39. Zhang, L. & Ren, G. IPET and FETR: experimental approach for studying molecular structure dynamics by cryo-electron tomography of a single-molecule structure. *PLoS One* **7**, e30249, https://doi.org/10.1371/journal.pone.0030249 (2012).
40. Lu, Z. *et al*. Calsyntenin-3 molecular architecture and interaction with neurexin 1alpha. *J Biol Chem* **289**, 34530–34542, https://doi.org/10.1074/jbc.M114.606806 (2014).
41. Saphire, E. O. *et al*. Crystal structure of a neutralizing human IGG against HIV-1: a template for vaccine design. *Science* **293**, 1155–1159, https://doi.org/10.1126/science.1061692 (2001).
42. Zhang, M. *et al*. HDL surface lipids mediate CETP binding as revealed by electron microscopy and molecular dynamics simulation. *Sci Rep-Uk* **5**, 8741, https://doi.org/10.1038/srep08741 (2015).
43. Segrest, J. P. *et al*. Surface Density-Induced Pleating of a Lipid Monolayer Drives Nascent High-Density Lipoprotein Assembly. *Structure* **23**, 1214–1226, https://doi.org/10.1016/j.str.2015.05.010 (2015).
44. Chen, B. *et al*. Apolipoprotein AI tertiary structures determine stability and phospholipid-binding activity of discoidal high-density lipoprotein particles of different sizes. *Protein Sci* **18**, 921–935, https://doi.org/10.1002/pro.101 (2009).
45. Cavigiolio, G. *et al*. The interplay between size, morphology, stability, and functionality of high-density lipoprotein subclasses. *Biochemistry* **47**, 4770–4779, https://doi.org/10.1021/bi7023354 (2008).
46. Zhang, L. *et al*. Structural basis of transfer between lipoproteins by cholesteryl ester transfer protein. *Nat Chem Biol* **8**, 342–349, https://doi.org/10.1038/nchembio.796 (2012).
47. Cho, W. J. *et al*. Membrane-directed molecular assembly of the neuronal SNARE complex. *J Cell Mol Med* **15**, 31–37, https://doi.org/10.1111/j.1582-4934.2010.01152.x (2011).
48. Deng, X. *et al*. Large Conformational Changes of Insertion 3 in Human Glycyl-tRNA Synthetase (hGlyRS) during Catalysis. *J Biol Chem* **291**, 5740–5752, https://doi.org/10.1074/jbc.M115.679126 (2016).
49. Zhang, X. *et al*. 3D Structural Fluctuation of IgG1 Antibody Revealed by Individual Particle Electron Tomography. *Sci Rep-Uk* **5**, 9803, https://doi.org/10.1038/srep09803 (2015).
50. Zhang, M. *et al*. Structural basis of the lipid transfer mechanism of phospholipid transfer protein (PLTP). Biochimica et biophysica acta. *Molecular and cell biology of lipids* **1863**, 1082–1094, https://doi.org/10.1016/j.bbalip.2018.06.001 (2018).
51. Liu, J. *et al*. Structural Plasticity of Neurexin 1alpha: Implications for its Role as Synaptic Organizer. *J Mol Biol* **430**, 4325–4343, https://doi.org/10.1016/j.jmb.2018.08.026 (2018).
52. Lei, D. *et al*. Three-dimensional structural dynamics of DNA origami Bennett linkages using individual-particle electron tomography. *Nat Commun* **9**, 592, https://doi.org/10.1038/s41467-018-03018-0 (2018).
53. Jay, J. *et al*. IgG Antibody 3D Structures and Dynamics. *Antibodies* **7**, 18, https://doi.org/10.3390/antib7020018 (2018).
54. Wu, H. *et al*. An Algorithm for Enhancing the Image Contrast of Electron Tomography. *Sci Rep-Uk* **8**, 16711, https://doi.org/10.1038/s41598-018-34652-9 (2018).
55. Zhang, M. *et al*. Assessing the mechanisms of cholesteryl ester transfer protein inhibitors. *Biochimica et biophysica acta. Molecular and cell biology of lipids* **1862**, 1606–1617, https://doi.org/10.1016/j.bbalip.2017.09.004 (2017).
56. Ikon, N. *et al*. A facile method for isolation of recombinant human apolipoprotein A-I from E. coli. *Protein expression and purification* **134**, 18–24, https://doi.org/10.1016/j.pep.2017.03.015 (2017).
57. Zhang, L. *et al*. Three-dimensional structural dynamics and fluctuations of DNA-nanogold conjugates by individual-particle electron tomography. *Nat Commun* **7**, 11083, https://doi.org/10.1038/ncomms11083 (2016).
58. Yu, Y. *et al*. Polyhedral 3D structure of human plasma very low density lipoproteins by individual particle cryo-electron tomography1. *J Lipid Res* **57**, 1879–1888, https://doi.org/10.1194/jlr.M070375 (2016).
59. Lu, Z. *et al*. Molecular Architecture of Contactin-associated Protein-like 2 (CNTNAP2) and Its Interaction with Contactin 2 (CNTN2). *J Biol Chem* **291**, 24133–24147, https://doi.org/10.1074/jbc.M116.748236 (2016).
60. Liu, J. *et al*. Fully Mechanically Controlled Automated Electron Microscopic Tomography. *Sci Rep-Uk* **6**, 29231, https://doi.org/10.1038/srep29231 (2016).
61. Lei, D. *et al*. Insights into the Tunnel Mechanism of Cholesteryl Ester Transfer Protein through All-atom Molecular Dynamics Simulations. *J Biol Chem* **291**, 14034–14044, https://doi.org/10.1074/jbc.M116.715565 (2016).
62. Ercius, P., Alaidi, O., Rames, M. J. & Ren, G. Electron Tomography: A Three-Dimensional Analytic Tool for Hard and Soft Materials Research. *Advanced materials* **27**, 5638–5663, https://doi.org/10.1002/adma.201501015 (2015).
63. Zhang, M. *et al*. Structural basis of the lipid transfer mechanism of phospholipid transfer protein (PLTP). *Biochimica et biophysica acta* **1863**, 1082–1094, https://doi.org/10.1016/j.bbalip.2018.06.001 (2018).
64. Chen, Q. *et al*. Reconstruction of 3D structures of MET antibodies from electron microscopy 2D class averages. *PLoS One* **12**, e0175758, https://doi.org/10.1371/journal.pone.0175758 (2017).
65. Velazquez-Muriel, J. *et al*. Assembly of macromolecular complexes by satisfaction of spatial restraints from electron microscopy images. *Proc Natl Acad Sci USA* **109**, 18821–18826, https://doi.org/10.1073/pnas.1216549109 (2012).
66. Schneidman-Duhovny, D. *et al*. A method for integrative structure determination of protein-protein complexes. *Bioinformatics* **28**, 3282–3289, https://doi.org/10.1093/bioinformatics/bts628 (2012).

67. Lauer, M. E. *et al*. Cholesteryl ester transfer between lipoproteins does not require a ternary tunnel complex with CETP. *J Struct Biol* **194**, 191–198, https://doi.org/10.1016/j.jsb.2016.02.016 (2016).
68. Vilhena, J. G. *et al*. Adsorption orientations and immunological recognition of antibodies on graphene. *Nanoscale* **8**, 13463–13475, https://doi.org/10.1039/c5nr07612a (2016).
69. Lyubchenko, Y. L. & Shlyakhtenko, L. S. AFM for analysis of structure and dynamics of DNA and protein-DNA complexes. *Methods* **47**, 206–213, https://doi.org/10.1016/j.ymeth.2008.09.002 (2009).
70. Sandin, S., Ofverstedt, L. G., Wikstrom, A. C., Wrange, O. & Skoglund, U. Structure and flexibility of individual immunoglobulin G molecules in solution. *Structure* **12**, 409–415, https://doi.org/10.1016/j.str.2004.02.011 (2004).
71. Bongini, L. *et al*. Freezing immunoglobulins to see them move. *Proc Natl Acad Sci USA* **101**, 6466–6471, https://doi.org/10.1073/pnas.0400119101 (2004).
72. Lammerts van Bueren, J. J. *et al*. The antibody zalutumumab inhibits epidermal growth factor receptor signaling by limiting intra- and intermolecular flexibility. *Proc Natl Acad Sci USA* **105**, 6109–6114, https://doi.org/10.1073/pnas.0709477105 (2008).
73. Lammerts van Bueren, J. J. *et al*. Retraction for Lammerts van Bueren *et al*. The antibody zalutumumab inhibits epidermal growth factor receptor signaling by limiting intra- and intermolecular flexibility. *Proc Natl Acad Sci USA* **109**, 5548, https://doi.org/10.1073/pnas.1203736109 (2012).
74. Dong, Q., Yan, X., Liang, Y. & Stein, S. E. In-Depth Characterization and Spectral Library Building of Glycopeptides in the Tryptic Digest of a Monoclonal Antibody Using 1D and 2D LC-MS/MS. *Journal of proteome research* **15**, 1472–1486, https://doi.org/10.1021/acs.jproteome.5b01046 (2016).
75. Schiel, J. E. & Turner, A. The NISTmAb Reference Material 8671 lifecycle management and quality plan. *Analytical and bioanalytical chemistry* **410**, 2067–2078, https://doi.org/10.1007/s00216-017-0844-2 (2018).
76. Schiel, J. E. *et al*. The NISTmAb Reference Material 8671 value assignment, homogeneity, and stability. *Analytical and bioanalytical chemistry* **410**, 2127–2139, https://doi.org/10.1007/s00216-017-0800-1 (2018).
77. Zhao, F. Q. & Craig, R. Capturing time-resolved changes in molecular structure by negative staining. *J Struct Biol* **141**, 43–52 (2003).
78. Ludtke, S. J., Baldwin, P. R. & Chiu, W. EMAN: semiautomated software for high-resolution single-particle reconstructions. *J Struct Biol* **128**, 82–97, https://doi.org/10.1006/jsbi.1999.4174 (1999).
79. Chittuluru, J. R. *et al*. Structure and nucleosome interaction of the yeast NuA4 and Piccolo-NuA4 histone acetyltransferase complexes. *Nature structural & molecular biology* **18**, 1196–1203, https://doi.org/10.1038/nsmb.2128 (2011).
80. Correia, I. *et al*. The structure of dual-variable-domain immunoglobulin molecules alone and bound to antigen. *Mabs* **5**, 364–372, https://doi.org/10.4161/mabs.24258 (2013).
81. Lei, D. *et al*. Single-molecule 3D imaging of human plasma intermediate-density lipoproteins reveals a polyhedral structure. Biochimica et biophysica acta. *Molecular and cell biology of lipids* **1864**, 260–270, https://doi.org/10.1016/j.bbalip.2018.12.004 (2018).
82. Trabuco, L. G., Villa, E., Mitra, K., Frank, J. & Schulten, K. Flexible fitting of atomic structures into electron microscopy maps using molecular dynamics. *Structure* **16**, 673–683, https://doi.org/10.1016/j.str.2008.03.005 (2008).
83. Liu, J., Bartesaghi, A., Borgnia, M. J., Sapiro, G. & Subramaniam, S. Molecular architecture of native HIV-1 gp120 trimers. *Nature* **455**, 109–113, https://doi.org/10.1038/nature07159 (2008).
84. Frank, J. Single-particle reconstruction of biological macromolecules in electron microscopy–30 years. *Quarterly reviews of biophysics* **42**, 139–158, https://doi.org/10.1017/S0033583509990059 (2009).
85. Yang, Z. *et al*. UCSF Chimera, MODELLER, and IMP: an integrated modeling system. *J Struct Biol* **179**, 269–278, https://doi.org/10.1016/j.jsb.2011.09.006 (2012).
86. Malhotra, A. *et al*. Escherichia coli 70 S ribosome at 15 A resolution by cryo-electron microscopy: localization of fMet-tRNAfMet and fitting of L1 protein. *J Mol Biol* **280**, 103–116, https://doi.org/10.1006/jmbi.1998.1859 (1998).
87. Rossmann, M. G. Fitting atomic models into electron-microscopy maps. *Acta crystallographica. Section D, Biological crystallography* **56**, 1341–1349 (2000).
88. Orzechowski, M. & Tama, F. Flexible fitting of high-resolution x-ray structures into cryoelectron microscopy maps using biased molecular dynamics simulations. *Biophysical journal* **95**, 5692–5705, https://doi.org/10.1529/biophysj.108.139451 (2008).
89. Irobalieva, R. N. *et al*. Erratum: Structural diversity of supercoiled DNA. *Nat Commun* **6**, 8851, https://doi.org/10.1038/ncomms9851 (2015).
90. Frank, J. Single-particle imaging of macromolecules by cryo-electron microscopy. *Annual review of biophysics and biomolecular structure* **31**, 303–319, https://doi.org/10.1146/annurev.biophys.31.082901.134202 (2002).
91. Beckmann, R. *et al*. Alignment of conduits for the nascent polypeptide chain in the ribosome-Sec. 61 complex. *Science* **278**, 2123–2126 (1997).
92. Bottcher, B., Wynne, S. A. & Crowther, R. A. Determination of the fold of the core protein of hepatitis B virus by electron cryomicroscopy. *Nature* **386**, 88–91, https://doi.org/10.1038/386088a0 (1997).
93. Rosenthal, P. B. & Henderson, R. Optimal determination of particle orientation, absolute hand, and contrast loss in single-particle electron cryomicroscopy. *J Mol Biol* **333**, 721–745 (2003).
94. Elliott, J. M. *et al*. Antiparallel conformation of knob and hole aglycosylated half-antibody homodimers is mediated by a CH2-CH3 hydrophobic interaction. *J Mol Biol* **426**, 1947–1957, https://doi.org/10.1016/j.jmb.2014.02.015 (2014).
95. Ridgway, J. B. B., Presta, L. G. & Carter, P. 'Knobs-into-holes' engineering of antibody CH3 domains for heavy chain heterodimerization. "Protein Engineering. *Design and Selection*" **9**, 617–621, https://doi.org/10.1093/protein/9.7.617 (1996).
96. McGaughey, G. B., Gagne, M. & Rappe, A. K. pi-Stacking interactions. *Alive and well in proteins. J Biol Chem* **273**, 15458–15463, https://doi.org/10.1074/jbc.273.25.15458 (1998).
97. Davies, A. M. *et al*. Structural determinants of unique properties of human IgG4-Fc. *J Mol Biol* **426**, 630–644, https://doi.org/10.1016/j.jmb.2013.10.039 (2014).
98. Mindell, J. A. & Grigorieff, N. Accurate determination of local defocus and specimen tilt in electron microscopy. *J Struct Biol* **142**, 334–347 (2003).
99. Frank, J. *et al*. SPIDER and WEB: processing and visualization of images in 3D electron microscopy and related fields. *J Struct Biol* **116**, 190–199, https://doi.org/10.1006/jsbi.1996.0030 (1996).
100. Zhang, K. Gctf: Real-time CTF determination and correction. *J Struct Biol* **193**, 1–12, https://doi.org/10.1016/j.jsb.2015.11.003 (2016).
101. Kale, L. *et al*. NAMD2: Greater scalability for parallel molecular dynamics. *Journal of Computational Physics* **151**, 283–312, https://doi.org/10.1006/jcph.1999.6201 (1999).
102. MacKerell, A. D. *et al*. All-atom empirical potential for molecular modeling and dynamics studies of proteins. *The journal of physical chemistry. B* **102**, 3586–3616, https://doi.org/10.1021/jp973084f (1998).
103. Kremer, J. R., Mastronarde, D. N. & McIntosh, J. R. Computer visualization of three-dimensional image data using IMOD. *J Struct Biol* **116**, 71–76, https://doi.org/10.1006/jsbi.1996.0013 (1996).
104. Fernandez, J. J., Li, S. & Crowther, R. A. CTF determination and correction in electron cryotomography. *Ultramicroscopy* **106**, 587–596, https://doi.org/10.1016/j.ultramic.2006.02.004 (2006).
105. Kupsch, A. *et al*. Missing wedge computed tomography by iterative algorithm DIRECTT. *Journal of microscopy* **261**, 36–45, https://doi.org/10.1111/jmi.12313 (2015).

106. Kovacik, L. *et al.* A simple Fourier filter for suppression of the missing wedge ray artefacts in single-axis electron tomographic reconstructions. *J Struct Biol* **186**, 141–152, https://doi.org/10.1016/j.jsb.2014.02.004 (2014).
107. Deng, Y. *et al.* ICON: 3D reconstruction with 'missing-information' restoration in biological electron tomography. *J Struct Biol* **195**, 100–112, https://doi.org/10.1016/j.jsb.2016.04.004 (2016).
108. Pryor, A. Jr. *et al.* GENFIRE: A generalized Fourier iterative reconstruction algorithm for high-resolution 3D imaging. *Sci Rep-Uk* **7**, 10409, https://doi.org/10.1038/s41598-017-09847-1 (2017).
109. Agard, D. A. & Stroud, R. M. Linking regions between helices in bacteriorhodopsin revealed. *Biophysical journal* **37**, 589–602 (1982).
110. Paavolainen, L. *et al.* Compensation of missing wedge effects with sequential statistical reconstruction in electron tomography. *PLoS One* **9**, e108978, https://doi.org/10.1371/journal.pone.0108978 (2014).
111. Humphrey, W., Dalke, A. & Schulten, K. VMD: visual molecular dynamics. *Journal of molecular graphics* **14**, 33–38, 27–38 (1996).

Acknowledgements

This material is based on work supported by the National Science Foundation under Grant DMR-1344290. Work at the Molecular Foundry was supported by the Office of Science, Office of Basic Energy Sciences of the U.S. Department of Energy under Contract No. DE-AC02-05CH11231. G.R. is partially supported by the National Heart, Lung, and Blood Institute of the National Institutes of Health (no. R01HL115153) and the National Institute of General Medical Sciences of the National Institutes of Health (no. R01GM104427).

Author Contributions

This project was initiated and designed by M.L. and G.R. H.L. prepared the hole-hole homodimer sample, while T.E.C. prepared the NISTmAb. D.L., J.L. and T.E.C. prepared the TEM samples and acquired the data. D.L. and G.R. processed the data; D.L. solved the IPET 3D structure; and G.R. conducted single-particle 3D reconstruction. D.L. docked the model. D.L., M.L., J.P.M. and G.R. interpreted and manipulated the structures. D.L. drafted the initial manuscript; D.L., J.L., H.L., T.E.C., J.P.M., M.L. and G.R. edited and revised the manuscript.

Additional Information

Supplementary information accompanies this paper at https://doi.org/10.1038/s41598-019-44978-7.

Competing Interests: Certain commercial equipment, instruments, or materials are identified in this paper in order to specify the experimental procedure adequately. Such identification is not intended to imply recommendation or endorsement by the National Institute of Standards and Technology, nor is it intended to imply that the materials or equipment identified are necessarily the best available for the purpose. H.L. and M.L. are currently employed at Genentech.

Publisher's note: Springer Nature remains neutral with regard to jurisdictional claims in published maps and institutional affiliations.

Supplementary Information

for

Single-Molecule 3D Images of "Hole-Hole" IgG1 Homodimers by Individual-Particle Electron Tomography

Dongsheng Lei,[1] Jianfang Liu,[1] Hongbin Liu,[2] Thomas E. Cleveland,[3] John P. Marino,[3] Ming Lei,[2,] *Gang Ren[1,]*

[1] The Molecular Foundry, Lawrence Berkeley National Laboratory, Berkeley, CA 94720, USA
[2] Genentech Inc, South San Francisco, CA 94080, USA
[3] Institute for Bioscience and Biotechnology Research, National Institute of Standards and Technology and the University of Maryland, Rockville, MD 20850, USA

* Correspondence should be addressed to: G. R. (gren@lbl.gov) or M.L. (lei.ming@gene.com)

Supplementary Table 1. The parameters used for IPET 3D reconstructions

#	EMDB#[1]	Shape	Dose/img.[2] ($e^-/Å^2$)	Dose/set[3] ($e^-/Å^2$)	Acq. angle range[4]	Total img.[5]	Reconst. angle range[6]	Cont.[7]	Resol.[8] (Å)	D_{CH3} (Å)	ϑ_{CH2} (°)	D_{Fab} (Å)	ϑ_{Fab} (°)	Fig. [9]
1	EMD-7353	Y-shape 01	70.31	4570.47	-48° to +48°	65	-45° to 45°	0.442	13.2	-	-	-	-	S2
2	EMD-7354	Y-shape 02	43.24	2983.37	-51° to +51°	69	-45° to 45°	0.239	13.6	-	-	-	-	S3
3	EMD-7355	Y-shape 03	99.42	6461.98	-48° to +48°	65	-45° to 45°	0.343	12.5	-	-	-	-	S4
4	EMD-7356	Y-shape 04	100.03	6501.88	-48° to +48°	65	-45° to 45°	0.249	12.8	-	-	-	-	S5
5	EMD-7357	Y-shape 05	98.94	6431.26	-48° to +48°	65	-45° to 45°	0.324	12.7	-	-	-	-	S6
6	EMD-7358	Y-shape 06	71.24	4630.30	-48° to +48°	65	-45° to 45°	0.362	14.1	-	-	-	-	S7
7	EMD-7359	Y-shape 07	100.13	6508.28	-48° to +48°	65	-45° to 45°	0.260	12.8	-	-	-	-	S8
8	EMD-7360	Y-shape 08	70.09	4556.14	-48° to +48°	65	-45° to 45°	0.265	12.9	-	-	-	-	S9
9	EMD-7361	Y-shape 09	70.57	4586.78	-48° to +48°	65	-45° to 45°	0.241	14.1	-	-	-	-	S10
10	EMD-7362	Y-shape 10	70.10	4556.44	-48° to +48°	65	-45° to 45°	0.203	13.5	-	-	-	-	S11
11	EMD-7363	Y-shape 11	40.72	2809.94	-51° to +51°	69	-45° to 45°	0.335	13.5	-	-	-	-	-
12	EMD-7364	Y-shape 12	43.73	3017.69	-51° to +51°	69	-45° to 45°	0.257	13.3	-	-	-	-	-
13	EMD-7365	Y-shape 13	41.79	2883.78	-51° to +51°	69	-45° to 45°	0.419	13.3	-	-	-	-	-
14	EMD-7366	Y-shape 14	41.36	2854.06	-51° to +51°	69	-45° to 45°	0.251	13.2	-	-	-	-	-
15	EMD-7367	Y-shape 15	70.30	4569.18	-48° to +48°	65	-45° to 45°	0.208	12.3	-	-	-	-	-
16	EMD-7368	Y-shape 16	97.65	6347.29	-48° to +48°	65	-45° to 45°	0.228	12.9	-	-	-	-	-
17	EMD-7369	X-shape 01	70.75	4598.56	-48° to +48°	65	-45° to 45°	0.306	13.7	106.4	77.3	79.3	125.4	S12
18	EMD-7370	X-shape 02	42.66	2943.60	-51° to +51°	69	-45° to 45°	0.288	13.2	87.8	173.2	88.8	119.2	S13
19	EMD-7371	X-shape 03	99.26	6451.61	-48° to +48°	65	-45° to 45°	0.289	12.5	96.7	149.9	57.4	40.4	S14
20	EMD-7372	X-shape 04	71.10	4621.51	-48° to +48°	65	-45° to 45°	0.394	13.9	80.1	81.8	74.0	73.8	S15
21	EMD-7373	X-shape 05	43.17	2978.80	-51° to +51°	69	-45° to 45°	0.270	13.6	88.2	44.5	77.9	137.7	S16
22	EMD-7374	X-shape 06	39.99	2759.35	-51° to +51°	69	-45° to 45°	0.341	13.4	97.9	138.1	80.9	109.4	S17
23	EMD-7375	X-shape 07	100.03	6501.94	-48° to +48°	65	-45° to 45°	0.387	12.8	94.4	137.3	66.8	75.0	S18
24	EMD-7376	X-shape 08	70.34	4571.86	-48° to +48°	65	-45° to 45°	0.358	12.6	39.3	80.0	72.8	107.0	S19
25	EMD-7377	X-shape 09	70.07	4554.84	-48° to +48°	65	-45° to 45°	0.332	12.7	106.9	120.6	87.2	137.8	S20
26	EMD-7378	X-shape 10	71.03	4616.89	-48° to +48°	65	-45° to 45°	0.392	14.1	100.6	136.2	91.4	69.3	S21
27	EMD-7379	X-shape 11	70.50	4582.44	-48° to +48°	65	-45° to 45°	0.326	12.8	92.1	15.6	92.7	114.4	S22
28	EMD-7380	X-shape 12	70.31	4570.41	-48° to +48°	65	-45° to 45°	0.346	11.9	87.2	115.4	74.2	122.9	S23
29	EMD-7381	X-shape 13	41.74	2880.14	-51° to +51°	69	-45° to 45°	0.394	13.5	99.2	122.5	90.6	120.6	S24
30	EMD-7382	X-shape 14	40.76	2812.50	-51° to +51°	69	-45° to 45°	0.325	14.0	53.8	22.9	72.9	56.2	S25
31	EMD-7383	X-shape 15	99.09	6440.60	-48° to +48°	65	-45° to 45°	0.299	12.5	47.1	27.6	87.7	112.8	S26
32	EMD-7384	X-shape 16	95.16	6185.12	-48° to +48°	65	-45° to 45°	0.383	13.5	88.5	58.4	82.6	141.3	S27
33	EMD-7385	X-shape 17	100.38	6524.42	-48° to +48°	65	-45° to 45°	0.370	12.3	89.6	137.1	84.1	85.0	S28
34	EMD-7386	X-shape 18	71.09	4620.67	-48° to +48°	65	-45° to 45°	0.263	13.7	95.8	52.6	97.4	143.1	S29
35	EMD-7387	X-shape	44.02	3037.25	-51° to +51°	69	-45° to 45°	0.262	12.9	106.7	126.7	98.4	150.1	S30

		19												
36	EMD-7388	X-shape 20	70.48	4581.01	-48˚ to +48˚	65	-45˚ to 45˚	0.387	12.0	81.0	36.3	86.3	141.1	S31
37	EMD-7389	X-shape 21	70.14	4558.92	-48˚ to +48˚	65	-45˚ to 45˚	0.324	12.2	85.7	48.7	106.8	159.9	S32
38	EMD-7390	X-shape 22	70.15	4559.58	-48˚ to +48˚	65	-45˚ to 45˚	0.401	12.3	76.1	69.9	108.0	110.6	S33
39	EMD-7391	X-shape 23	70.63	4591.20	-48˚ to +48˚	65	-45˚ to 45˚	0.275	13.6	73.1	16.4	91.2	125.7	S34
40	EMD-7392	X-shape 24	99.79	6486.67	-48˚ to +48˚	65	-45˚ to 45˚	0.372	12.2	101.8	164.4	59.4	80.5	S35
41	EMD-7393	X-shape 25	70.44	4578.89	-48˚ to +48˚	65	-45˚ to 45˚	0.364	12.3	97.1	92.2	77.3	71.8	-
42	EMD-7394	X-shape 26	70.68	4593.88	-48˚ to +48˚	65	-45˚ to 45˚	0.472	12.4	94.5	162.3	111.4	171.5	-
43	EMD-7395	X-shape 27	44.29	3056.08	-51˚ to +51˚	69	-45˚ to 45˚	0.304	13.6	81.3	25.9	84.6	118.8	-
44	EMD-7396	X-shape 28	43.16	2978.33	-51˚ to +51˚	69	-45˚ to 45˚	0.334	13.1	89.1	85.7	91.8	139.6	-
45	EMD-7397	X-shape 29	100.25	6516.05	-48˚ to +48˚	65	-45˚ to 45˚	0.380	12.6	50.0	49.9	90.1	74.7	-
46	EMD-7398	X-shape 30	70.44	4578.57	-48˚ to +48˚	65	-45˚ to 45˚	0.335	12.6	119.9	77.3	92.5	122.5	-
47	EMD-7399	X-shape 31	70.57	4587.12	-48˚ to +48˚	65	-45˚ to 45˚	0.304	12.2	85.5	53.2	78.9	96.0	-
48	EMD-7400	X-shape 32	40.53	2796.79	-51˚ to +51˚	69	-45˚ to 45˚	0.411	13.8	114.2	128.0	86.2	116.0	-
49	EMD-7401	X-shape 33	70.63	4590.67	-48˚ to +48˚	65	-45˚ to 45˚	0.392	13.2	91.5	59.7	86.9	113.5	-
50	EMD-7402	X-shape 34	70.23	4564.90	-48˚ to +48˚	65	-45˚ to 45˚	0.333	11.9	66.8	37.3	80.1	80.3	-
51	EMD-7404	X-shape 35	43.85	3025.72	-51˚ to +51˚	69	-45˚ to 45˚	0.229	13.6	37.0	86.5	98.7	145.3	-
52	EMD-7405	X-shape 36	70.63	4590.93	-48˚ to +48˚	65	-45˚ to 45˚	0.372	12.1	61.6	35.7	85.3	136.4	-
53	EMD-7406	X-shape 37	70.70	4595.56	-48˚ to +48˚	65	-45˚ to 45˚	0.248	12.1	93.9	82.6	90.3	123.6	-
54	EMD-7407	X-shape 38	70.50	4582.72	-48˚ to +48˚	65	-45˚ to 45˚	0.303	13.9	100.3	55.0	89.1	146.4	-
55	EMD-7408	X-shape 39	70.61	4589.47	-48˚ to +48˚	65	-45˚ to 45˚	0.296	13.6	85.5	12.6	62.1	15.7	-
56	EMD-7409	X-shape 40	70.90	4608.70	-48˚ to +48˚	65	-45˚ to 45˚	0.299	13.4	45.6	8.0	80.0	83.9	-
57	EMD-7410	X-shape 41	70.12	4557.54	-48˚ to +48˚	65	-45˚ to 45˚	0.275	12.5	95.4	117.4	73.2	113.5	-
58	EMD-7411	X-shape 42	70.87	4606.42	-48˚ to +48˚	65	-45˚ to 45˚	0.395	12.3	86.9	125.8	93.1	145.1	-
59	EMD-7412	X-shape 43	69.81	4537.84	-48˚ to +48˚	65	-45˚ to 45˚	0.228	12.6	76.4	41.4	76.6	79.2	-
60	EMD-7413	X-shape 44	69.72	4531.56	-48˚ to +48˚	65	-45˚ to 45˚	0.275	12.0	83.1	34.5	92.4	139.3	-
61	EMD-7414	X-shape 45	70.65	4592.31	-48˚ to +48˚	65	-45˚ to 45˚	0.330	12.2	65.1	76.0	76.8	52.6	-
62	EMD-7415	X-shape 46	71.13	4623.45	-48˚ to +48˚	65	-45˚ to 45˚	0.239	14.3	94.5	20.9	103.2	169.6	-
63	EMD-7416	X-shape 47	70.84	4604.39	-48˚ to +48˚	65	-45˚ to 45˚	0.309	12.6	84.9	99.1	96.9	139.1	-
64	EMD-7417	X-shape 48	69.96	4547.66	-48˚ to +48˚	65	-45˚ to 45˚	0.376	12.6	76.9	23.0	75.8	77.5	-
65	EMD-7418	i-shape 01	99.06	6438.89	-48˚ to +48˚	65	-45˚ to 45˚	0.444	12.8	-	-	-	-	S36
66	EMD-7419	i-shape 02	41.73	2879.62	-51˚ to +51˚	69	-45˚ to 45˚	0.356	13.3	-	-	-	-	S37
67	EMD-7420	i-shape 03	70.60	4588.70	-48˚ to +48˚	65	-45˚ to 45˚	0.579	13.6	-	-	-	-	S38
68	EMD-7421	i-shape 04	97.47	6335.45	-48˚ to +48˚	65	-45˚ to 45˚	0.465	13.0	-	-	-	-	S39
69	EMD-7422	i-shape 05	70.55	4585.67	-48˚ to +48˚	65	-45˚ to 45˚	0.472	12.3	-	-	-	-	S40
70	EMD-7423	i-shape 06	98.09	6375.59	-48˚ to +48˚	65	-45˚ to 45˚	0.397	12.8	-	-	-	-	S41
71	EMD-7424	i-shape 07	39.63	2734.57	-51˚ to +51˚	69	-45˚ to 45˚	0.564	13.2	-	-	-	-	S42

#	EMDB#[1]	Shape	Dose/img.[2] ($e^-/Å^2$)	Dose/set[3] ($e^-/Å^2$)	Acq. angle range[4]	Total img.[5]	Reconst. angle range[6]	Cont.[7]	Resol.[8] (Å)	D_{CH3} (Å)	ϑ_{CH2} (°)	D_{Fab} (Å)	ϑ_{Fab} (°)	Fig. [9]
72	EMD-7425	i-shape 08	70.44	4578.43	-48° to +48°	65	-45° to 45°	0.279	12.8	-	-	-	-	S43
73	EMD-7426	i-shape 09	70.62	4590.57	-48° to +48°	65	-45° to 45°	0.339	12.6	-	-	-	-	S44
74	EMD-7427	i-shape 10	71.21	4628.39	-48° to +48°	65	-45° to 45°	0.284	14.1	-	-	-	-	S45
75	EMD-7428	i-shape 11	43.26	2985.20	-51° to +51°	69	-45° to 45°	0.333	13.4	-	-	-	-	-
76	EMD-7429	i-shape 12	40.13	2769.02	-51° to +51°	69	-45° to 45°	0.428	13.3	-	-	-	-	-
77	EMD-7430	i-shape 13	70.67	4593.68	-48° to +48°	65	-45° to 45°	0.434	12.7	-	-	-	-	-
78	EMD-7431	i-shape 14	70.32	4570.79	-48° to +48°	65	-45° to 45°	0.435	13.7	-	-	-	-	-
79	EMD-7432	i-shape 15	70.81	4602.44	-48° to +48°	65	-45° to 45°	0.305	13.4	-	-	-	-	-
80	EMD-7433	i-shape 16	71.27	4632.59	-48° to +48°	65	-45° to 45°	0.429	13.9	-	-	-	-	-

TEM: Zeiss 120 stands for Zeiss Libra 120 Plus TEM;
CCD: UltraScan for Gatan UltraScan 4000 4Kx4K CCD
Angstrom per pixel: 2.96 Å

[1]EMDB Index: https://www.ebi.ac.uk/pdbe/emdb/

[2]Dose used for each CCD frame

[3]Dose used for whole tilt series

[4]Data acquisition angle range

[5]Total images in the tilt series

[6]Reconstruction angle range

[7]Contour used for display

[8]IPET 3D reconstruction resolution

[9]The process of IPET 3D reconstruction showed in Supplementary Figure

Supplementary Figures

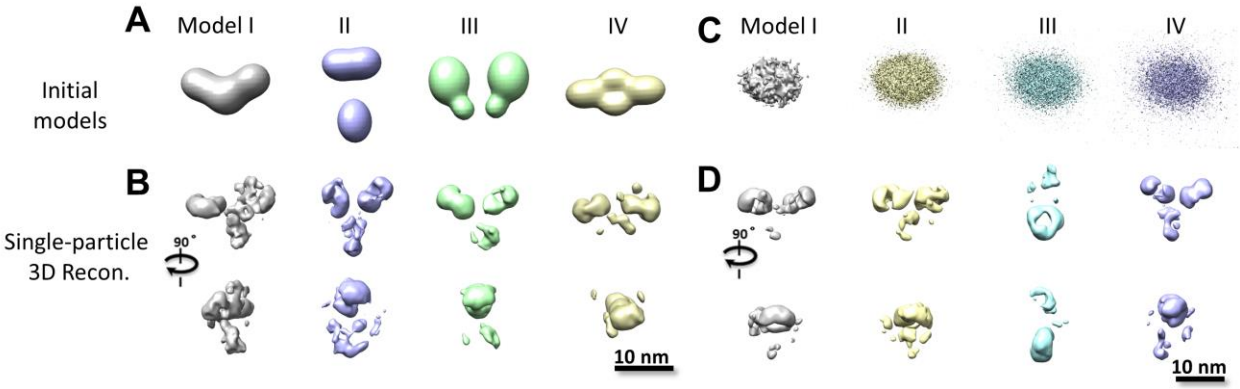

Supplementary Fig. 1 | Single-particle 3D reconstructions of hole-hole homodimer. Two sets of initial models were used to perform single particle reconstruction. **(A)** Four featureless blobs are used as the initial model for multi-model 3D refinement. **(B)** Final 3D reconstructions obtained based on corresponding initial models by using the multi-model 3D refinement algorithm. **(C)** Four single Gaussian blobs under different noise levels are used as the initial models for multi-model 3D refinement. **(D)** Final 3D reconstructions obtained based on corresponding initial models by using the multi-model 3D refinement algorithm. Scale bars=10 nm.

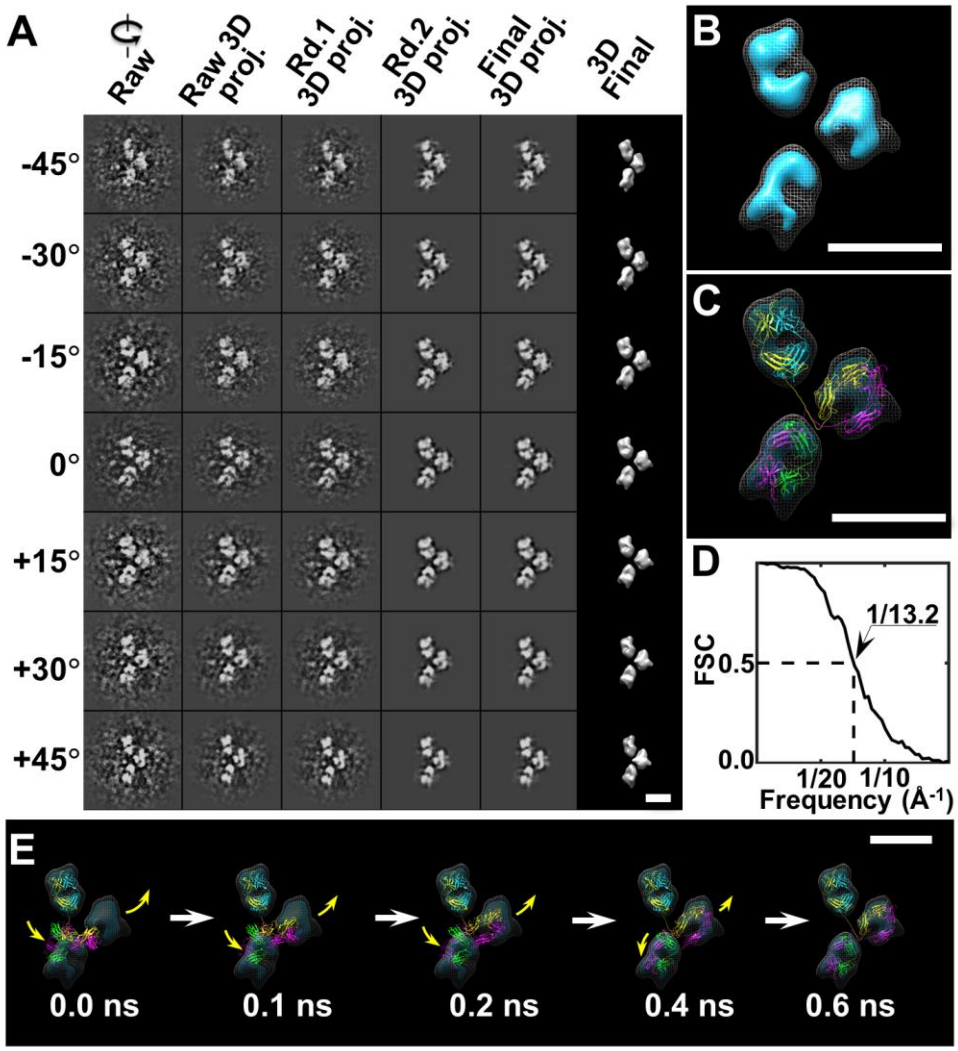

Supplementary Fig. 2 | 3D IPET reconstruction of the first Y-shaped IgG homodimer by IPET. (A) Seven representative tilt images of an individual Y-shaped particle are displayed in the first column from the left. Using IPET, the tilt images (after CTF correction) were gradually aligned to a common center for 3D reconstruction via iterative refinement. Projections of raw, intermediate and final 3D reconstructions at the corresponding tilt angles are displayed in the next five columns according to their corresponding tilt angles. **(B)** The final 3D density map. **(C)** The density map was flexibly docked with IgG crystal structure by using TMD simulation. **(D)** FSC analyses (from two density maps reconstructed from odd and even numbers of tilt images) showed that the resolution of the final 3D density map was ~13.2 Å. **(E)** Five snapshots illustrated the conformational changes of IgG model during TMD simulation. Scale bars=10 nm.

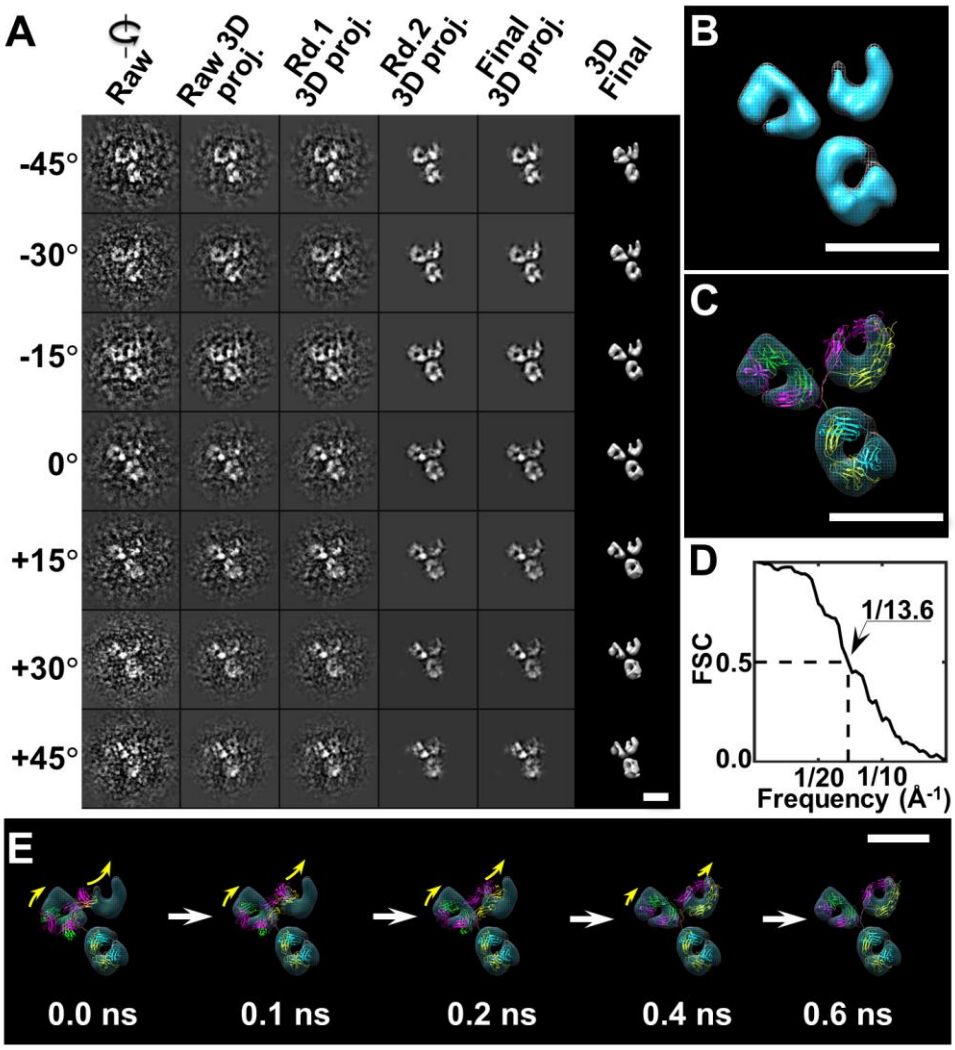

Supplementary Fig. 3 | 3D IPET reconstruction of the second Y-shaped IgG homodimer by IPET. **(A)** Seven representative tilt images of an individual Y-shaped particle are displayed in the first column from the left. Using IPET, the tilt images (after CTF correction) were gradually aligned to a common center for 3D reconstruction via iterative refinement. Projections of raw, intermediate and final 3D reconstructions at the corresponding tilt angles are displayed in the next five columns according to their corresponding tilt angles. **(B)** The final 3D density map. **(C)** The density map was flexibly docked with IgG crystal structure by using TMD simulation. **(D)** FSC analyses (from two density maps reconstructed from odd and even numbers of tilt images) showed that the resolution of the final 3D density map was ~13.6 Å. **(E)** Five snapshots illustrated the conformational changes of IgG model during TMD simulation. Scale bars=10 nm.

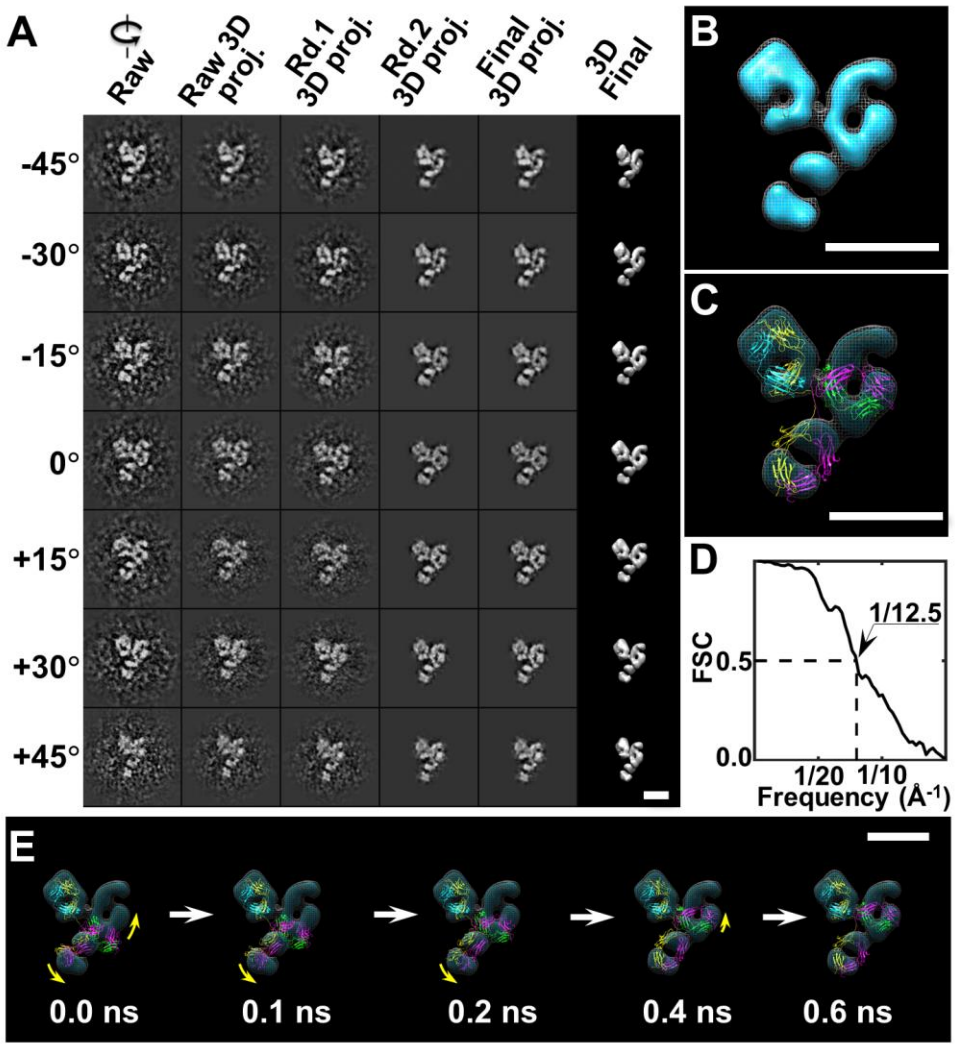

Supplementary Fig. 4 | 3D IPET reconstruction of the third Y-shaped IgG homodimer by IPET. (A) Seven representative tilt images of an individual Y-shaped particle are displayed in the first column from the left. Using IPET, the tilt images (after CTF correction) were gradually aligned to a common center for 3D reconstruction via iterative refinement. Projections of raw, intermediate and final 3D reconstructions at the corresponding tilt angles are displayed in the next five columns according to their corresponding tilt angles. **(B)** The final 3D density map. **(C)** The density map was flexibly docked with IgG crystal structure by using TMD simulation. **(D)** FSC analyses (from two density maps reconstructed from odd and even numbers of tilt images) showed that the resolution of the final 3D density map was ~12.5 Å. **(E)** Five snapshots illustrated the conformational changes of IgG model during TMD simulation. Scale bars=10 nm.

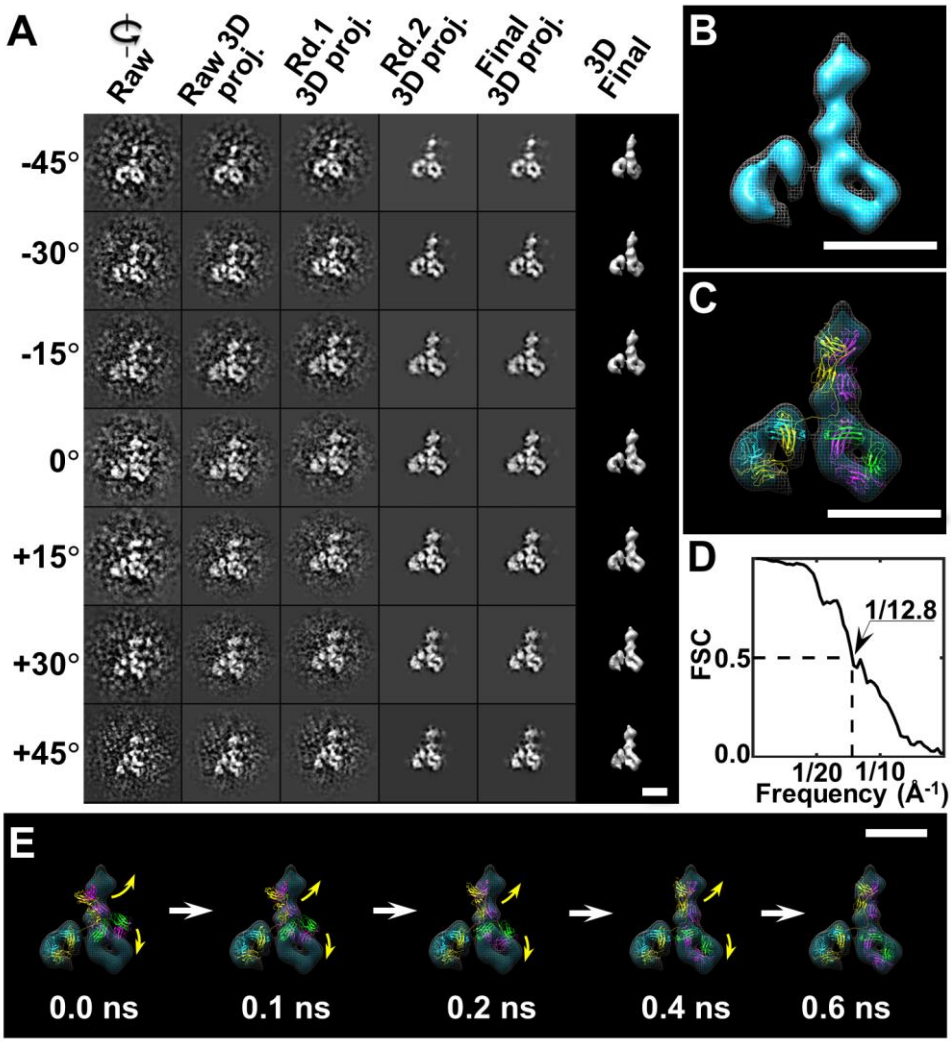

Supplementary Fig. 5 | 3D IPET reconstruction of the forth Y-shaped IgG homodimer by IPET. (A) Seven representative tilt images of an individual Y-shaped particle are displayed in the first column from the left. Using IPET, the tilt images (after CTF correction) were gradually aligned to a common center for 3D reconstruction via iterative refinement. Projections of raw, intermediate and final 3D reconstructions at the corresponding tilt angles are displayed in the next five columns according to their corresponding tilt angles. **(B)** The final 3D density map. **(C)** The density map was flexibly docked with IgG crystal structure by using TMD simulation. **(D)** FSC analyses (from two density maps reconstructed from odd and even numbers of tilt images) showed that the resolution of the final 3D density map was ~12.8 Å. **(E)** Five snapshots illustrated the conformational changes of IgG model during TMD simulation. Scale bars=10 nm.

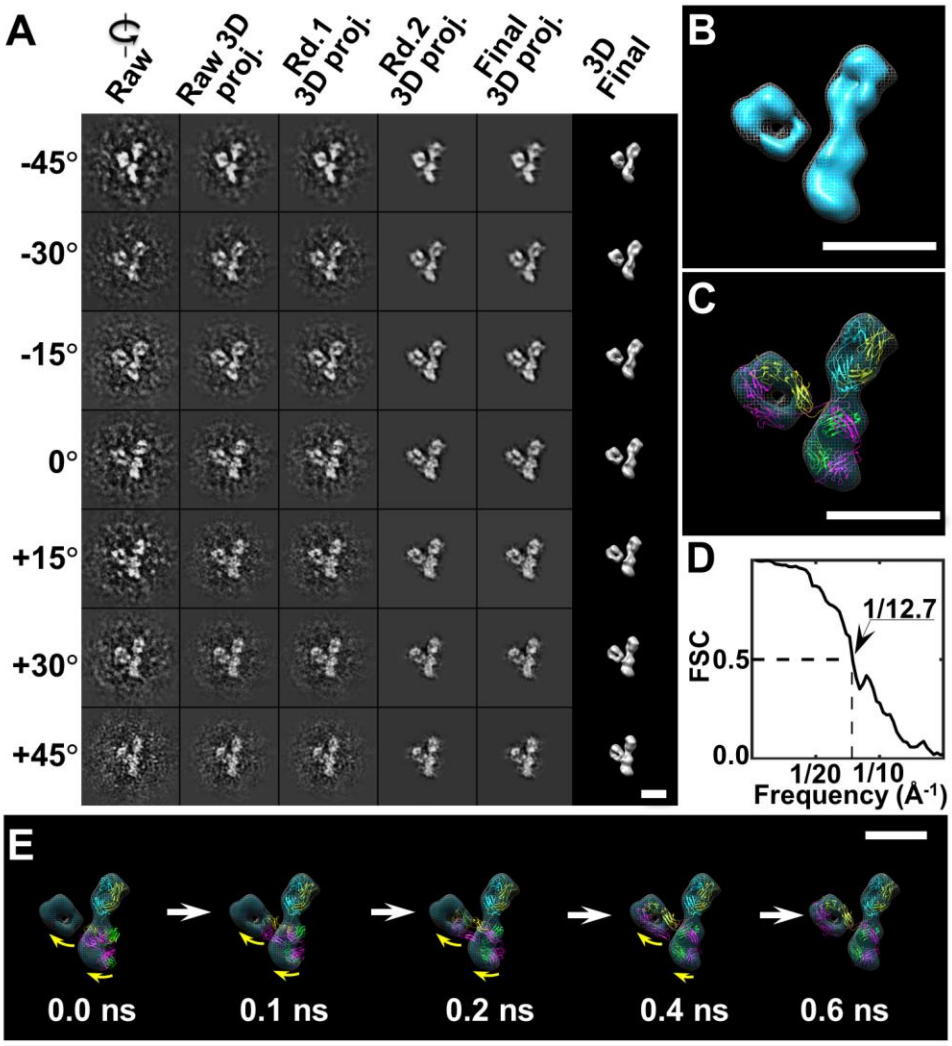

Supplementary Fig. 6 | 3D IPET reconstruction of the fifth Y-shaped IgG homodimer by IPET. (A) Seven representative tilt images of an individual Y-shaped particle are displayed in the first column from the left. Using IPET, the tilt images (after CTF correction) were gradually aligned to a common center for 3D reconstruction via iterative refinement. Projections of raw, intermediate and final 3D reconstructions at the corresponding tilt angles are displayed in the next five columns according to their corresponding tilt angles. **(B)** The final 3D density map. **(C)** The density map was flexibly docked with IgG crystal structure by using TMD simulation. **(D)** FSC analyses (from two density maps reconstructed from odd and even numbers of tilt images) showed that the resolution of the final 3D density map was ~12.7 Å. **(E)** Five snapshots illustrated the conformational changes of IgG model during TMD simulation. Scale bars=10 nm.

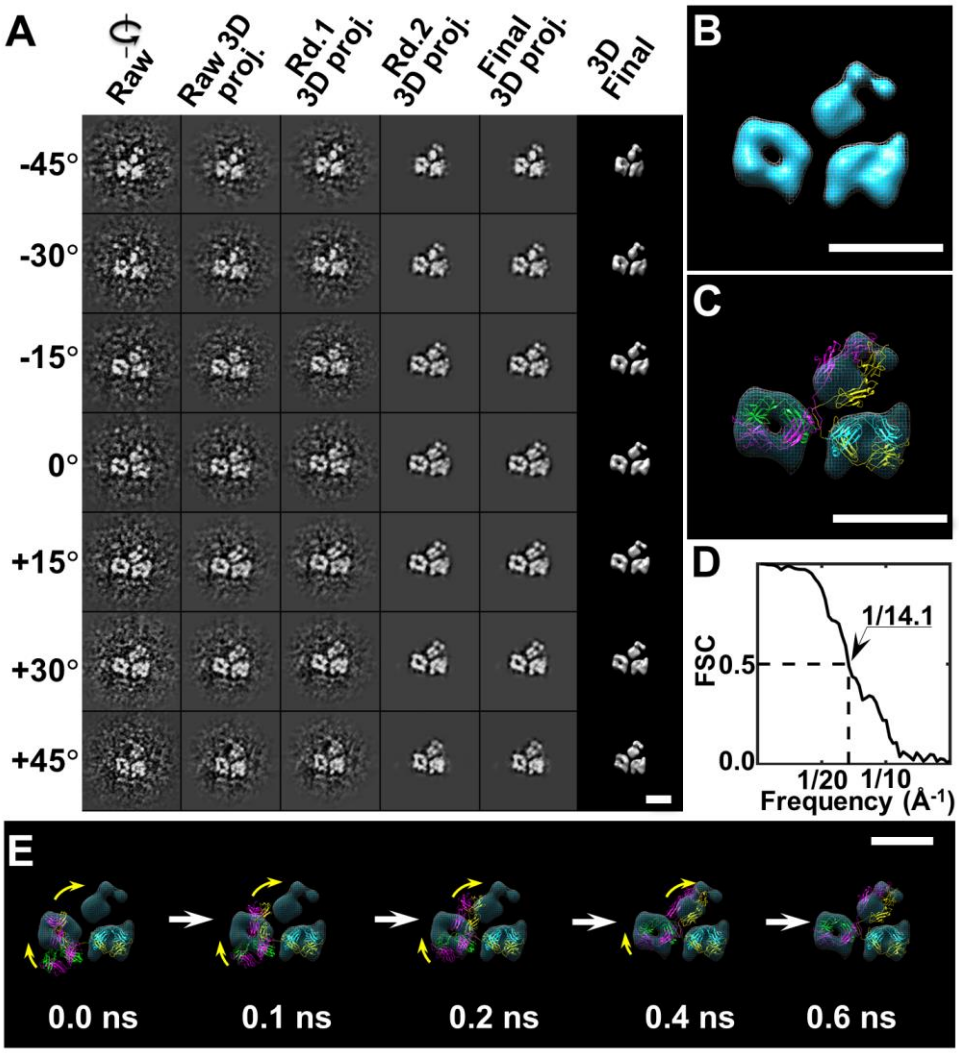

Supplementary Fig. 7 | 3D IPET reconstruction of the sixth Y-shaped IgG homodimer by IPET. (A) Seven representative tilt images of an individual Y-shaped particle are displayed in the first column from the left. Using IPET, the tilt images (after CTF correction) were gradually aligned to a common center for 3D reconstruction via iterative refinement. Projections of raw, intermediate and final 3D reconstructions at the corresponding tilt angles are displayed in the next five columns according to their corresponding tilt angles. **(B)** The final 3D density map. **(C)** The density map was flexibly docked with IgG crystal structure by using TMD simulation. **(D)** FSC analyses (from two density maps reconstructed from odd and even numbers of tilt images) showed that the resolution of the final 3D density map was ~14.1 Å. **(E)** Five snapshots illustrated the conformational changes of IgG model during TMD simulation. Scale bars=10 nm.

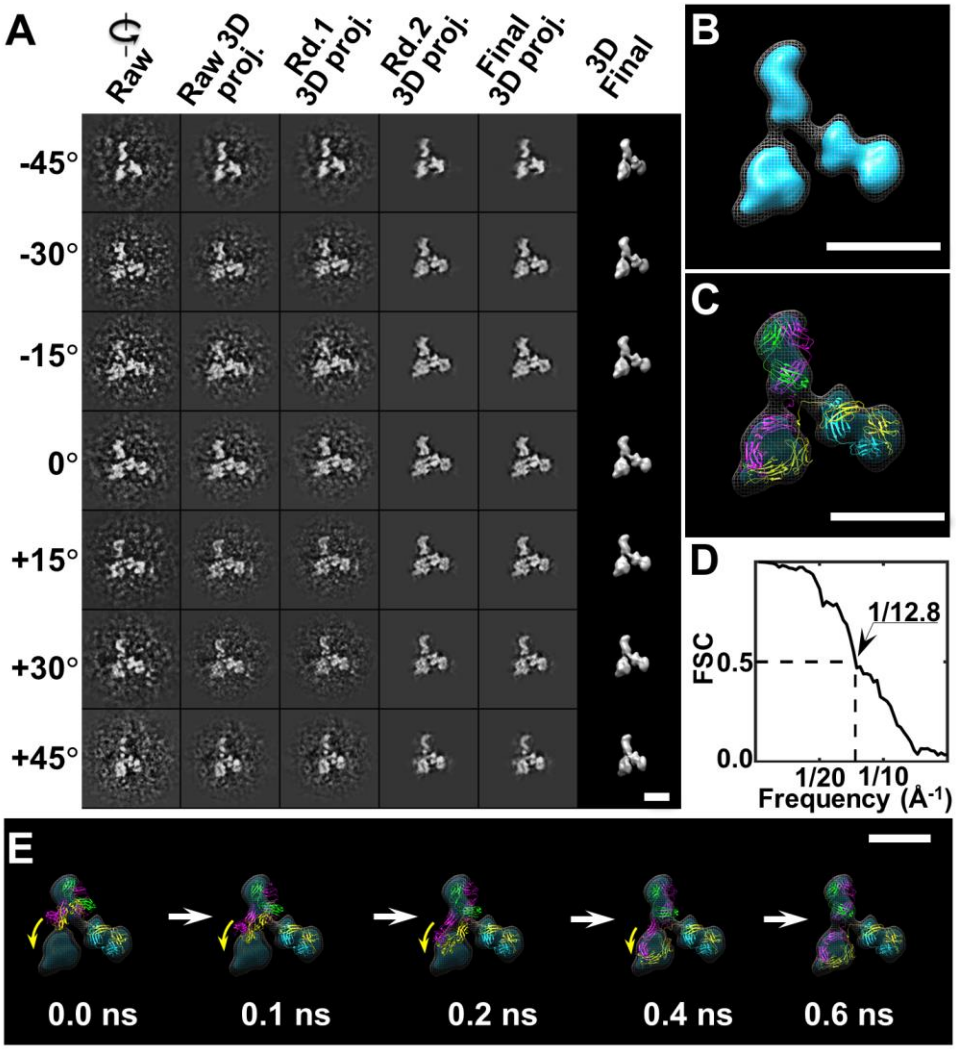

Supplementary Fig. 8 | 3D IPET reconstruction of the seventh Y-shaped IgG homodimer by IPET. **(A)** Seven representative tilt images of an individual Y-shaped particle are displayed in the first column from the left. Using IPET, the tilt images (after CTF correction) were gradually aligned to a common center for 3D reconstruction via iterative refinement. Projections of raw, intermediate and final 3D reconstructions at the corresponding tilt angles are displayed in the next five columns according to their corresponding tilt angles. **(B)** The final 3D density map. **(C)** The density map was flexibly docked with IgG crystal structure by using TMD simulation. **(D)** FSC analyses (from two density maps reconstructed from odd and even numbers of tilt images) showed that the resolution of the final 3D density map was ~12.8 Å. **(E)** Five snapshots illustrated the conformational changes of IgG model during TMD simulation. Scale bars=10 nm.

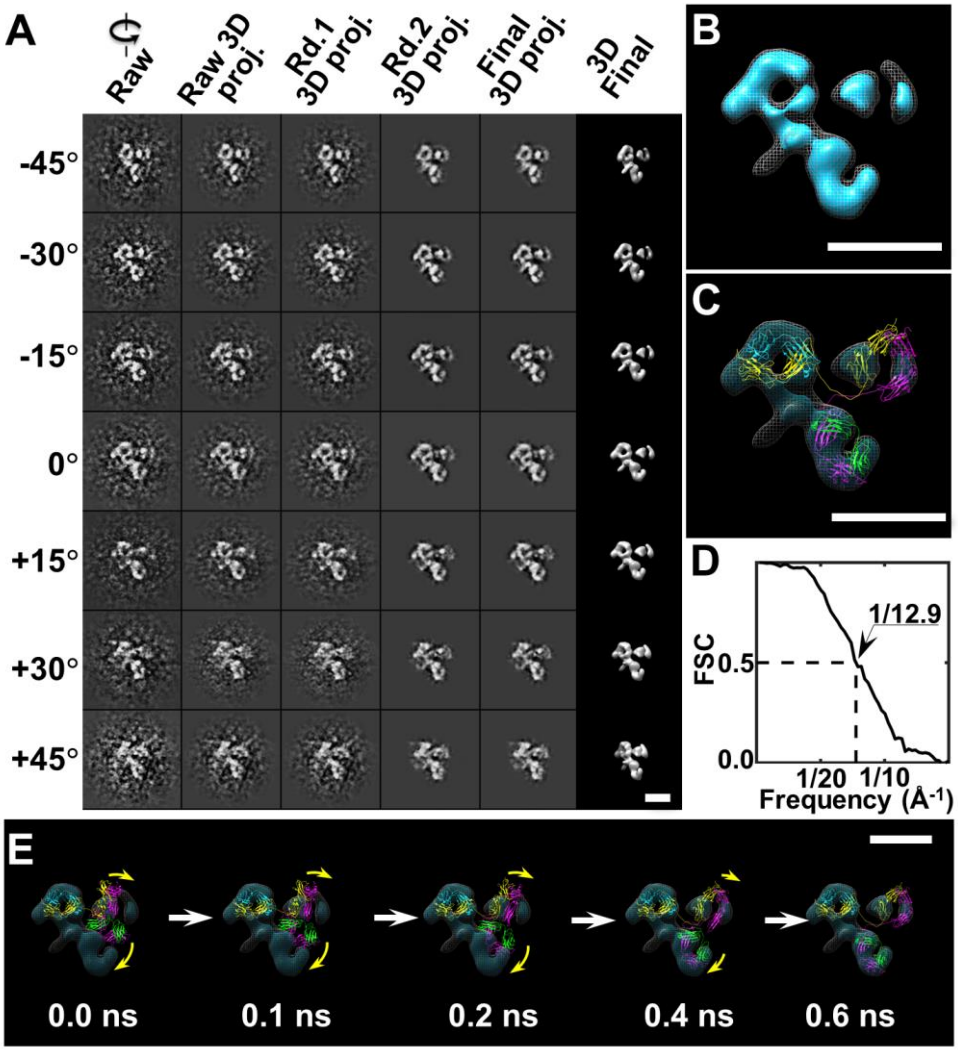

Supplementary Fig. 9 | 3D IPET reconstruction of the eighth Y-shaped IgG homodimer by IPET. **(A)** Seven representative tilt images of an individual Y-shaped particle are displayed in the first column from the left. Using IPET, the tilt images (after CTF correction) were gradually aligned to a common center for 3D reconstruction via iterative refinement. Projections of raw, intermediate and final 3D reconstructions at the corresponding tilt angles are displayed in the next five columns according to their corresponding tilt angles. **(B)** The final 3D density map. **(C)** The density map was flexibly docked with IgG crystal structure by using TMD simulation. **(D)** FSC analyses (from two density maps reconstructed from odd and even numbers of tilt images) showed that the resolution of the final 3D density map was ~12.9 Å. **(E)** Five snapshots illustrated the conformational changes of IgG model during TMD simulation. Scale bars=10 nm.

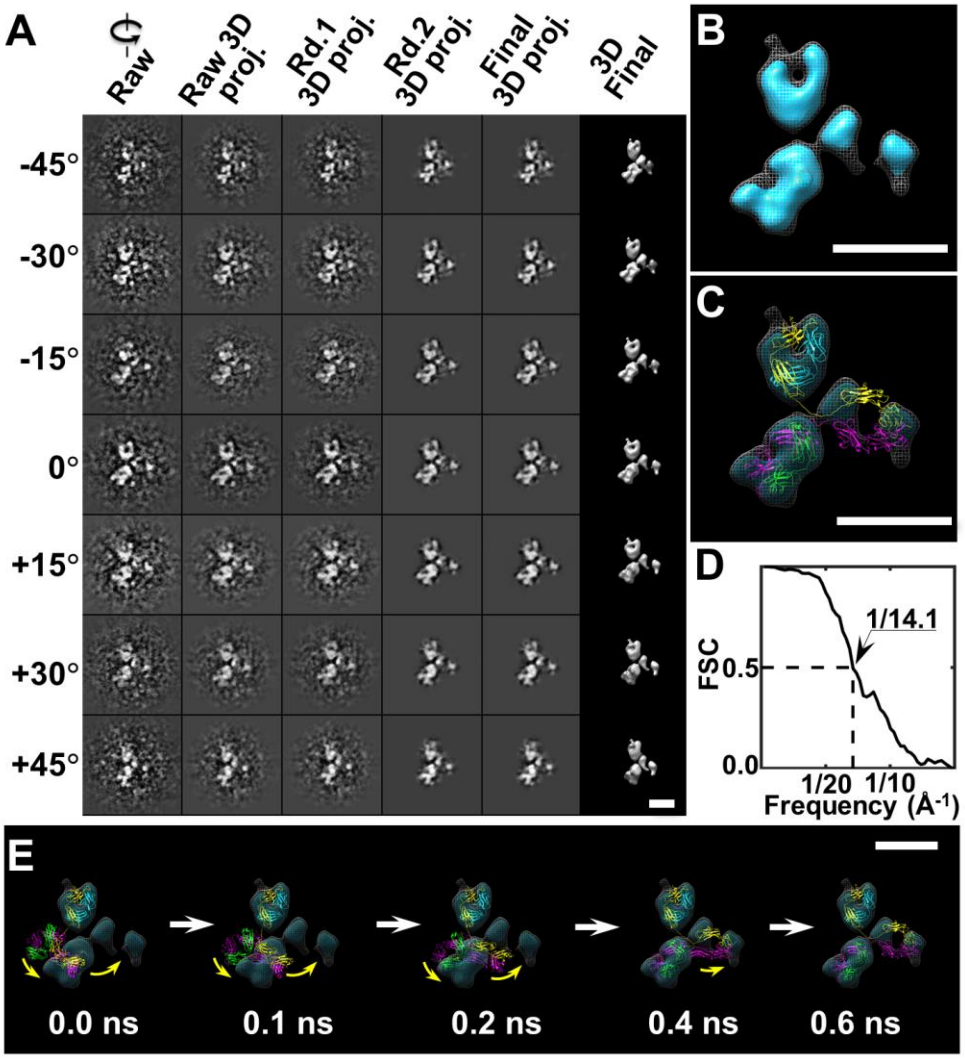

Supplementary Fig. 10 | 3D IPET reconstruction of the ninth Y-shaped IgG homodimer by IPET. **(A)** Seven representative tilt images of an individual Y-shaped particle are displayed in the first column from the left. Using IPET, the tilt images (after CTF correction) were gradually aligned to a common center for 3D reconstruction via iterative refinement. Projections of raw, intermediate and final 3D reconstructions at the corresponding tilt angles are displayed in the next five columns according to their corresponding tilt angles. **(B)** The final 3D density map. **(C)** The density map was flexibly docked with IgG crystal structure by using TMD simulation. **(D)** FSC analyses (from two density maps reconstructed from odd and even numbers of tilt images) showed that the resolution of the final 3D density map was ~14.1 Å. **(E)** Five snapshots illustrated the conformational changes of IgG model during TMD simulation. Scale bars=10 nm.

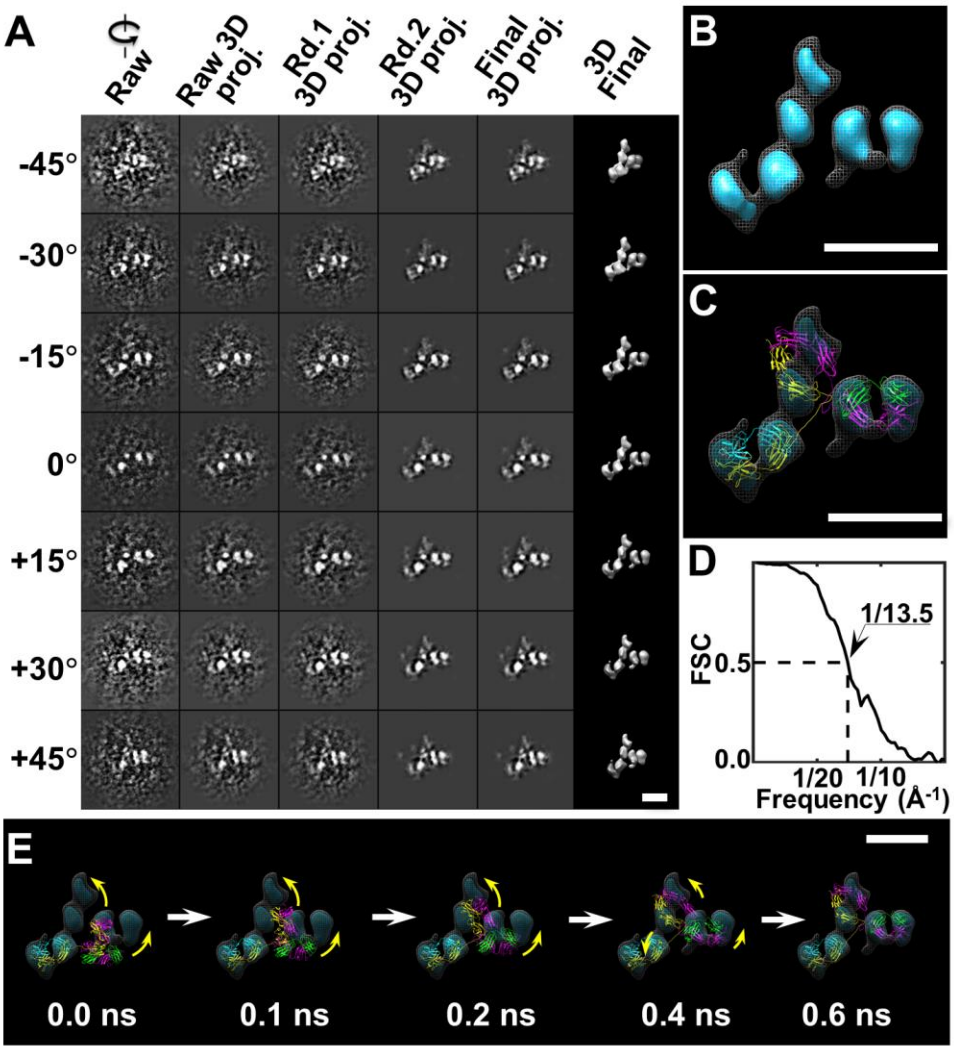

Supplementary Fig. 11 | 3D IPET reconstruction of the tenth Y-shaped IgG homodimer by IPET. **(A)** Seven representative tilt images of an individual Y-shaped particle are displayed in the first column from the left. Using IPET, the tilt images (after CTF correction) were gradually aligned to a common center for 3D reconstruction via iterative refinement. Projections of raw, intermediate and final 3D reconstructions at the corresponding tilt angles are displayed in the next five columns according to their corresponding tilt angles. **(B)** The final 3D density map. **(C)** The density map was flexibly docked with IgG crystal structure by using TMD simulation. **(D)** FSC analyses (from two density maps reconstructed from odd and even numbers of tilt images) showed that the resolution of the final 3D density map was ~13.5 Å. **(E)** Five snapshots illustrated the conformational changes of IgG model during TMD simulation. Scale bars=10 nm.

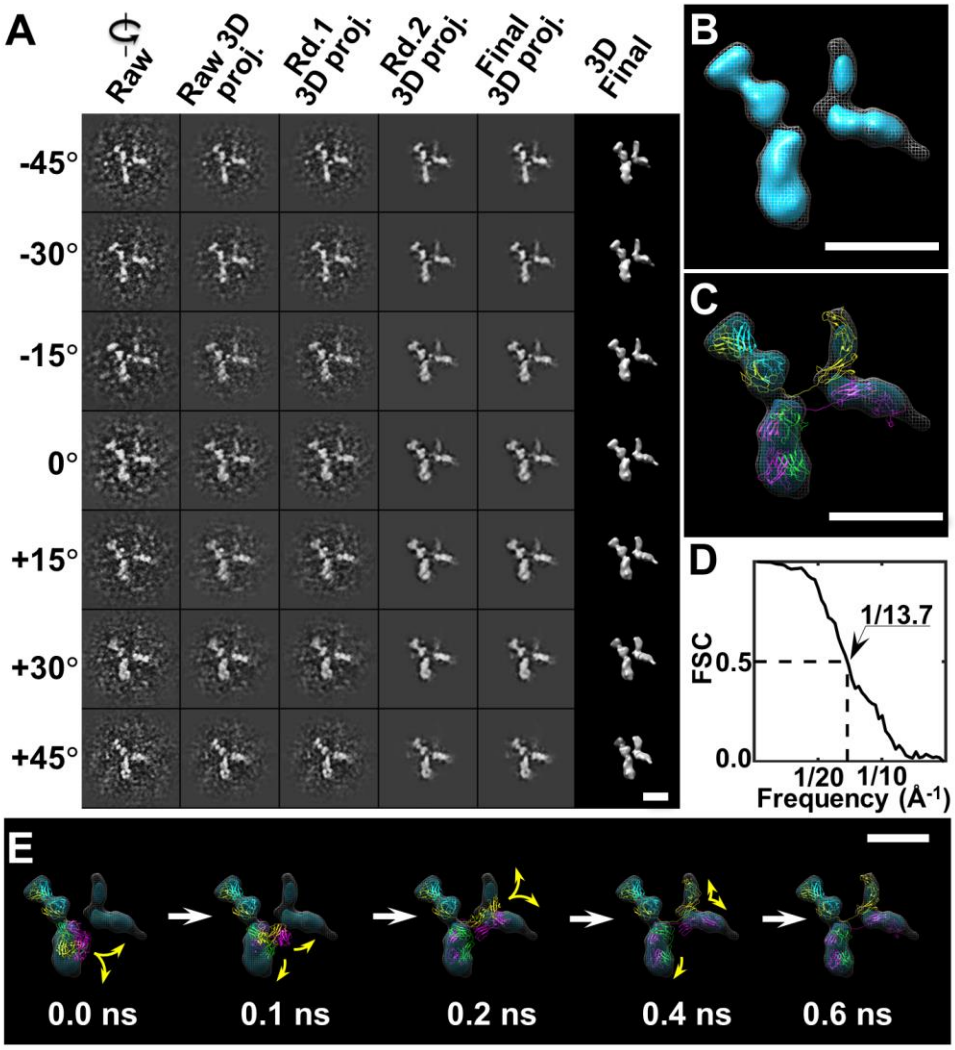

Supplementary Fig. 12 | 3D IPET reconstruction of the first X-shaped IgG homodimer by IPET. (A) Seven representative tilt images of an individual X-shaped particle are displayed in the first column from the left. Using IPET, the tilt images (after CTF correction) were gradually aligned to a common center for 3D reconstruction via iterative refinement. Projections of raw, intermediate and final 3D reconstructions at the corresponding tilt angles are displayed in the next five columns according to their corresponding tilt angles. **(B)** The final 3D density map. **(C)** The density map was flexibly docked with IgG crystal structure by using TMD simulation. **(D)** FSC analyses (from two density maps reconstructed from odd and even numbers of tilt images) showed that the resolution of the final 3D density map was ~13.7 Å. **(E)** Five snapshots illustrated the conformational changes of IgG model during TMD simulation. Scale bars=10 nm.

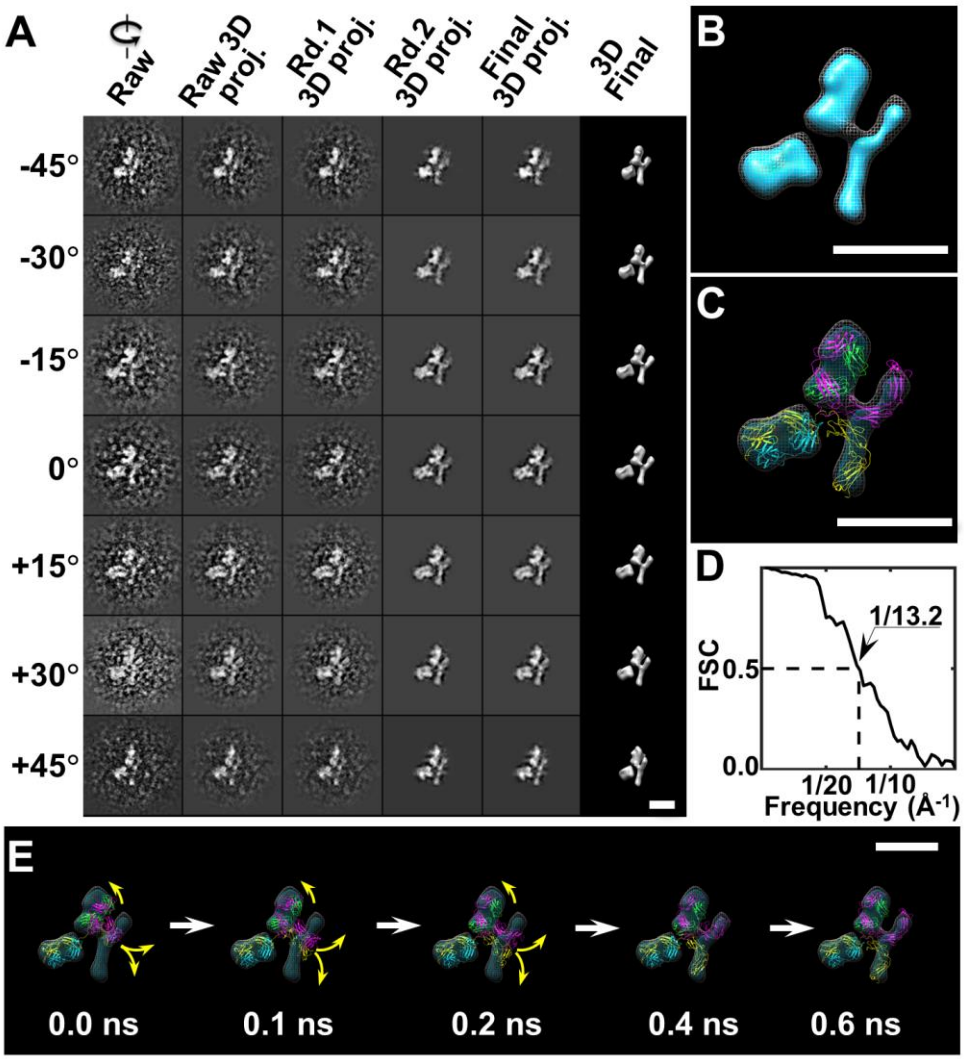

Supplementary Fig. 13 | 3D IPET reconstruction of the second X-shaped IgG homodimer by IPET. **(A)** Seven representative tilt images of an individual X-shaped particle are displayed in the first column from the left. Using IPET, the tilt images (after CTF correction) were gradually aligned to a common center for 3D reconstruction via iterative refinement. Projections of raw, intermediate and final 3D reconstructions at the corresponding tilt angles are displayed in the next five columns according to their corresponding tilt angles. **(B)** The final 3D density map. **(C)** The density map was flexibly docked with IgG crystal structure by using TMD simulation. **(D)** FSC analyses (from two density maps reconstructed from odd and even numbers of tilt images) showed that the resolution of the final 3D density map was ~13.2 Å. **(E)** Five snapshots illustrated the conformational changes of IgG model during TMD simulation. Scale bars=10 nm.

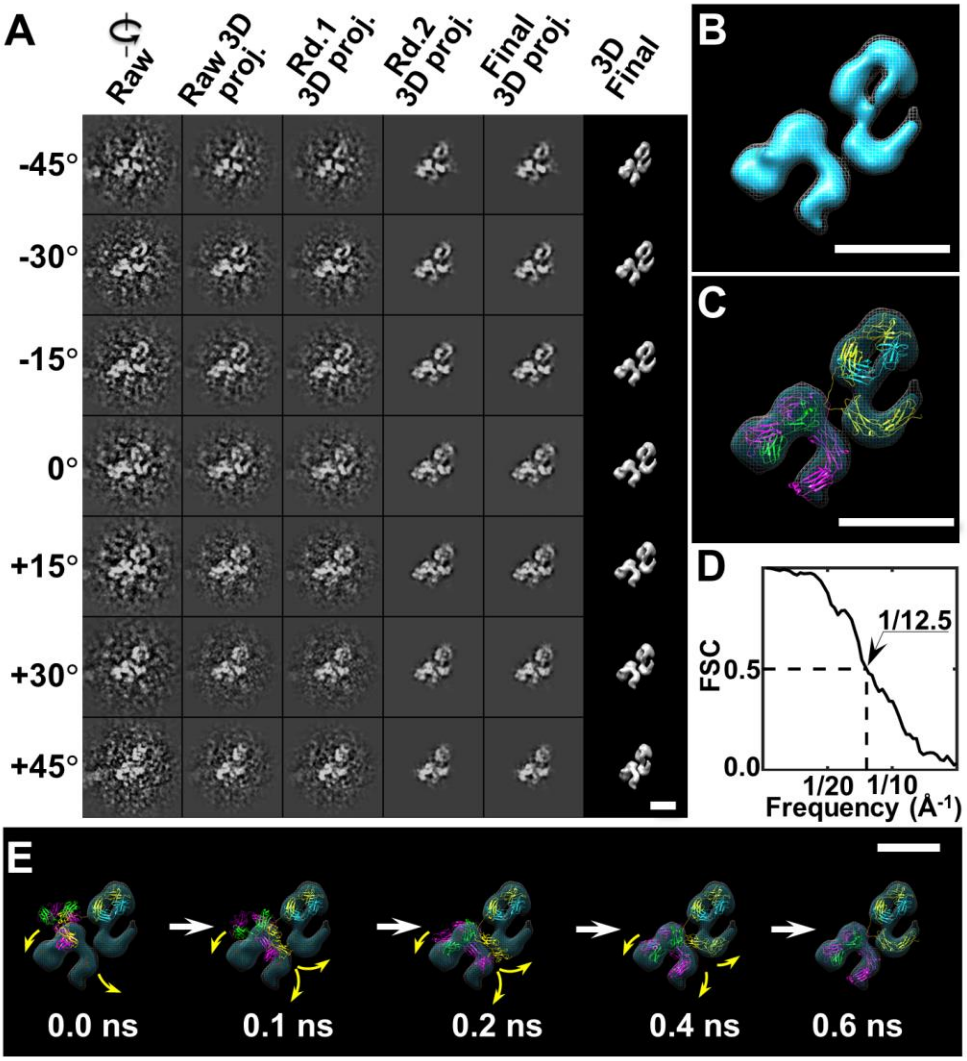

Supplementary Fig. 14 | 3D IPET reconstruction of the third X-shaped IgG homodimer by IPET. (A) Seven representative tilt images of an individual X-shaped particle are displayed in the first column from the left. Using IPET, the tilt images (after CTF correction) were gradually aligned to a common center for 3D reconstruction via iterative refinement. Projections of raw, intermediate and final 3D reconstructions at the corresponding tilt angles are displayed in the next five columns according to their corresponding tilt angles. **(B)** The final 3D density map. **(C)** The density map was flexibly docked with IgG crystal structure by using TMD simulation. **(D)** FSC analyses (from two density maps reconstructed from odd and even numbers of tilt images) showed that the resolution of the final 3D density map was ~12.5 Å. **(E)** Five snapshots illustrated the conformational changes of IgG model during TMD simulation. Scale bars=10 nm.

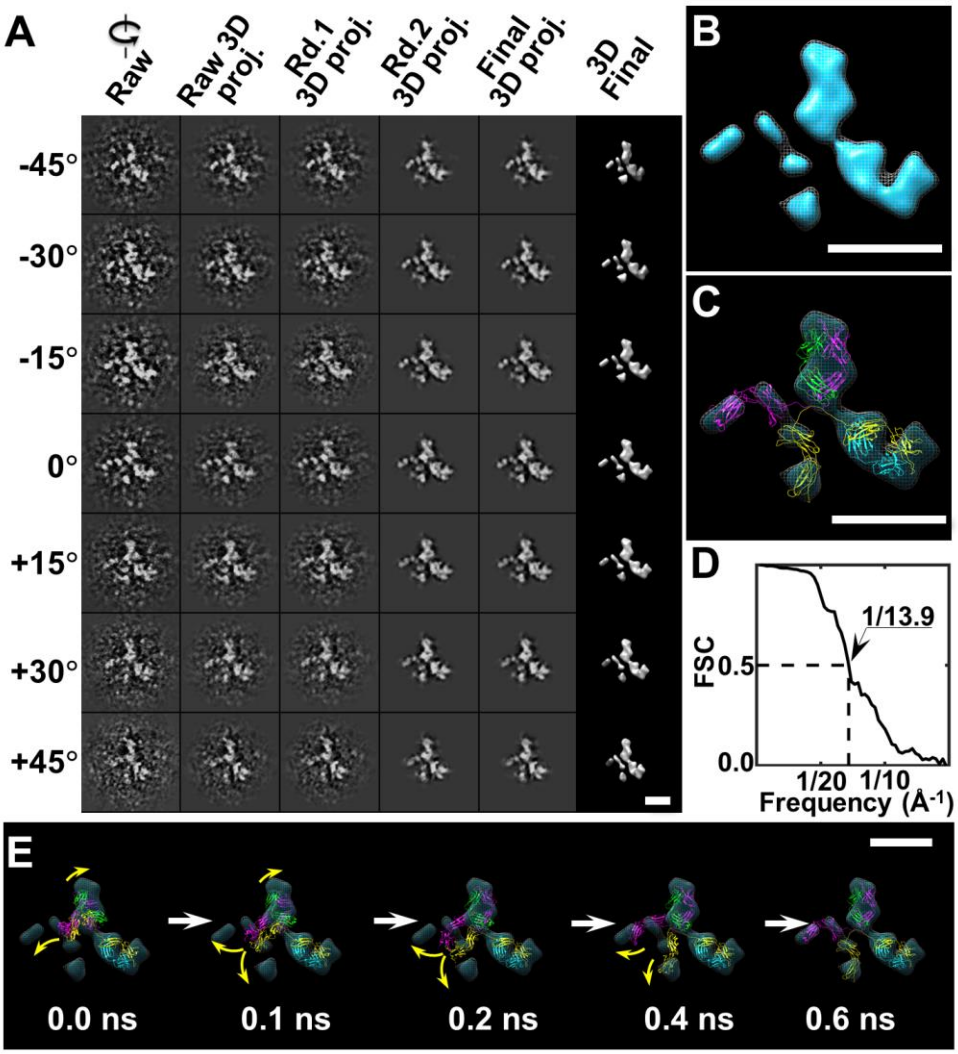

Supplementary Fig. 15 | 3D IPET reconstruction of the forth X-shaped IgG homodimers by IPET. **(A)** Seven representative tilt images of an individual X-shaped particle are displayed in the first column from the left. Using IPET, the tilt images (after CTF correction) were gradually aligned to a common center for 3D reconstruction via iterative refinement. Projections of raw, intermediate and final 3D reconstructions at the corresponding tilt angles are displayed in the next five columns according to their corresponding tilt angles. **(B)** The final 3D density map. **(C)** The density map was flexibly docked with IgG crystal structure by using TMD simulation. **(D)** FSC analyses (from two density maps reconstructed from odd and even numbers of tilt images) showed that the resolution of the final 3D density map was ~13.9 Å. **(E)** Five snapshots illustrated the conformational changes of IgG model during TMD simulation. Scale bars=10 nm.

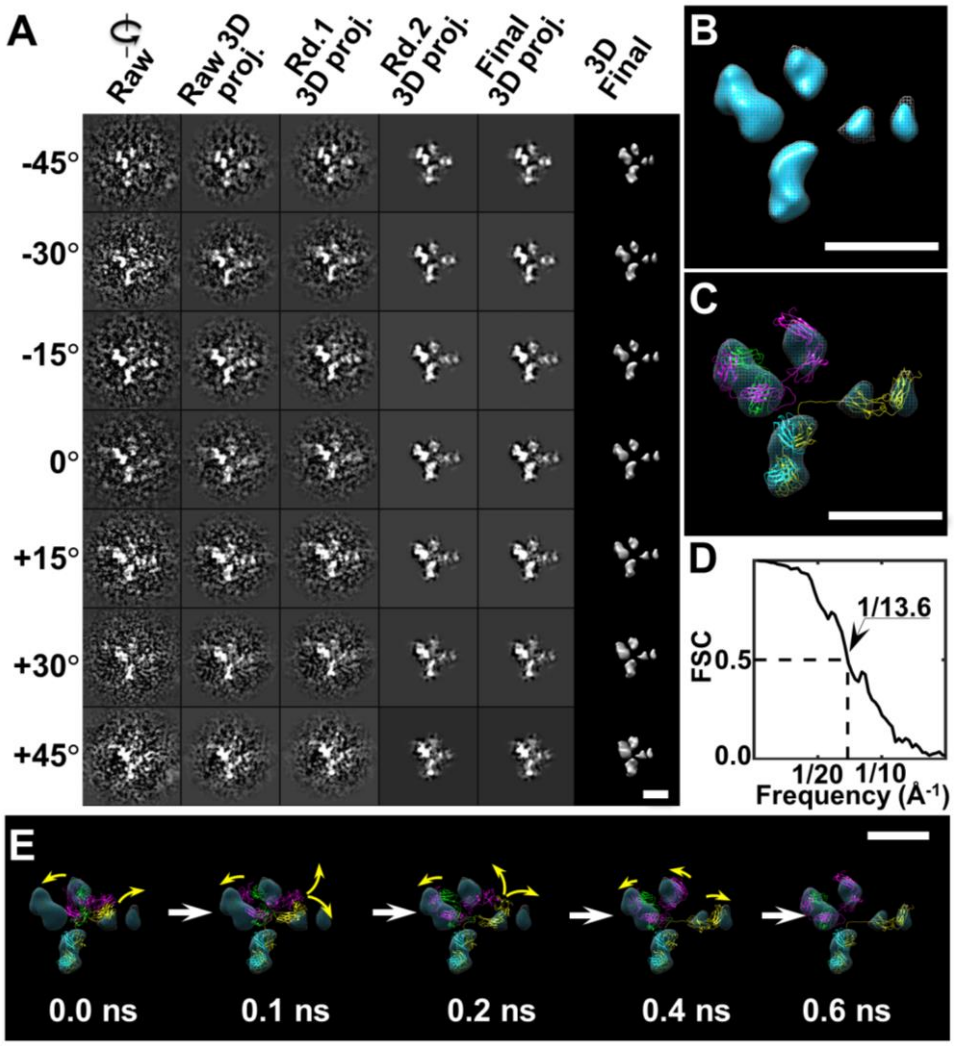

Supplementary Fig. 16 | 3D IPET reconstruction of the fifth X-shaped IgG homodimer by IPET. (A) Seven representative tilt images of an individual X-shaped particle are displayed in the first column from the left. Using IPET, the tilt images (after CTF correction) were gradually aligned to a common center for 3D reconstruction via iterative refinement. Projections of raw, intermediate and final 3D reconstructions at the corresponding tilt angles are displayed in the next five columns according to their corresponding tilt angles. **(B)** The final 3D density map. **(C)** The density map was flexibly docked with IgG crystal structure by using TMD simulation. **(D)** FSC analyses (from two density maps reconstructed from odd and even numbers of tilt images) showed that the resolution of the final 3D density map was ~13.6 Å. **(E)** Five snapshots illustrated the conformational changes of IgG model during TMD simulation. Scale bars=10 nm.

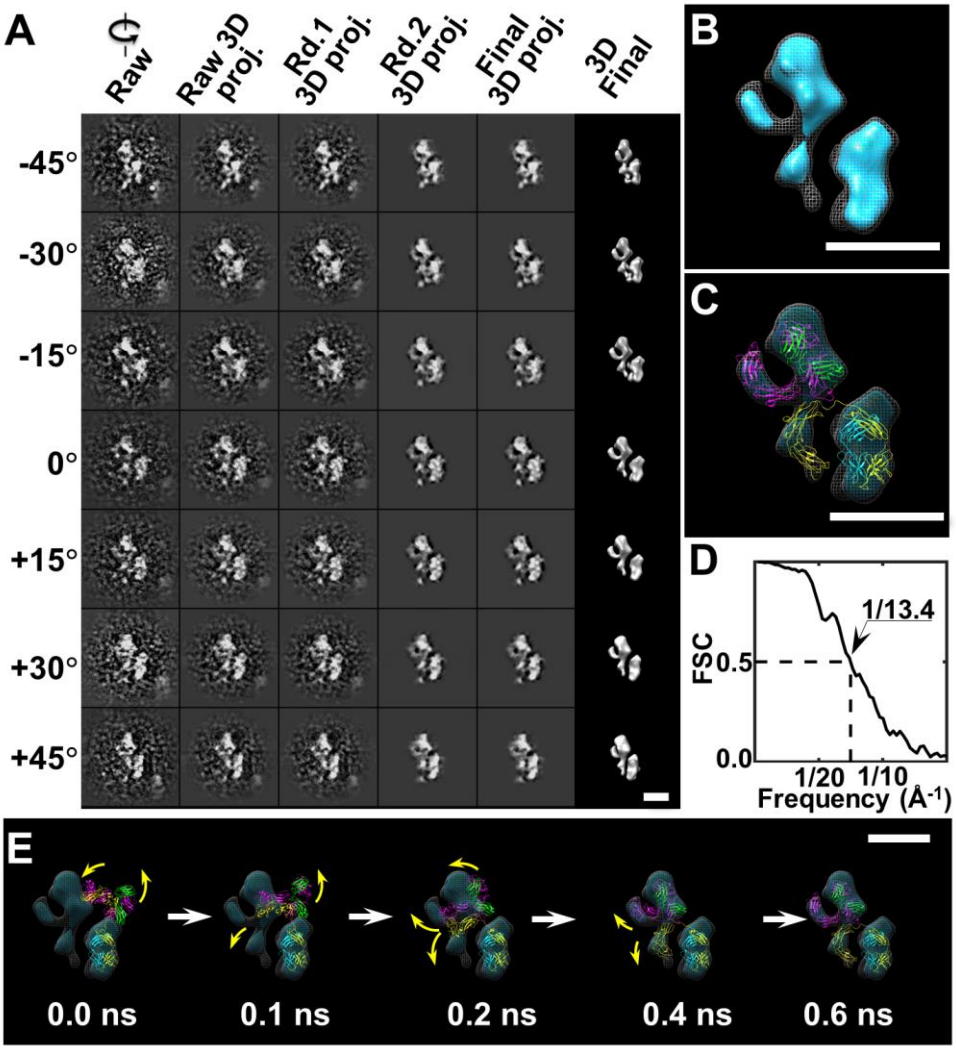

Supplementary Fig. 17 | 3D IPET reconstruction of the sixth X-shaped IgG homodimer by IPET. (A) Seven representative tilt images of an individual X-shaped particle are displayed in the first column from the left. Using IPET, the tilt images (after CTF correction) were gradually aligned to a common center for 3D reconstruction via iterative refinement. Projections of raw, intermediate and final 3D reconstructions at the corresponding tilt angles are displayed in the next five columns according to their corresponding tilt angles. **(B)** The final 3D density map. **(C)** The density map was flexibly docked with IgG crystal structure by using TMD simulation. **(D)** FSC analyses (from two density maps reconstructed from odd and even numbers of tilt images) showed that the resolution of the final 3D density map was ~13.4 Å. **(E)** Five snapshots illustrated the conformational changes of IgG model during TMD simulation. Scale bars=10 nm.

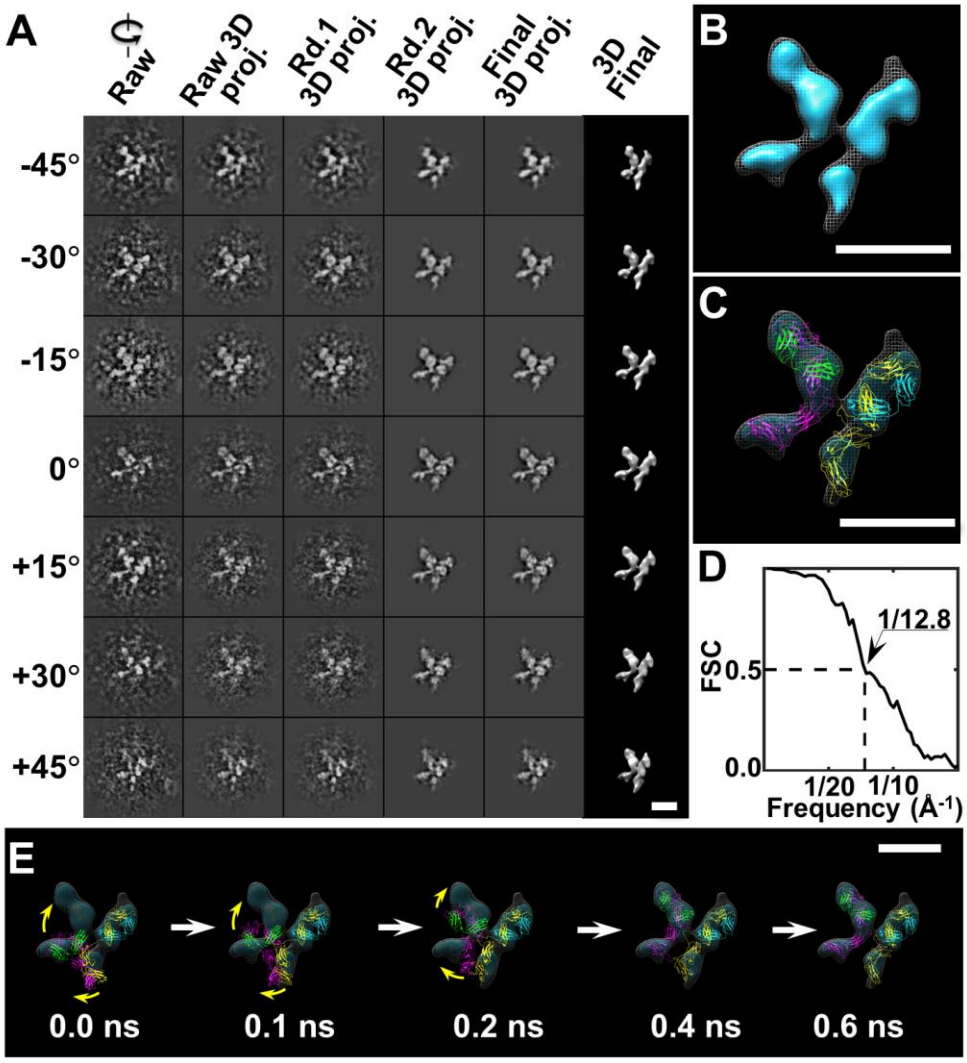

Supplementary Fig. 18 | 3D IPET reconstruction of the seventh X-shaped IgG homodimer by IPET. **(A)** Seven representative tilt images of an individual X-shaped particle are displayed in the first column from the left. Using IPET, the tilt images (after CTF correction) were gradually aligned to a common center for 3D reconstruction via iterative refinement. Projections of raw, intermediate and final 3D reconstructions at the corresponding tilt angles are displayed in the next five columns according to their corresponding tilt angles. **(B)** The final 3D density map. **(C)** The density map was flexibly docked with IgG crystal structure by using TMD simulation. **(D)** FSC analyses (from two density maps reconstructed from odd and even numbers of tilt images) showed that the resolution of the final 3D density map was ~12.8 Å. **(E)** Five snapshots illustrated the conformational changes of IgG model during TMD simulation. Scale bars=10 nm.

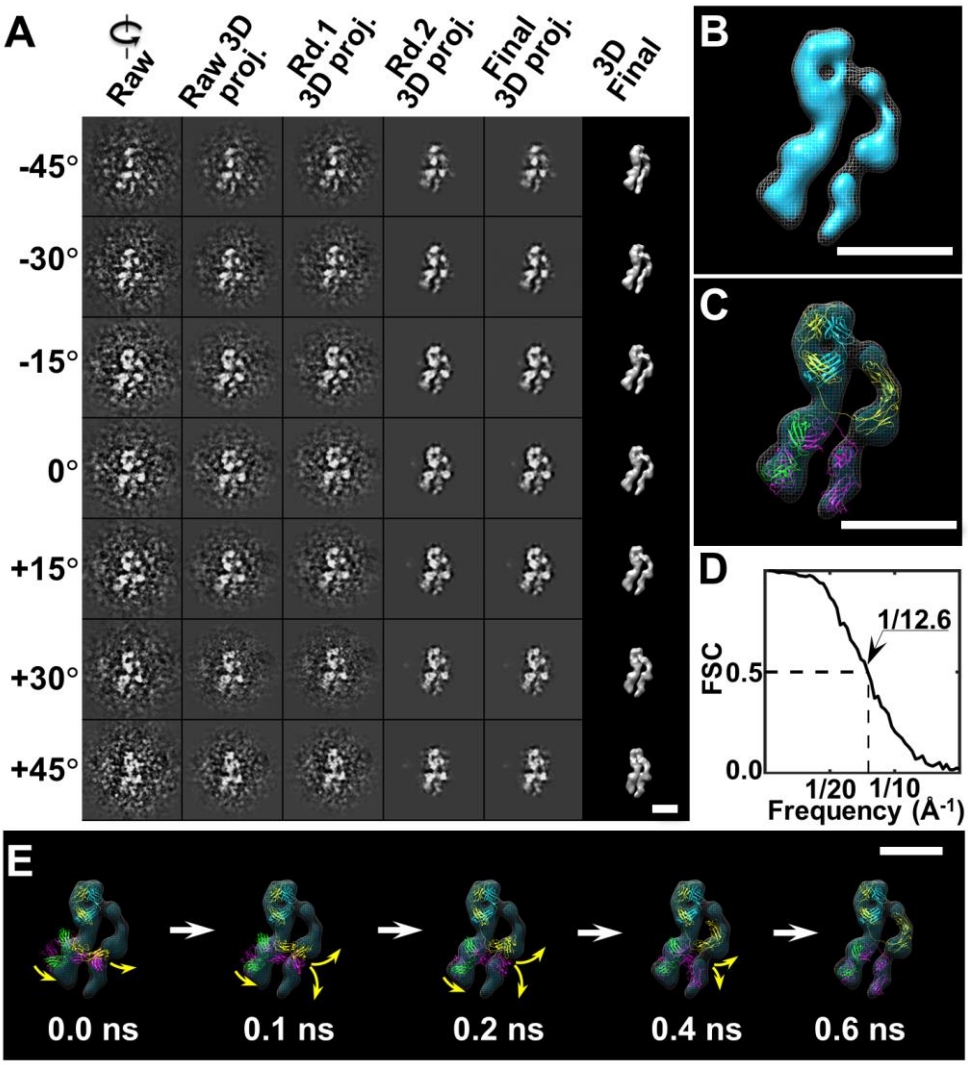

Supplementary Fig. 19 | 3D IPET reconstruction of the eighth X-shaped IgG homodimer by IPET. **(A)** Seven representative tilt images of an individual X-shaped particle are displayed in the first column from the left. Using IPET, the tilt images (after CTF correction) were gradually aligned to a common center for 3D reconstruction via iterative refinement. Projections of raw, intermediate and final 3D reconstructions at the corresponding tilt angles are displayed in the next five columns according to their corresponding tilt angles. **(B)** The final 3D density map. **(C)** The density map was flexibly docked with IgG crystal structure by using TMD simulation. **(D)** FSC analyses (from two density maps reconstructed from odd and even numbers of tilt images) showed that the resolution of the final 3D density map was ~12.6 Å. **(E)** Five snapshots illustrated the conformational changes of IgG model during TMD simulation. Scale bars=10 nm.

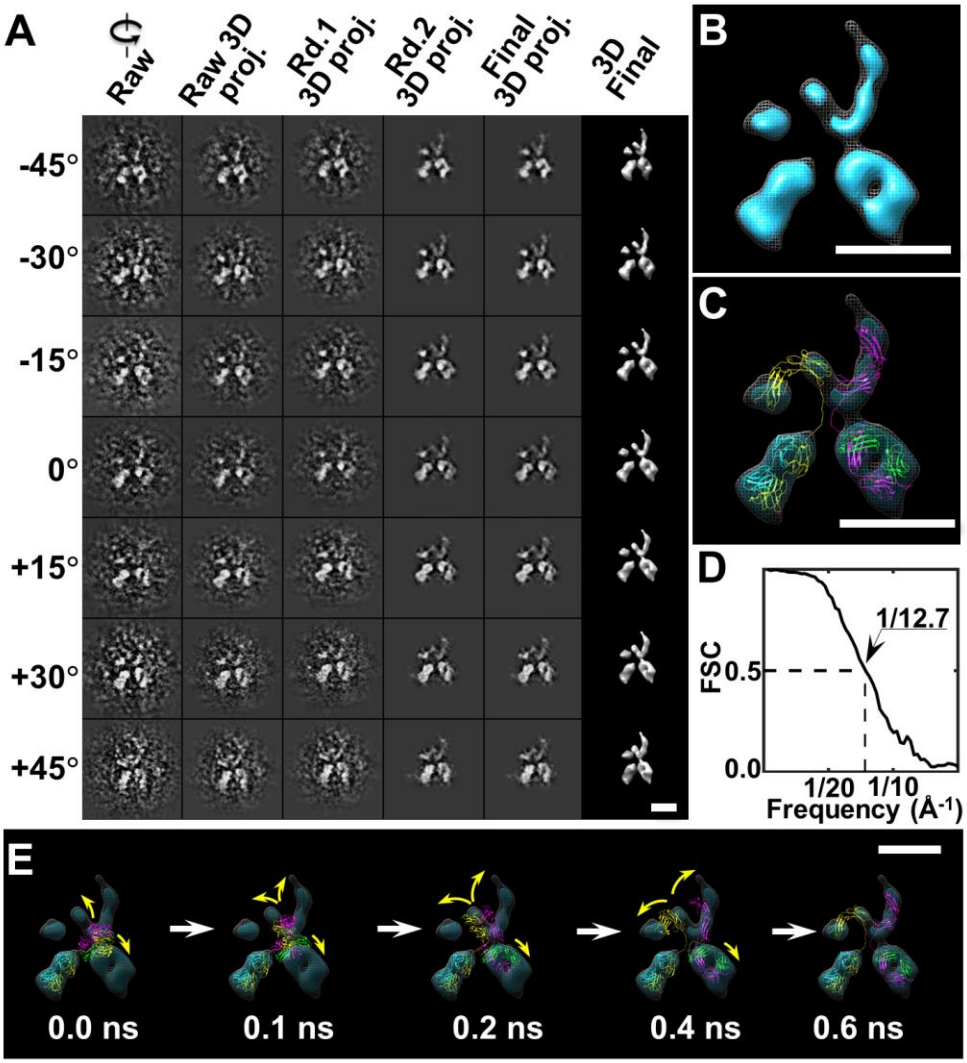

Supplementary Fig. 20 | 3D IPET reconstruction of the ninth X-shaped IgG homodimer by IPET. (A) Seven representative tilt images of an individual X-shaped particle are displayed in the first column from the left. Using IPET, the tilt images (after CTF correction) were gradually aligned to a common center for 3D reconstruction via iterative refinement. Projections of raw, intermediate and final 3D reconstructions at the corresponding tilt angles are displayed in the next five columns according to their corresponding tilt angles. **(B)** The final 3D density map. **(C)** The density map was flexibly docked with IgG crystal structure by using TMD simulation. **(D)** FSC analyses (from two density maps reconstructed from odd and even numbers of tilt images) showed that the resolution of the final 3D density map was ~12.7 Å. **(E)** Five snapshots illustrated the conformational changes of IgG model during TMD simulation. Scale bars=10 nm.

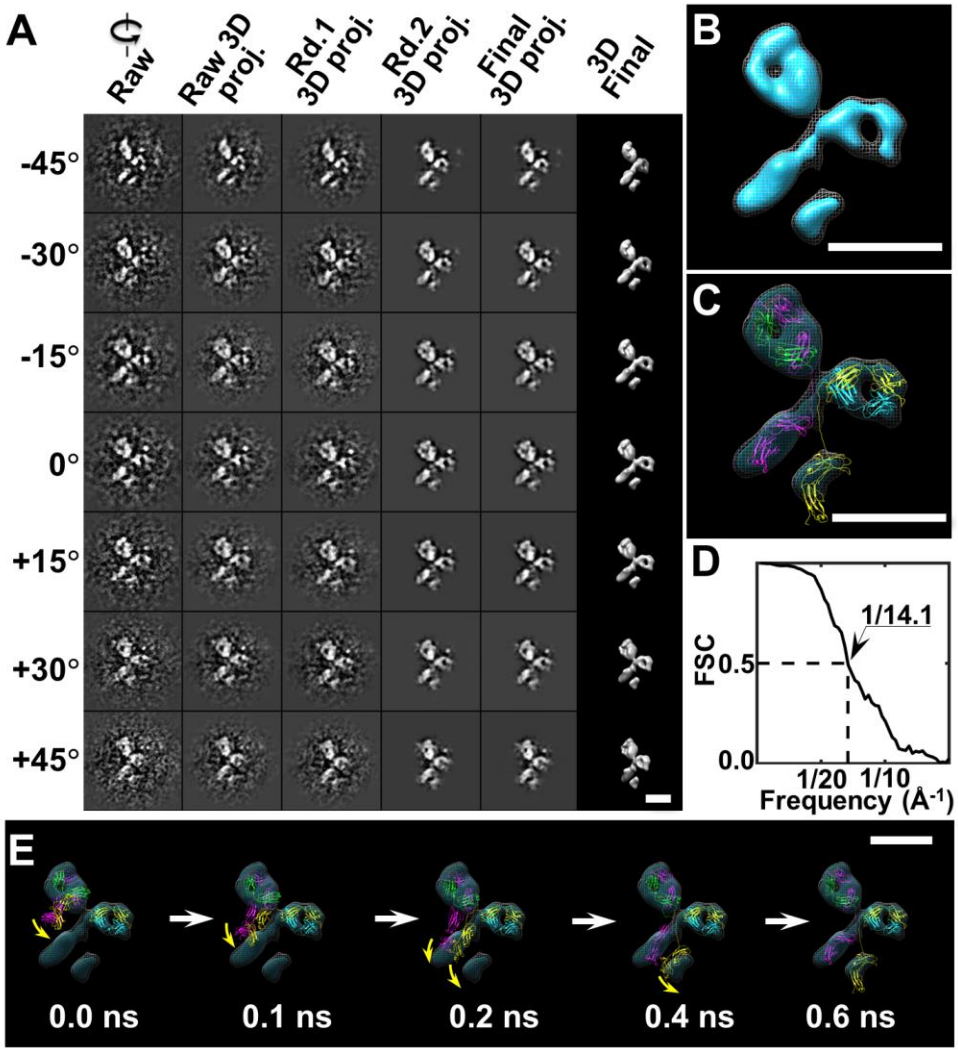

Supplementary Fig. 21 | 3D IPET reconstruction of the tenth X-shaped IgG homodimer by IPET. (A) Seven representative tilt images of an individual X-shaped particle are displayed in the first column from the left. Using IPET, the tilt images (after CTF correction) were gradually aligned to a common center for 3D reconstruction via iterative refinement. Projections of raw, intermediate and final 3D reconstructions at the corresponding tilt angles are displayed in the next five columns according to their corresponding tilt angles. **(B)** The final 3D density map. **(C)** The density map was flexibly docked with IgG crystal structure by using TMD simulation. **(D)** FSC analyses (from two density maps reconstructed from odd and even numbers of tilt images) showed that the resolution of the final 3D density map was ~14.1 Å. **(E)** Five snapshots illustrated the conformational changes of IgG model during TMD simulation. Scale bars=10 nm.

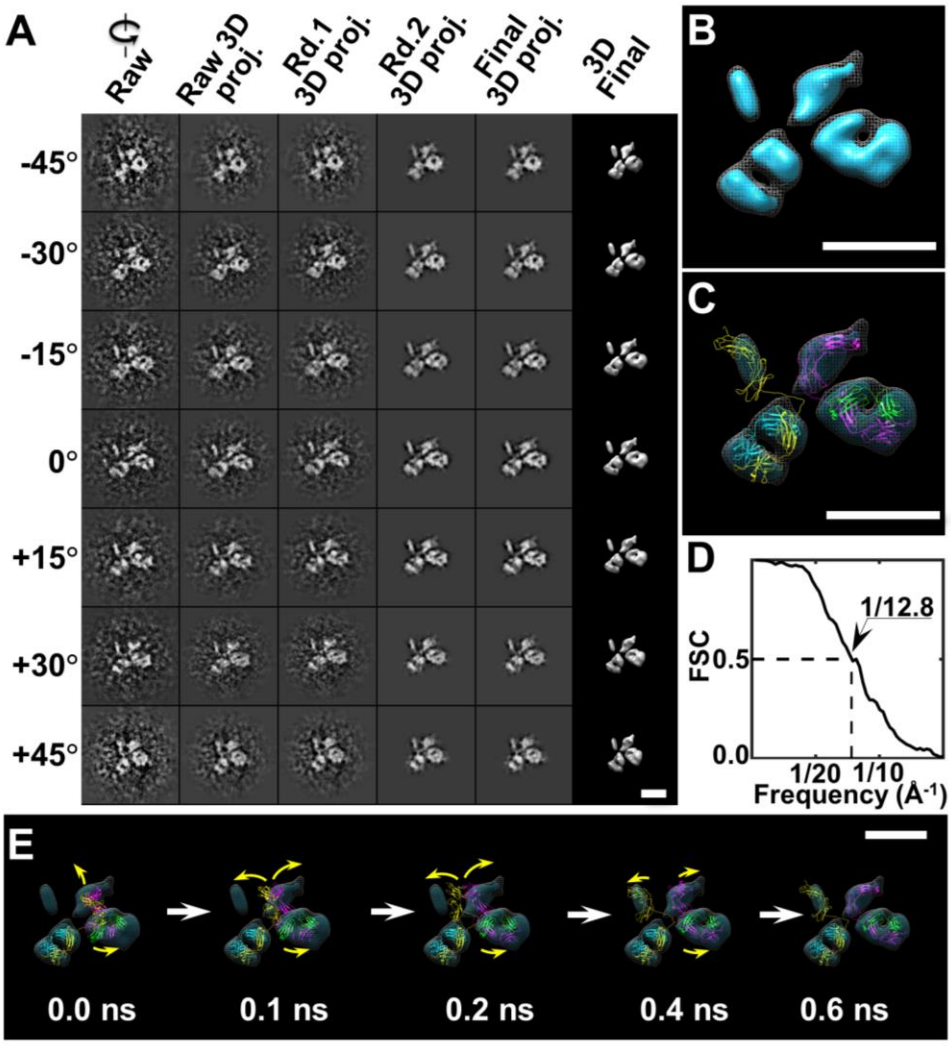

Supplementary Fig. 22 | 3D IPET reconstruction of the 11th X-shaped IgG homodimer by IPET. (A) Seven representative tilt images of an individual X-shaped particle are displayed in the first column from the left. Using IPET, the tilt images (after CTF correction) were gradually aligned to a common center for 3D reconstruction via iterative refinement. Projections of raw, intermediate and final 3D reconstructions at the corresponding tilt angles are displayed in the next five columns according to their corresponding tilt angles. **(B)** The final 3D density map. **(C)** The density map was flexibly docked with IgG crystal structure by using TMD simulation. **(D)** FSC analyses (from two density maps reconstructed from odd and even numbers of tilt images) showed that the resolution of the final 3D density map was ~12.8 Å. **(E)** Five snapshots illustrated the conformational changes of IgG model during TMD simulation. Scale bars=10 nm.

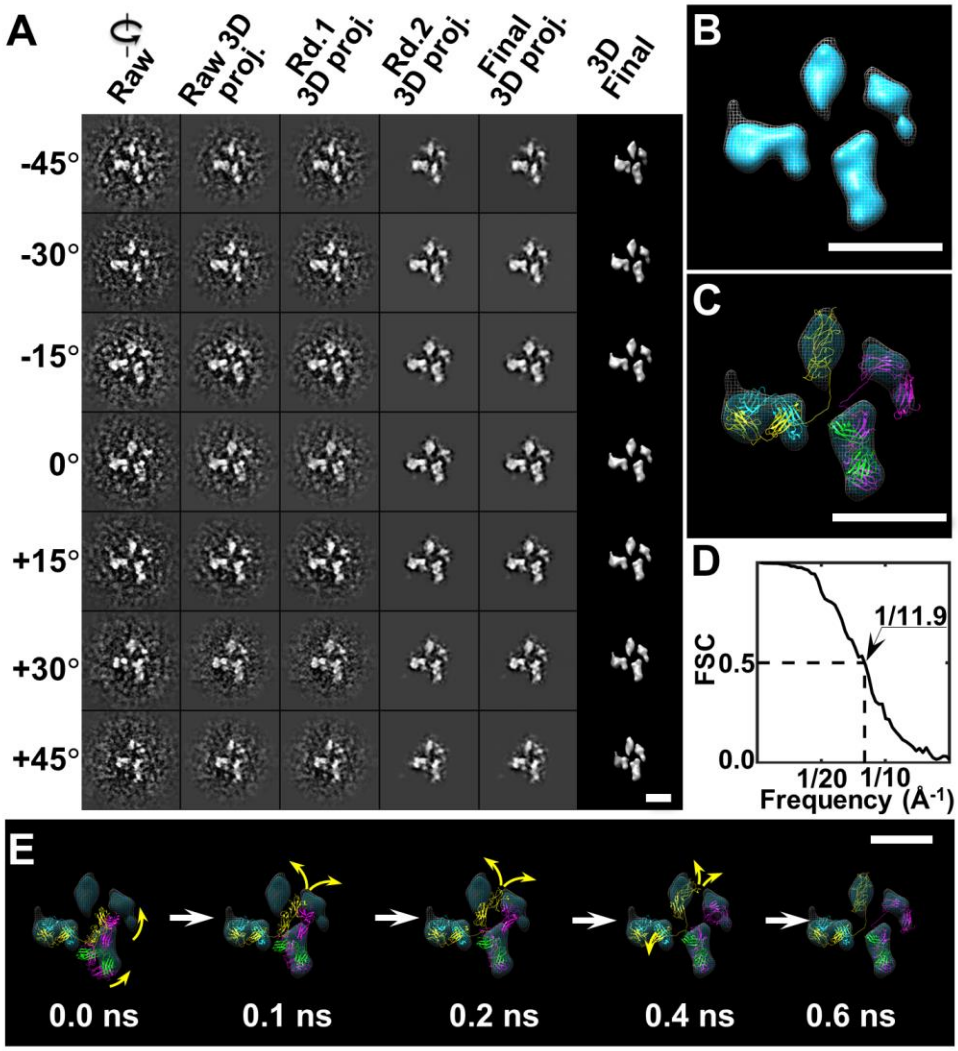

Supplementary Fig. 23 | 3D IPET reconstruction of the 12th X-shaped IgG homodimer by IPET. (A) Seven representative tilt images of an individual X-shaped particle are displayed in the first column from the left. Using IPET, the tilt images (after CTF correction) were gradually aligned to a common center for 3D reconstruction via iterative refinement. Projections of raw, intermediate and final 3D reconstructions at the corresponding tilt angles are displayed in the next five columns according to their corresponding tilt angles. **(B)** The final 3D density map. **(C)** The density map was flexibly docked with IgG crystal structure by using TMD simulation. **(D)** FSC analyses (from two density maps reconstructed from odd and even numbers of tilt images) showed that the resolution of the final 3D density map was ~11.9 Å. **(E)** Five snapshots illustrated the conformational changes of IgG model during TMD simulation. Scale bars=10 nm.

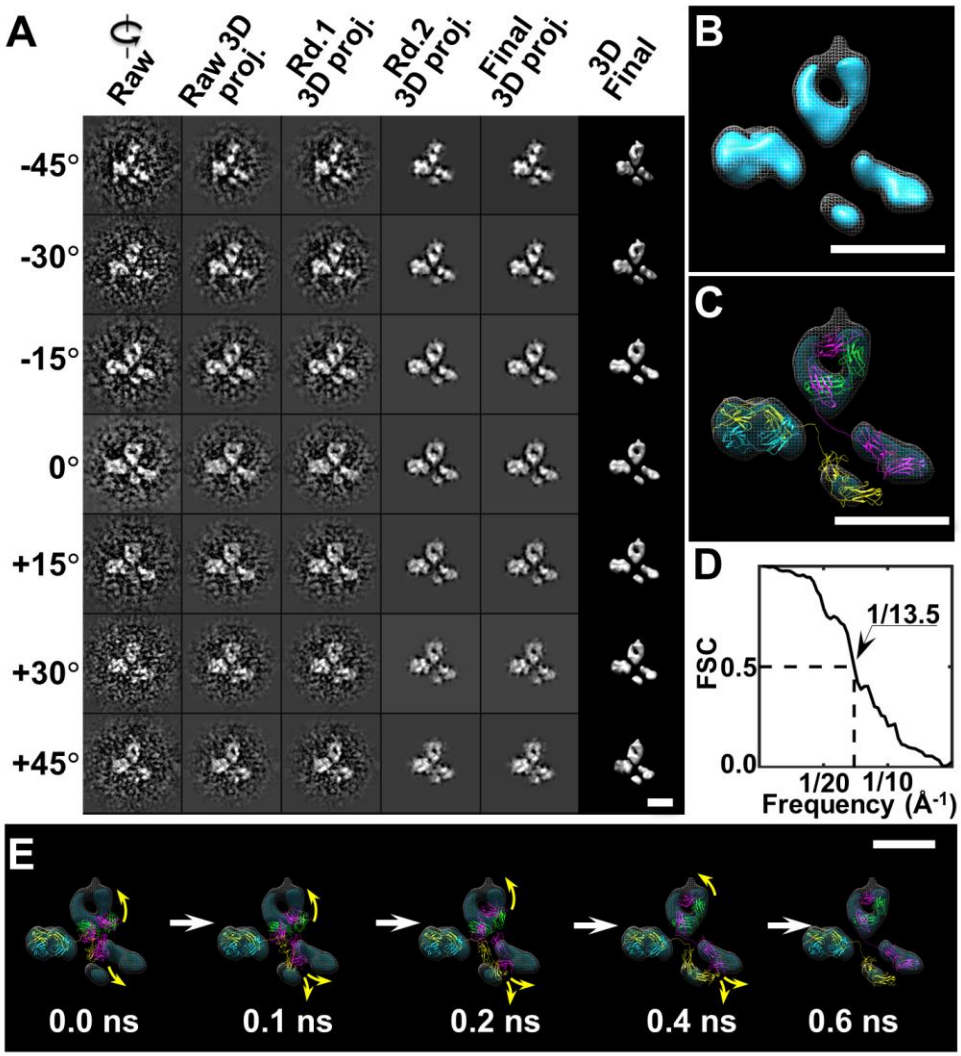

Supplementary Fig. 24 | 3D IPET reconstruction of the 13th X-shaped IgG homodimer by IPET. (A) Seven representative tilt images of an individual X-shaped particle are displayed in the first column from the left. Using IPET, the tilt images (after CTF correction) were gradually aligned to a common center for 3D reconstruction via iterative refinement. Projections of raw, intermediate and final 3D reconstructions at the corresponding tilt angles are displayed in the next five columns according to their corresponding tilt angles. **(B)** The final 3D density map. **(C)** The density map was flexibly docked with IgG crystal structure by using TMD simulation. **(D)** FSC analyses (from two density maps reconstructed from odd and even numbers of tilt images) showed that the resolution of the final 3D density map was ~13.5 Å. **(E)** Five snapshots illustrated the conformational changes of IgG model during TMD simulation. Scale bars=10 nm.

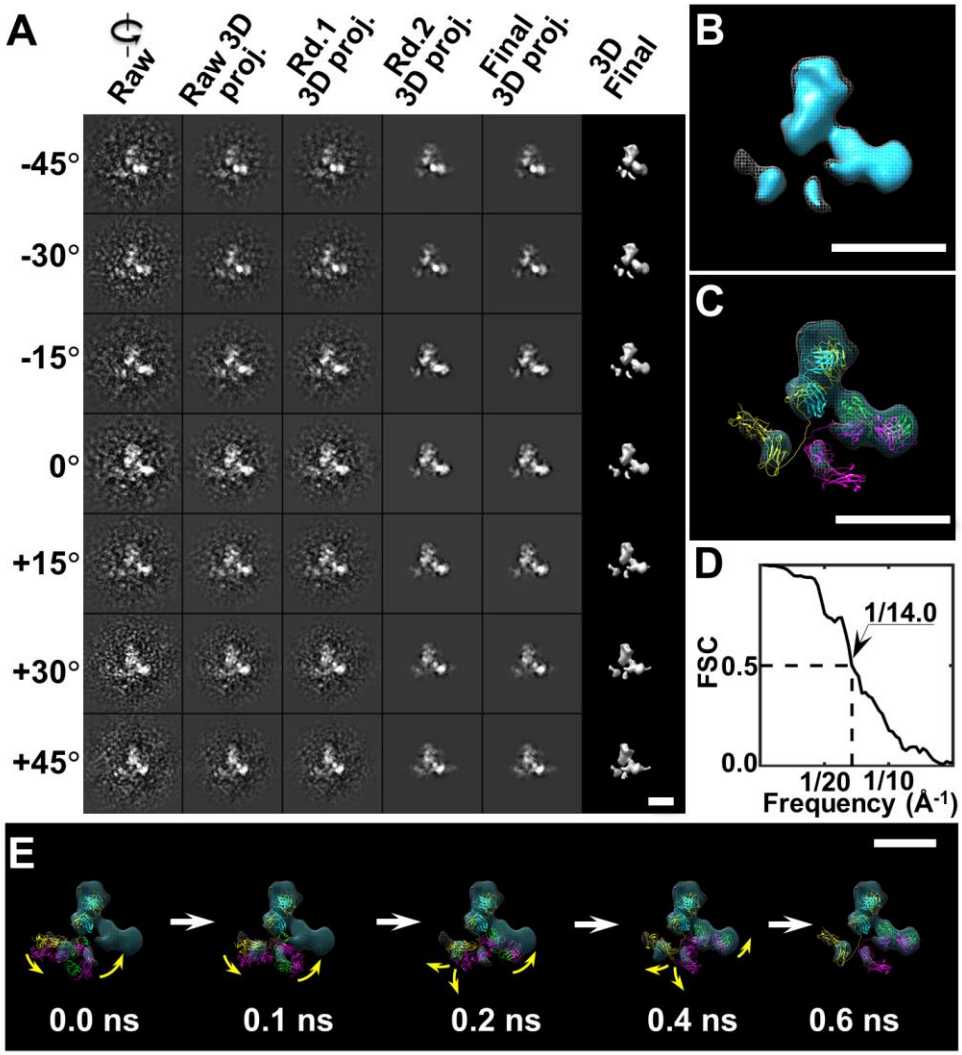

Supplementary Fig. 25 | 3D IPET reconstruction of the 14th X-shaped IgG homodimer by IPET. (A) Seven representative tilt images of an individual X-shaped particle are displayed in the first column from the left. Using IPET, the tilt images (after CTF correction) were gradually aligned to a common center for 3D reconstruction via iterative refinement. Projections of raw, intermediate and final 3D reconstructions at the corresponding tilt angles are displayed in the next five columns according to their corresponding tilt angles. **(B)** The final 3D density map. **(C)** The density map was flexibly docked with IgG crystal structure by using TMD simulation. **(D)** FSC analyses (from two density maps reconstructed from odd and even numbers of tilt images) showed that the resolution of the final 3D density map was ~14.0 Å. **(E)** Five snapshots illustrated the conformational changes of IgG model during TMD simulation. Scale bars=10 nm.

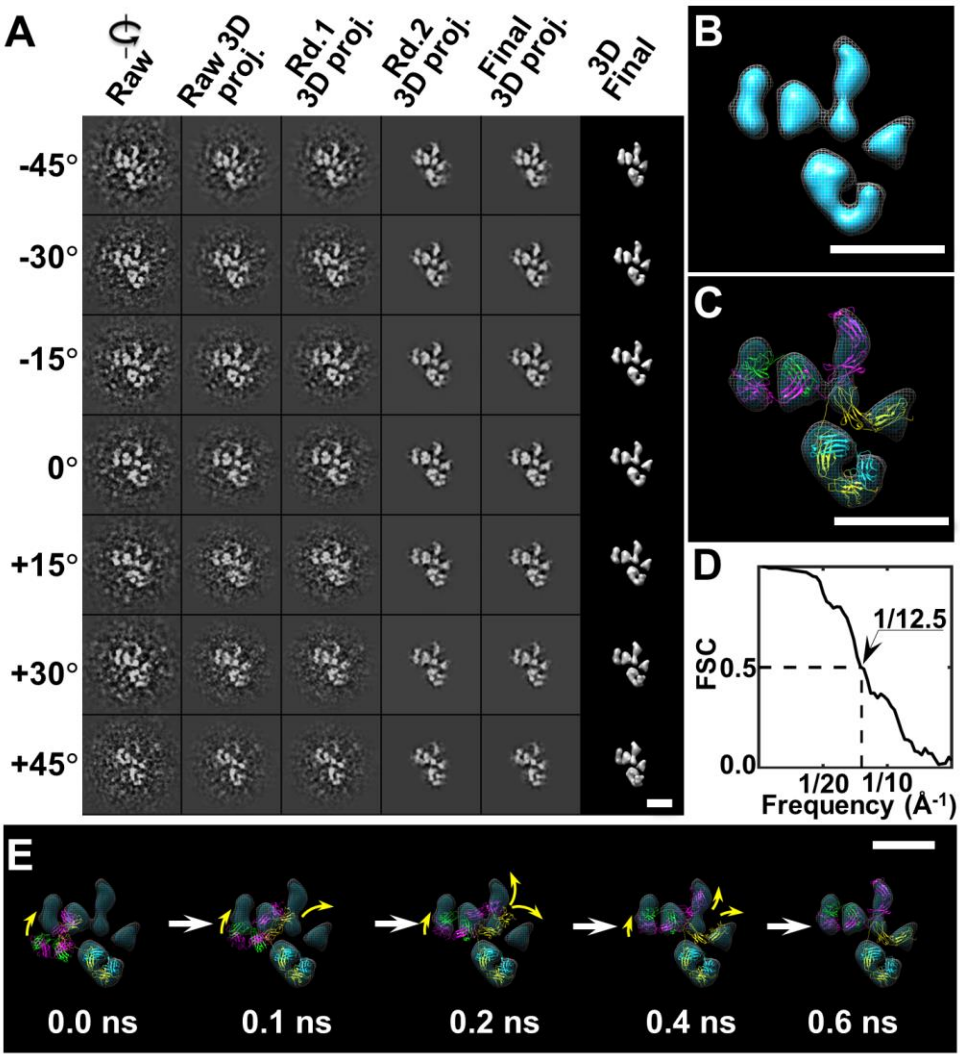

Supplementary Fig. 26 | 3D IPET reconstruction of the 15th X-shaped IgG homodimer by IPET. (A) Seven representative tilt images of an individual X-shaped particle are displayed in the first column from the left. Using IPET, the tilt images (after CTF correction) were gradually aligned to a common center for 3D reconstruction via iterative refinement. Projections of raw, intermediate and final 3D reconstructions at the corresponding tilt angles are displayed in the next five columns according to their corresponding tilt angles. **(B)** The final 3D density map. **(C)** The density map was flexibly docked with IgG crystal structure by using TMD simulation. **(D)** FSC analyses (from two density maps reconstructed from odd and even numbers of tilt images) showed that the resolution of the final 3D density map was ~12.5 Å. **(E)** Five snapshots illustrated the conformational changes of IgG model during TMD simulation. Scale bars=10 nm.

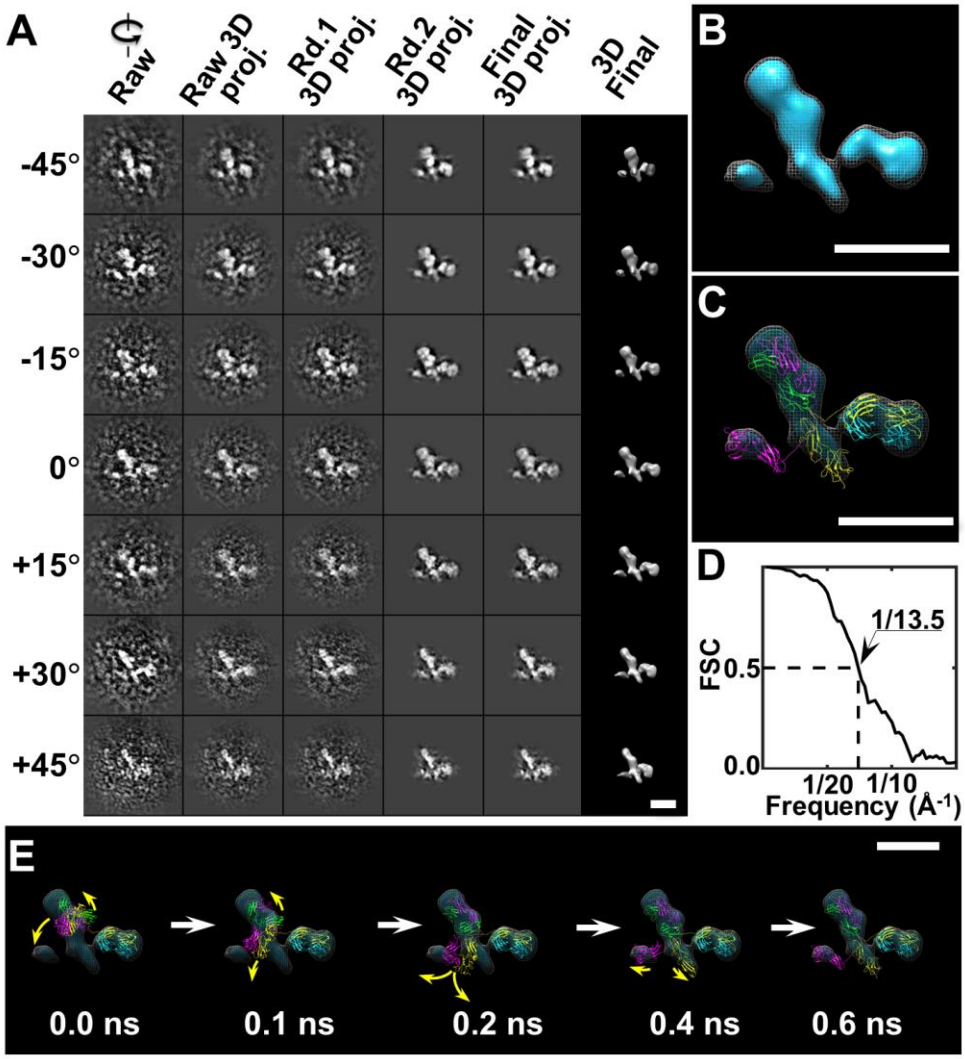

Supplementary Fig. 27 | 3D IPET reconstruction of the 16th X-shaped IgG homodimer by IPET. (A) Seven representative tilt images of an individual X-shaped particle are displayed in the first column from the left. Using IPET, the tilt images (after CTF correction) were gradually aligned to a common center for 3D reconstruction via iterative refinement. Projections of raw, intermediate and final 3D reconstructions at the corresponding tilt angles are displayed in the next five columns according to their corresponding tilt angles. **(B)** The final 3D density map. **(C)** The density map was flexibly docked with IgG crystal structure by using TMD simulation. **(D)** FSC analyses (from two density maps reconstructed from odd and even numbers of tilt images) showed that the resolution of the final 3D density map was ~13.5 Å. **(E)** Five snapshots illustrated the conformational changes of IgG model during TMD simulation. Scale bars=10 nm.

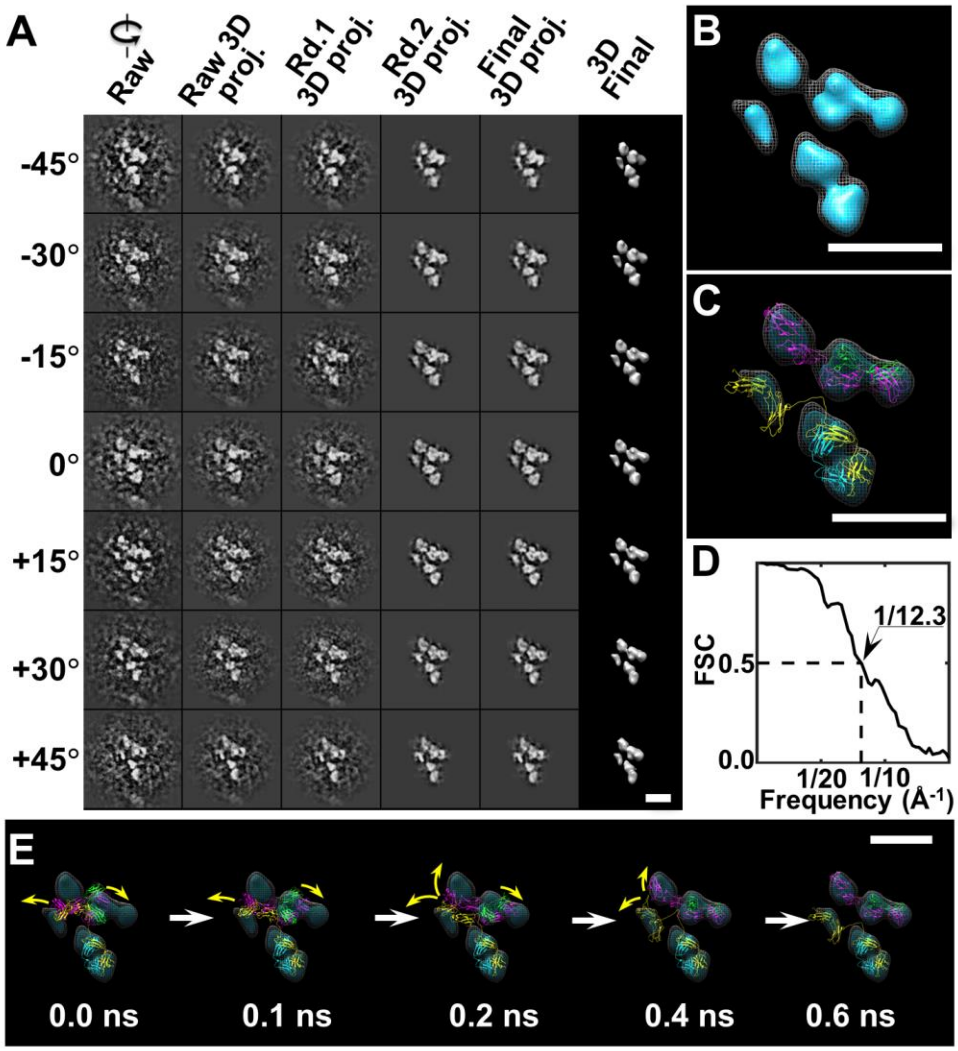

Supplementary Fig. 28 | 3D IPET reconstruction of the 17th X-shaped IgG homodimer by IPET. (A) Seven representative tilt images of an individual X-shaped particle are displayed in the first column from the left. Using IPET, the tilt images (after CTF correction) were gradually aligned to a common center for 3D reconstruction via iterative refinement. Projections of raw, intermediate and final 3D reconstructions at the corresponding tilt angles are displayed in the next five columns according to their corresponding tilt angles. **(B)** The final 3D density map. **(C)** The density map was flexibly docked with IgG crystal structure by using TMD simulation. **(D)** FSC analyses (from two density maps reconstructed from odd and even numbers of tilt images) showed that the resolution of the final 3D density map was ~12.3 Å. **(E)** Five snapshots illustrated the conformational changes of IgG model during TMD simulation. Scale bars=10 nm.

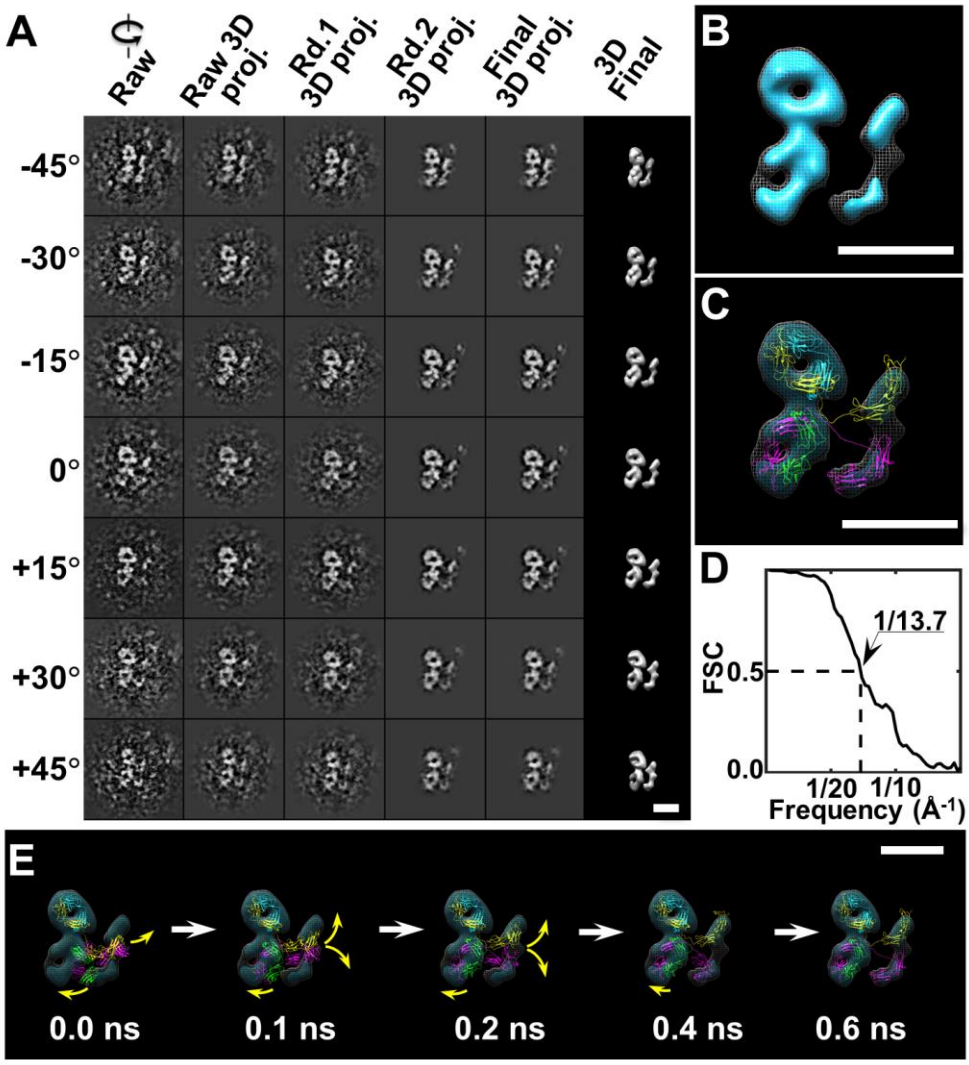

Supplementary Fig. 29 | 3D IPET reconstruction of the 18th X-shaped IgG homodimer by IPET. (A) Seven representative tilt images of an individual X-shaped particle are displayed in the first column from the left. Using IPET, the tilt images (after CTF correction) were gradually aligned to a common center for 3D reconstruction via iterative refinement. Projections of raw, intermediate and final 3D reconstructions at the corresponding tilt angles are displayed in the next five columns according to their corresponding tilt angles. **(B)** The final 3D density map. **(C)** The density map was flexibly docked with IgG crystal structure by using TMD simulation. **(D)** FSC analyses (from two density maps reconstructed from odd and even numbers of tilt images) showed that the resolution of the final 3D density map was ~13.7 Å. **(E)** Five snapshots illustrated the conformational changes of IgG model during TMD simulation. Scale bars=10 nm.

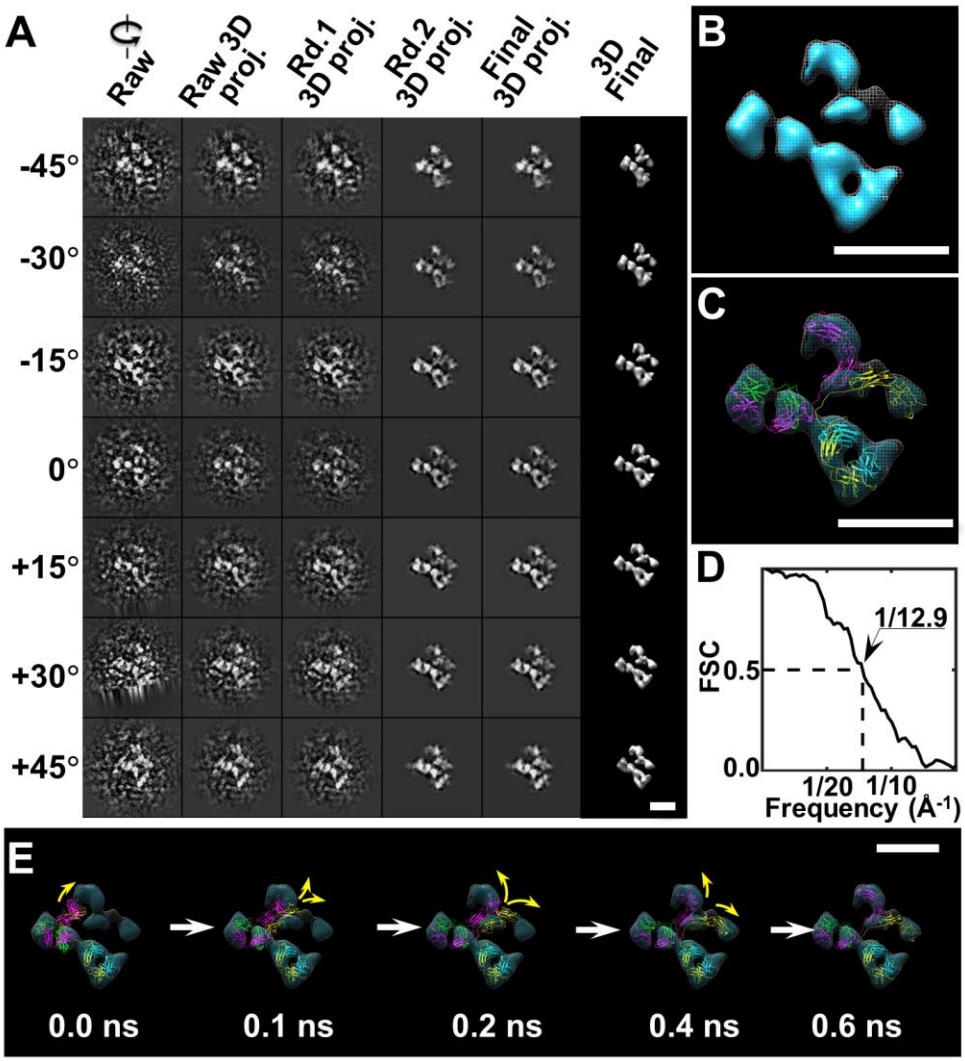

Supplementary Fig. 30 | 3D IPET reconstruction of the 19th X-shaped IgG homodimer by IPET. (A) Seven representative tilt images of an individual X-shaped particle are displayed in the first column from the left. Using IPET, the tilt images (after CTF correction) were gradually aligned to a common center for 3D reconstruction via iterative refinement. Projections of raw, intermediate and final 3D reconstructions at the corresponding tilt angles are displayed in the next five columns according to their corresponding tilt angles. **(B)** The final 3D density map. **(C)** The density map was flexibly docked with IgG crystal structure by using TMD simulation. **(D)** FSC analyses (from two density maps reconstructed from odd and even numbers of tilt images) showed that the resolution of the final 3D density map was ~12.9 Å. **(E)** Five snapshots illustrated the conformational changes of IgG model during TMD simulation. Scale bars=10 nm.

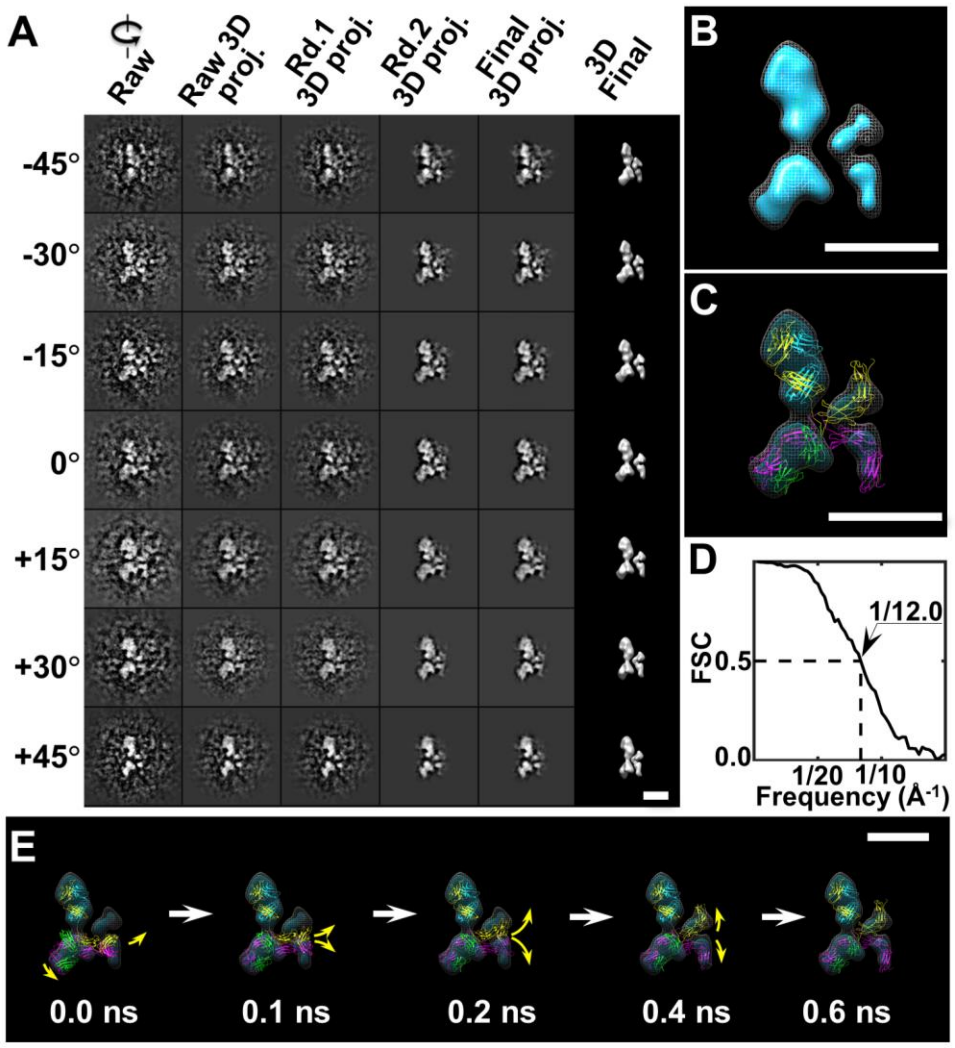

Supplementary Fig. 31 | 3D IPET reconstruction of the 20th X-shaped IgG homodimer by IPET. (A) Seven representative tilt images of an individual X-shaped particle are displayed in the first column from the left. Using IPET, the tilt images (after CTF correction) were gradually aligned to a common center for 3D reconstruction via iterative refinement. Projections of raw, intermediate and final 3D reconstructions at the corresponding tilt angles are displayed in the next five columns according to their corresponding tilt angles. **(B)** The final 3D density map. **(C)** The density map was flexibly docked with IgG crystal structure by using TMD simulation. **(D)** FSC analyses (from two density maps reconstructed from odd and even numbers of tilt images) showed that the resolution of the final 3D density map was ~12.0 Å. **(E)** Five snapshots illustrated the conformational changes of IgG model during TMD simulation. Scale bars=10 nm.

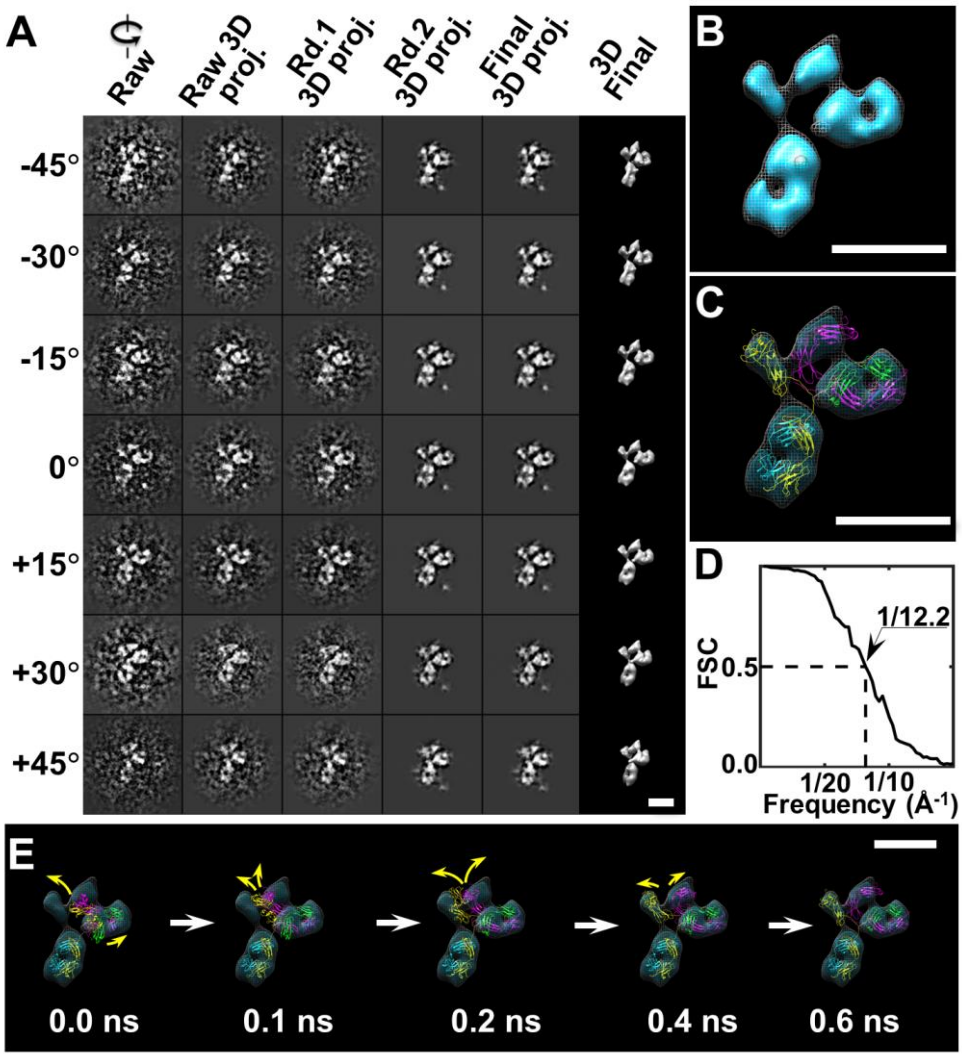

Supplementary Fig. 32 | 3D IPET reconstruction of the 21st X-shaped IgG homodimer by IPET. (A) Seven representative tilt images of an individual X-shaped particle are displayed in the first column from the left. Using IPET, the tilt images (after CTF correction) were gradually aligned to a common center for 3D reconstruction via iterative refinement. Projections of raw, intermediate and final 3D reconstructions at the corresponding tilt angles are displayed in the next five columns according to their corresponding tilt angles. **(B)** The final 3D density map. **(C)** The density map was flexibly docked with IgG crystal structure by using TMD simulation. **(D)** FSC analyses (from two density maps reconstructed from odd and even numbers of tilt images) showed that the resolution of the final 3D density map was ~12.2 Å. **(E)** Five snapshots illustrated the conformational changes of IgG model during TMD simulation. Scale bars=10 nm.

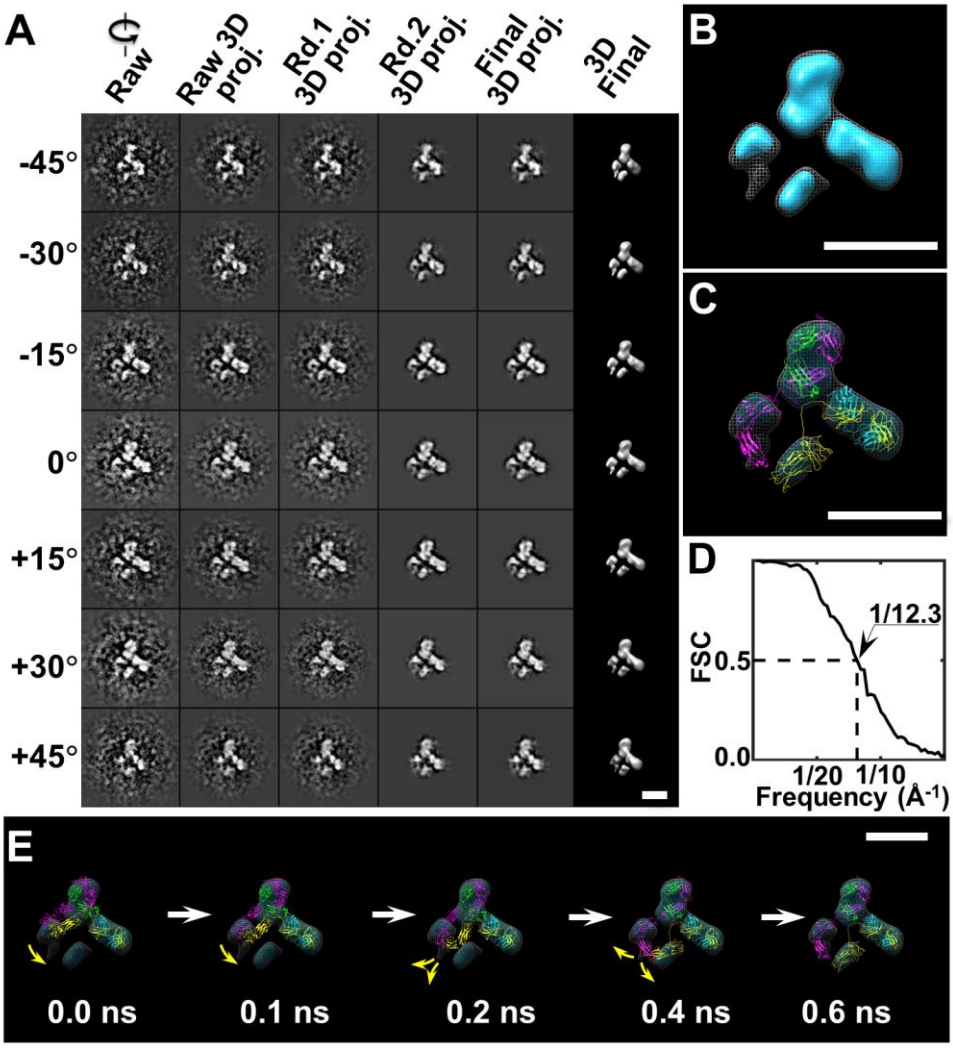

Supplementary Fig. 33 | 3D IPET reconstruction of the 22nd X-shaped IgG homodimer by IPET. (A) Seven representative tilt images of an individual X-shaped particle are displayed in the first column from the left. Using IPET, the tilt images (after CTF correction) were gradually aligned to a common center for 3D reconstruction via iterative refinement. Projections of raw, intermediate and final 3D reconstructions at the corresponding tilt angles are displayed in the next five columns according to their corresponding tilt angles. **(B)** The final 3D density map. **(C)** The density map was flexibly docked with IgG crystal structure by using TMD simulation. **(D)** FSC analyses (from two density maps reconstructed from odd and even numbers of tilt images) showed that the resolution of the final 3D density map was ~13.3 Å. **(E)** Five snapshots illustrated the conformational changes of IgG model during TMD simulation. Scale bars=10 nm.

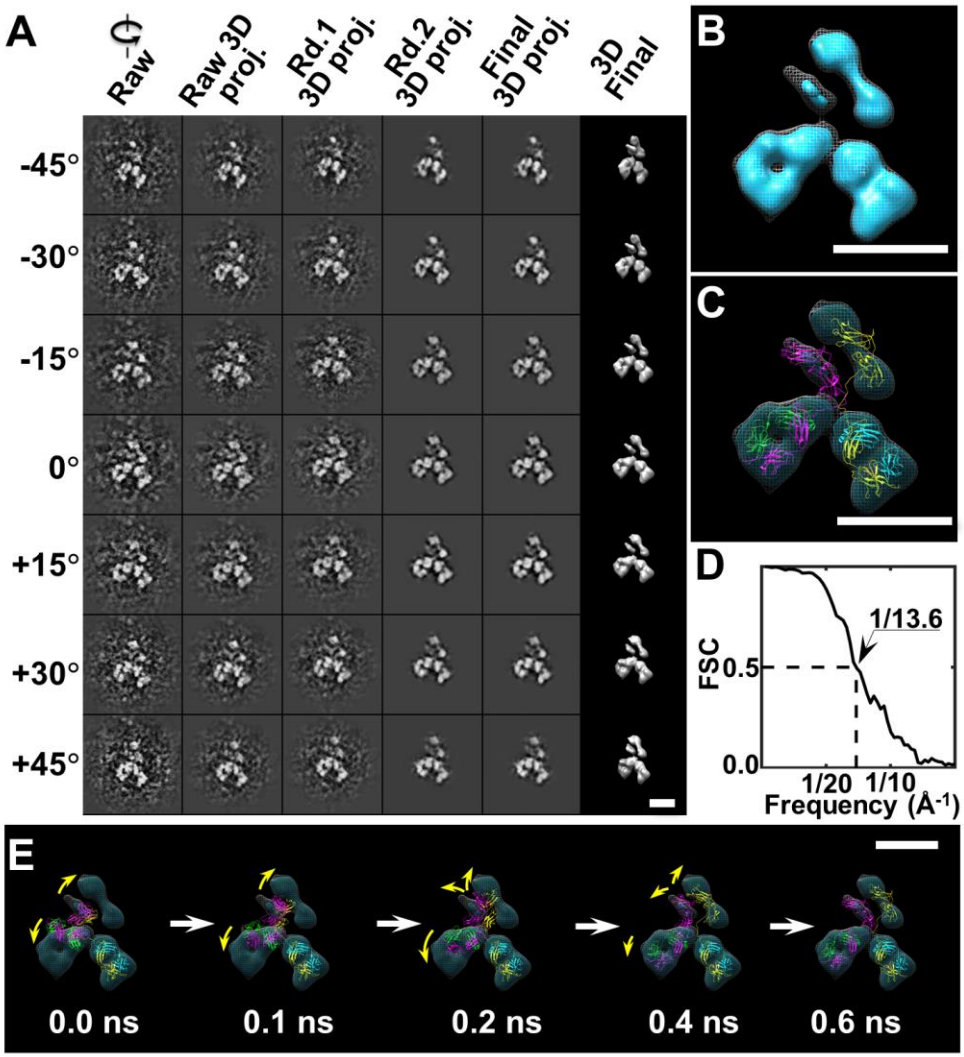

Supplementary Fig. 34 | 3D IPET reconstruction of the 23rd X-shaped IgG homodimer by IPET. (A) Seven representative tilt images of an individual X-shaped particle are displayed in the first column from the left. Using IPET, the tilt images (after CTF correction) were gradually aligned to a common center for 3D reconstruction via iterative refinement. Projections of raw, intermediate and final 3D reconstructions at the corresponding tilt angles are displayed in the next five columns according to their corresponding tilt angles. **(B)** The final 3D density map. **(C)** The density map was flexibly docked with IgG crystal structure by using TMD simulation. **(D)** FSC analyses (from two density maps reconstructed from odd and even numbers of tilt images) showed that the resolution of the final 3D density map was ~13.6 Å. **(E)** Five snapshots illustrated the conformational changes of IgG model during TMD simulation. Scale bars=10 nm.

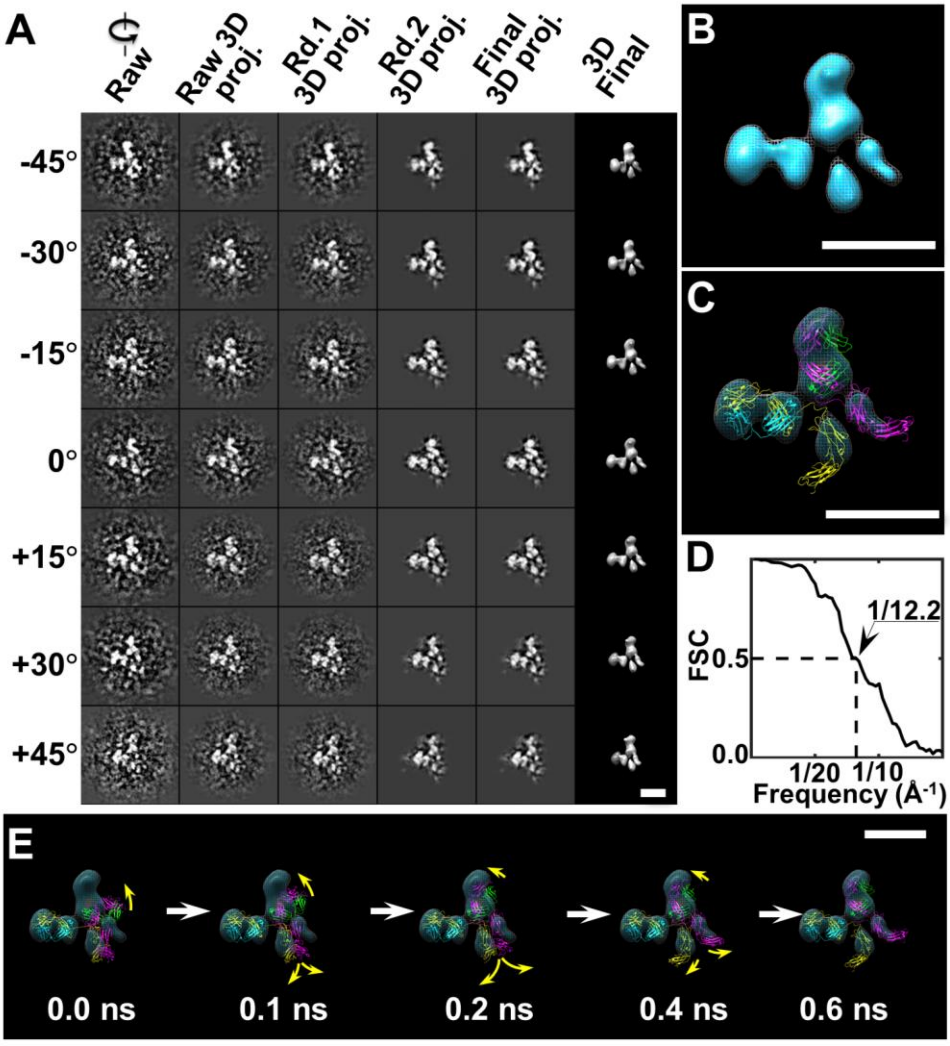

Supplementary Fig. 35 | 3D IPET reconstruction of the 24th X-shaped IgG homodimer by IPET. (A) Seven representative tilt images of an individual X-shaped particle are displayed in the first column from the left. Using IPET, the tilt images (after CTF correction) were gradually aligned to a common center for 3D reconstruction via iterative refinement. Projections of raw, intermediate and final 3D reconstructions at the corresponding tilt angles are displayed in the next five columns according to their corresponding tilt angles. **(B)** The final 3D density map. **(C)** The density map was flexibly docked with IgG crystal structure by using TMD simulation. **(D)** FSC analyses (from two density maps reconstructed from odd and even numbers of tilt images) showed that the resolution of the final 3D density map was ~12.2 Å. **(E)** Five snapshots illustrated the conformational changes of IgG model during TMD simulation. Scale bars=10 nm.

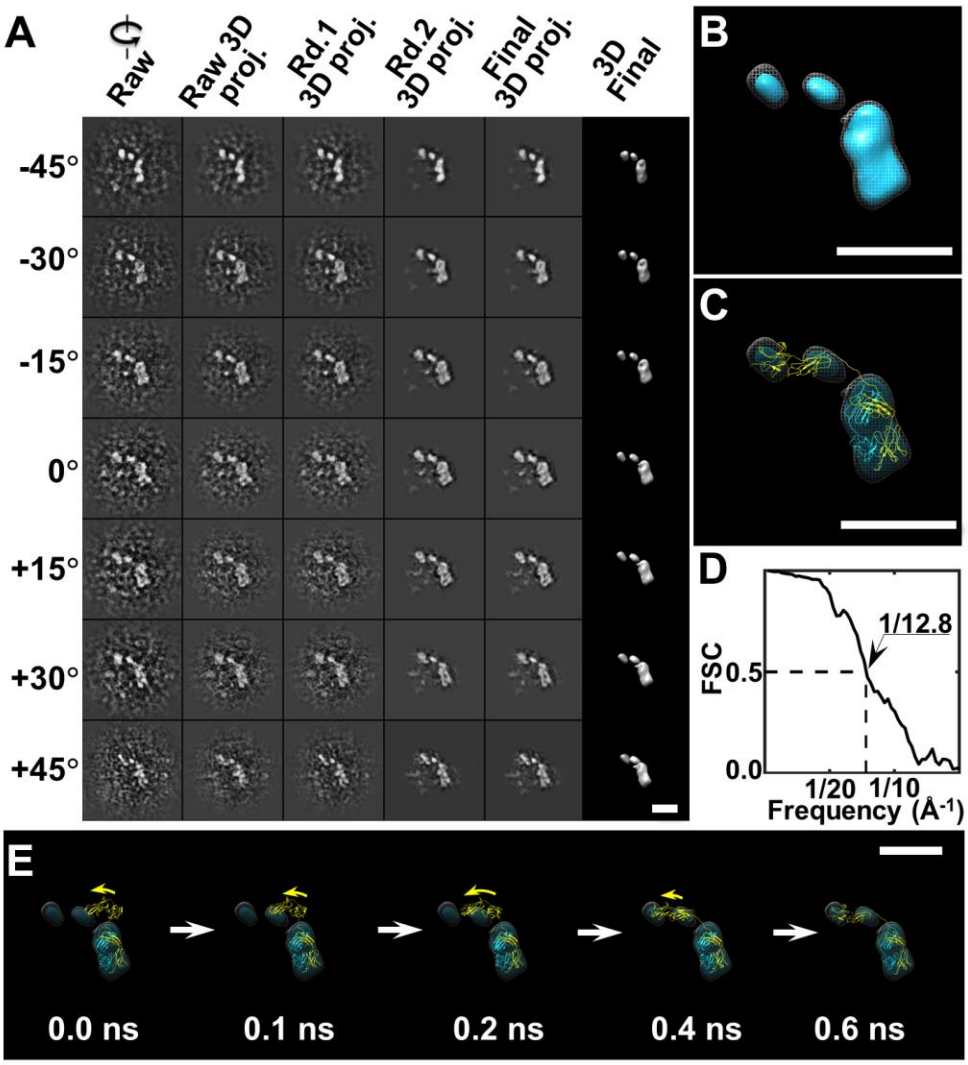

Supplementary Fig. 36 | 3D IPET reconstruction of the first i-shaped half-IgG by IPET. (A) Seven representative tilt images of an individual i-shaped particle are displayed in the first column from the left. Using IPET, the tilt images (after CTF correction) were gradually aligned to a common center for 3D reconstruction via iterative refinement. Projections of raw, intermediate and final 3D reconstructions at the corresponding tilt angles are displayed in the next five columns according to their corresponding tilt angles. **(B)** The final 3D density map. **(C)** The density map was flexibly docked with IgG crystal structure by using TMD simulation. **(D)** FSC analyses (from two density maps reconstructed from odd and even numbers of tilt images) showed that the resolution of the final 3D density map was ~12.8 Å. **(E)** Five snapshots illustrated the conformational changes of IgG model during TMD simulation. Scale bars=10 nm.

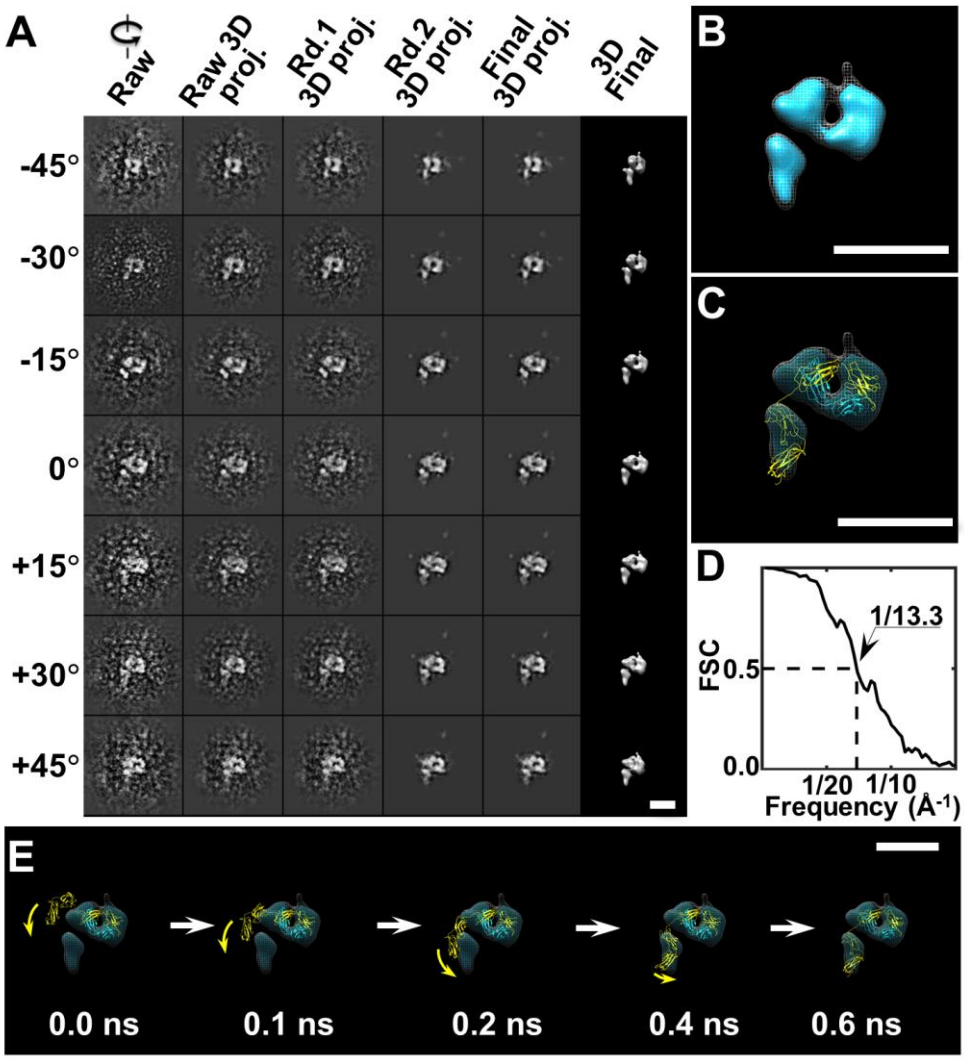

Supplementary Fig. 37 | 3D IPET reconstruction of the second i-shaped half-IgG by IPET. (A) Seven representative tilt images of an individual i-shaped particle are displayed in the first column from the left. Using IPET, the tilt images (after CTF correction) were gradually aligned to a common center for 3D reconstruction via iterative refinement. Projections of raw, intermediate and final 3D reconstructions at the corresponding tilt angles are displayed in the next five columns according to their corresponding tilt angles. **(B)** The final 3D density map. **(C)** The density map was flexibly docked with IgG crystal structure by using TMD simulation. **(D)** FSC analyses (from two density maps reconstructed from odd and even numbers of tilt images) showed that the resolution of the final 3D density map was ~13.3 Å. **(E)** Five snapshots illustrated the conformational changes of IgG model during TMD simulation. Scale bars=10 nm.

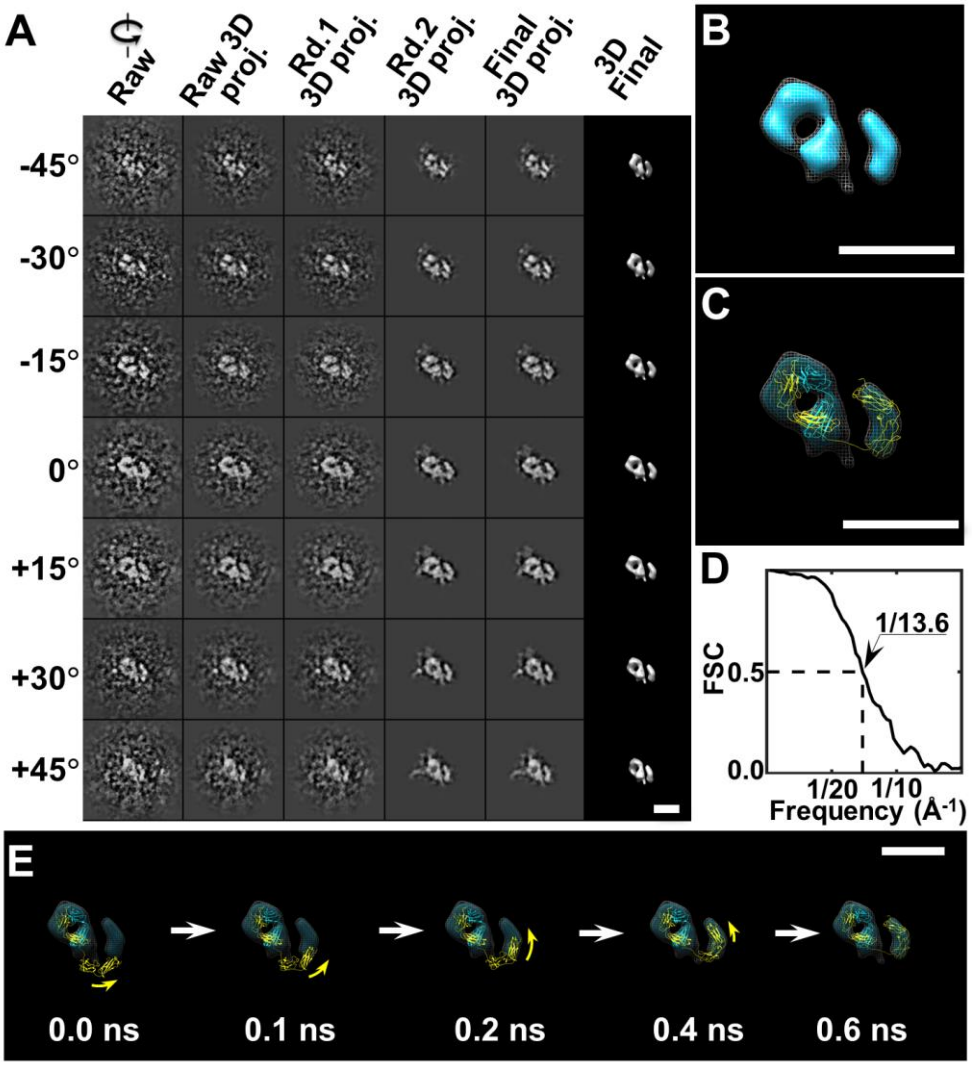

Supplementary Fig. 38 | 3D IPET reconstruction of the third i-shaped half-IgG by IPET. (A) Seven representative tilt images of an individual i-shaped particle are displayed in the first column from the left. Using IPET, the tilt images (after CTF correction) were gradually aligned to a common center for 3D reconstruction via iterative refinement. Projections of raw, intermediate and final 3D reconstructions at the corresponding tilt angles are displayed in the next five columns according to their corresponding tilt angles. **(B)** The final 3D density map. **(C)** The density map was flexibly docked with IgG crystal structure by using TMD simulation. **(D)** FSC analyses (from two density maps reconstructed from odd and even numbers of tilt images) showed that the resolution of the final 3D density map was ~13.6 Å. **(E)** Five snapshots illustrated the conformational changes of IgG model during TMD simulation. Scale bars=10 nm.

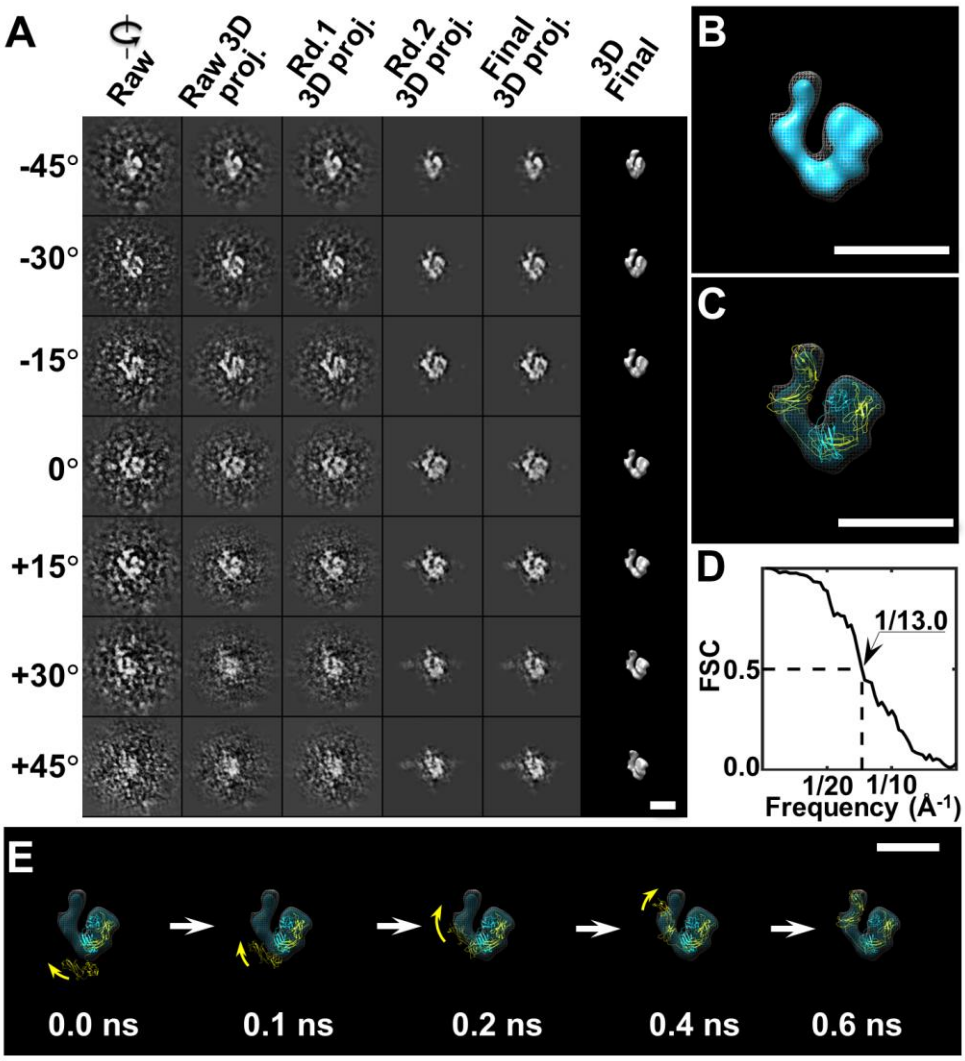

Supplementary Fig. 39 | 3D IPET reconstruction of the forth i-shaped half-IgG by IPET. (A) Seven representative tilt images of an individual i-shaped particle are displayed in the first column from the left. Using IPET, the tilt images (after CTF correction) were gradually aligned to a common center for 3D reconstruction via iterative refinement. Projections of raw, intermediate and final 3D reconstructions at the corresponding tilt angles are displayed in the next five columns according to their corresponding tilt angles. **(B)** The final 3D density map. **(C)** The density map was flexibly docked with IgG crystal structure by using TMD simulation. **(D)** FSC analyses (from two density maps reconstructed from odd and even numbers of tilt images) showed that the resolution of the final 3D density map was ~13.0 Å. **(E)** Five snapshots illustrated the conformational changes of IgG model during TMD simulation. Scale bars=10 nm.

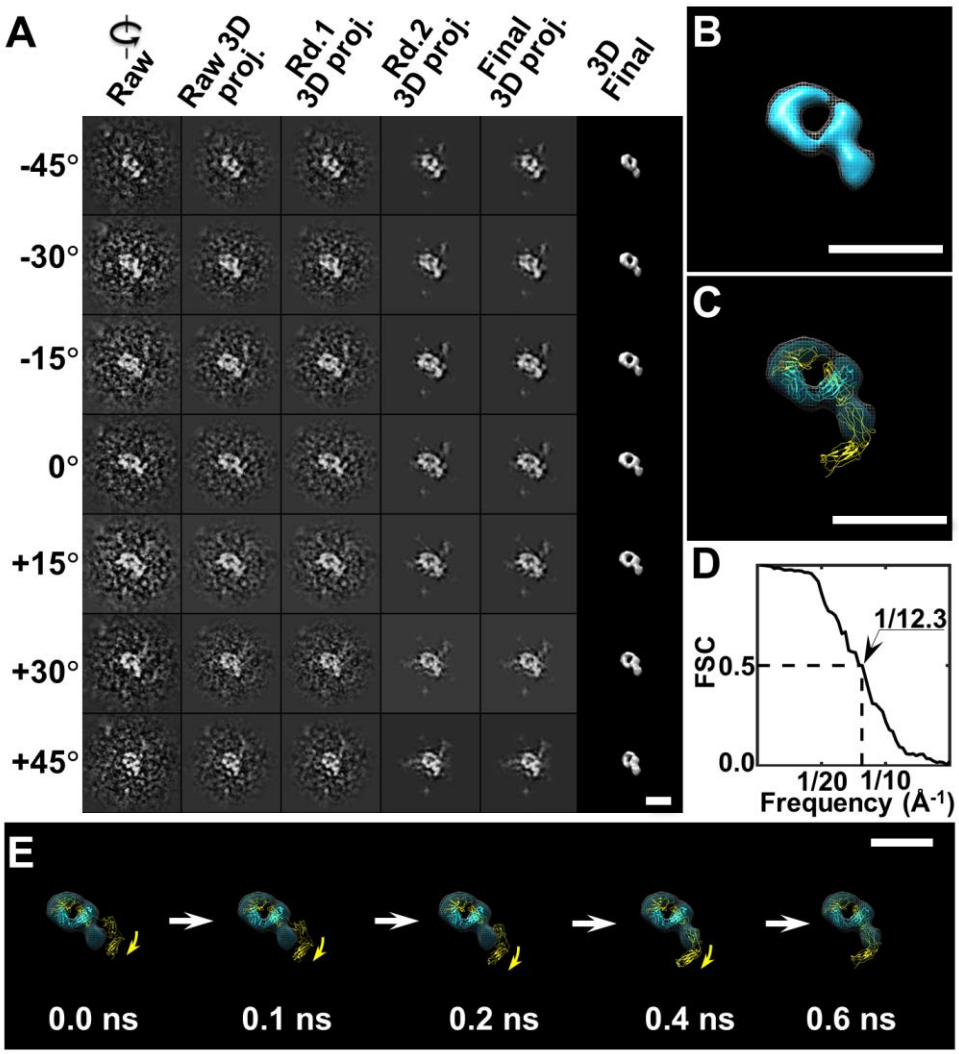

Supplementary Fig. 40 | 3D IPET reconstruction of the fifth i-shaped half-IgG by IPET. (A) Seven representative tilt images of an individual i-shaped particle are displayed in the first column from the left. Using IPET, the tilt images (after CTF correction) were gradually aligned to a common center for 3D reconstruction via iterative refinement. Projections of raw, intermediate and final 3D reconstructions at the corresponding tilt angles are displayed in the next five columns according to their corresponding tilt angles. **(B)** The final 3D density map. **(C)** The density map was flexibly docked with IgG crystal structure by using TMD simulation. **(D)** FSC analyses (from two density maps reconstructed from odd and even numbers of tilt images) showed that the resolution of the final 3D density map was ~12.3 Å. **(E)** Five snapshots illustrated the conformational changes of IgG model during TMD simulation. Scale bars=10 nm.

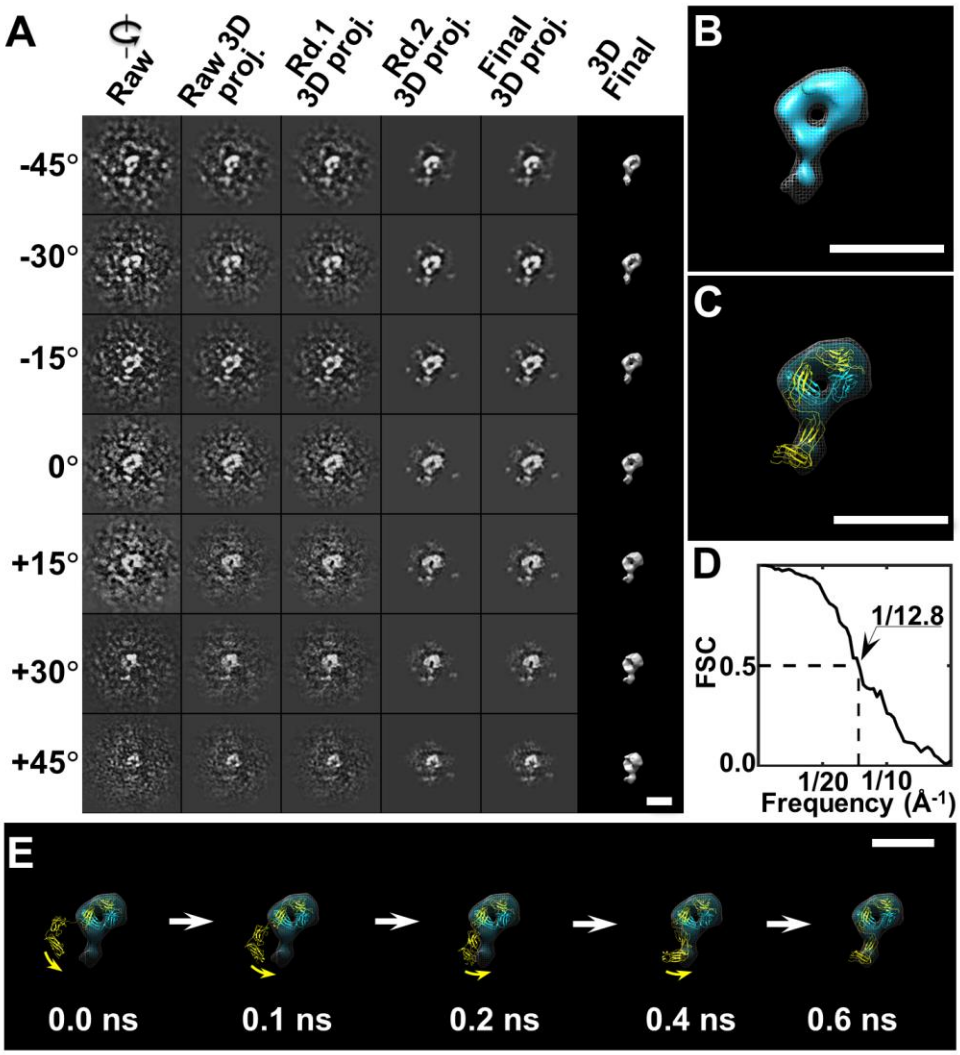

Supplementary Fig. 41 | 3D IPET reconstruction of the sixth i-shaped half-IgG by IPET. (A) Seven representative tilt images of an individual i-shaped particle are displayed in the first column from the left. Using IPET, the tilt images (after CTF correction) were gradually aligned to a common center for 3D reconstruction via iterative refinement. Projections of raw, intermediate and final 3D reconstructions at the corresponding tilt angles are displayed in the next five columns according to their corresponding tilt angles. **(B)** The final 3D density map. **(C)** The density map was flexibly docked with IgG crystal structure by using TMD simulation. **(D)** FSC analyses (from two density maps reconstructed from odd and even numbers of tilt images) showed that the resolution of the final 3D density map was ~12.8 Å. **(E)** Five snapshots illustrated the conformational changes of IgG model during TMD simulation. Scale bars=10 nm.

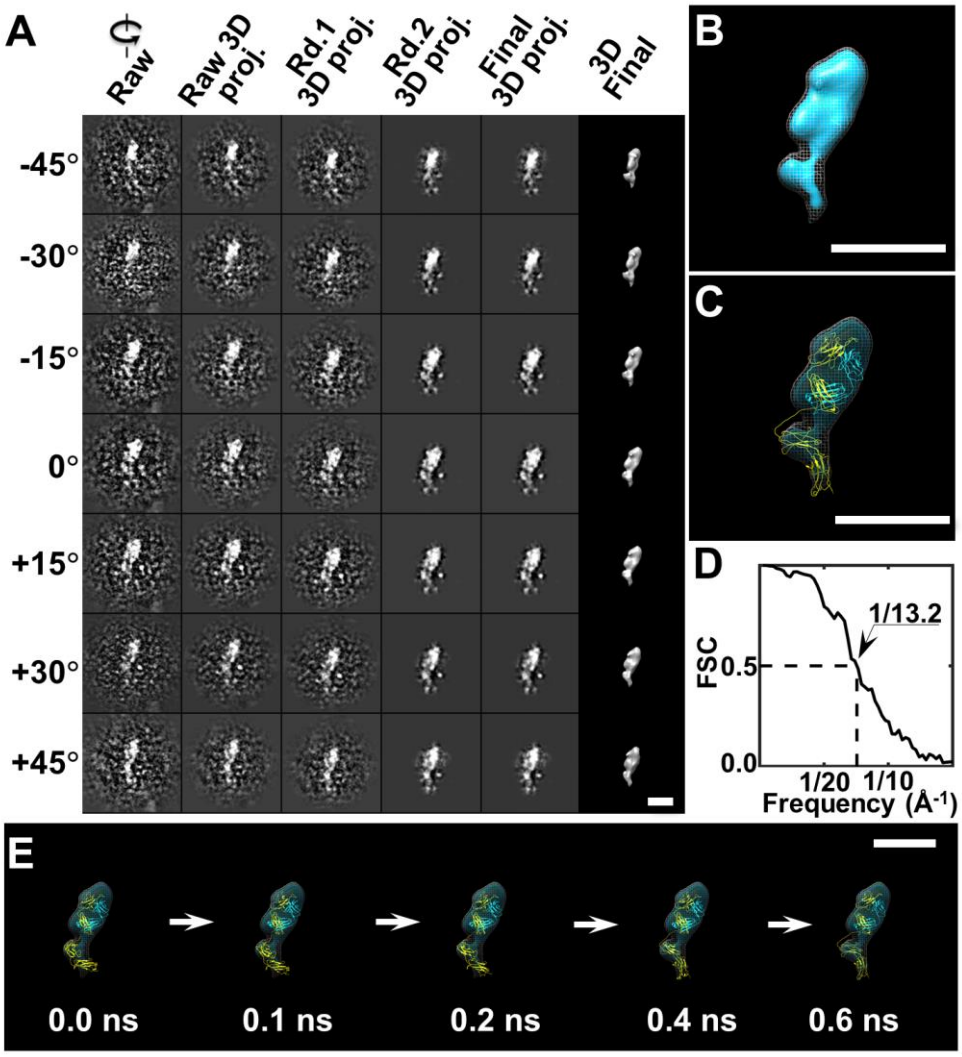

Supplementary Fig. 42 | 3D IPET reconstruction of the seventh i-shaped half-IgG by IPET. (A) Seven representative tilt images of an individual i-shaped particle are displayed in the first column from the left. Using IPET, the tilt images (after CTF correction) were gradually aligned to a common center for 3D reconstruction via iterative refinement. Projections of raw, intermediate and final 3D reconstructions at the corresponding tilt angles are displayed in the next five columns according to their corresponding tilt angles. **(B)** The final 3D density map. **(C)** The density map was flexibly docked with IgG crystal structure by using TMD simulation. **(D)** FSC analyses (from two density maps reconstructed from odd and even numbers of tilt images) showed that the resolution of the final 3D density map was ~13.2 Å. **(E)** Five snapshots illustrated the conformational changes of IgG model during TMD simulation. Scale bars=10 nm.

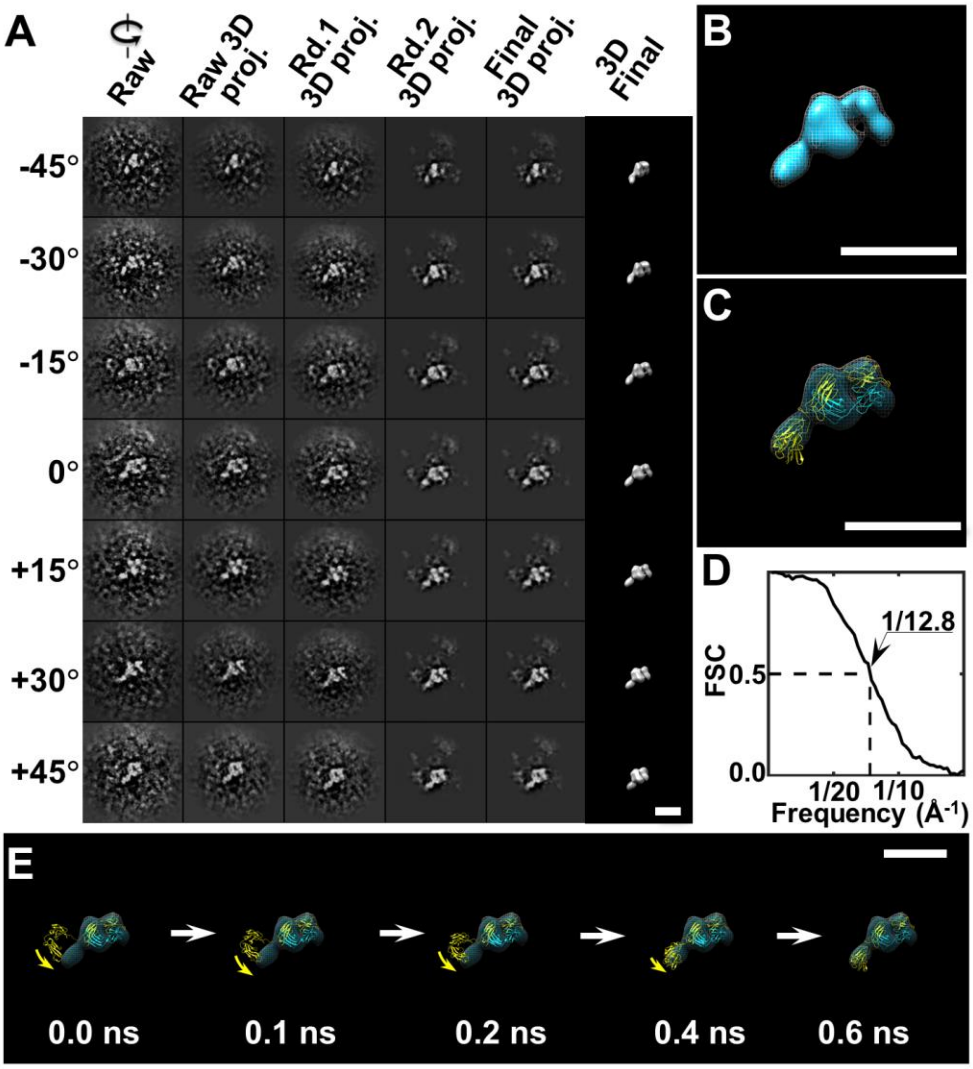

Supplementary Fig. 43 | 3D IPET reconstruction of the eighth i-shaped half-IgG by IPET. (A) Seven representative tilt images of an individual i-shaped particle are displayed in the first column from the left. Using IPET, the tilt images (after CTF correction) were gradually aligned to a common center for 3D reconstruction via iterative refinement. Projections of raw, intermediate and final 3D reconstructions at the corresponding tilt angles are displayed in the next five columns according to their corresponding tilt angles. **(B)** The final 3D density map. **(C)** The density map was flexibly docked with IgG crystal structure by using TMD simulation. **(D)** FSC analyses (from two density maps reconstructed from odd and even numbers of tilt images) showed that the resolution of the final 3D density map was ~12.8 Å. **(E)** Five snapshots illustrated the conformational changes of IgG model during TMD simulation. Scale bars=10 nm.

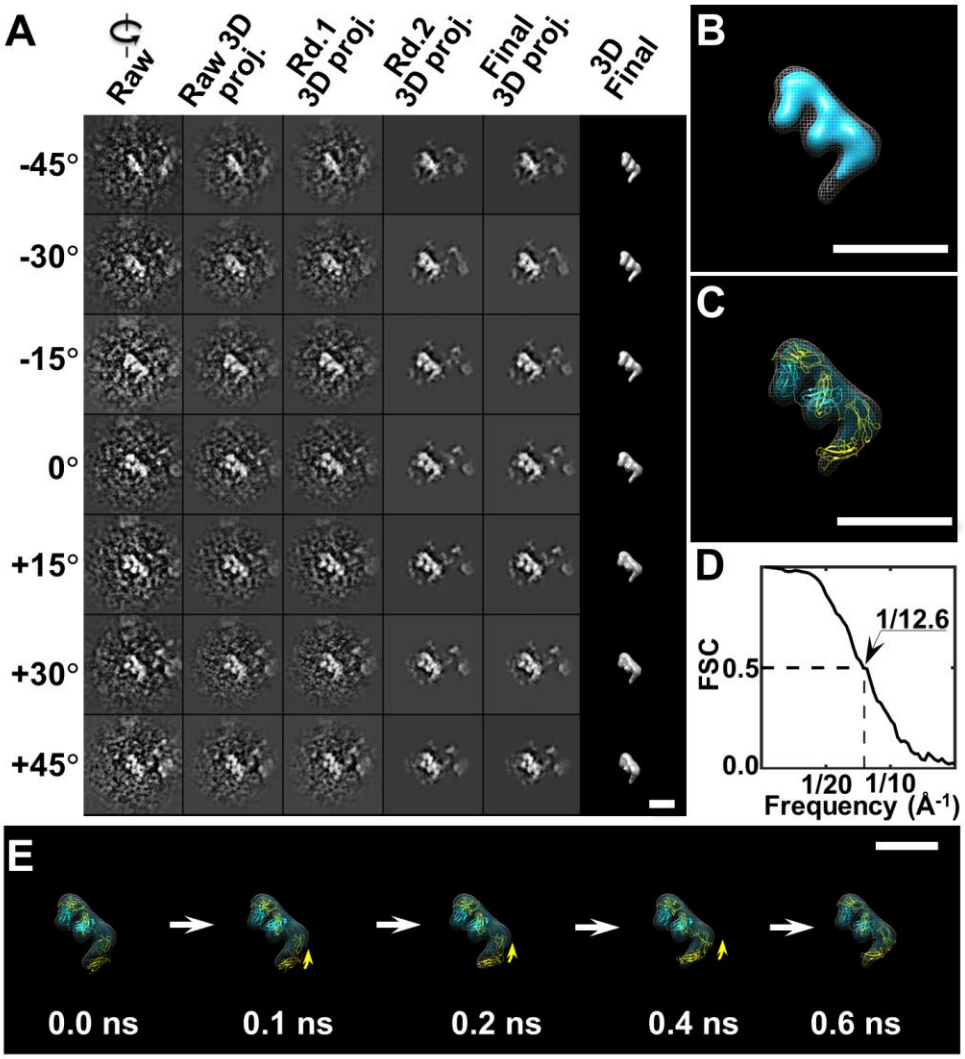

Supplementary Fig. 44 | 3D IPET reconstruction of the ninth i-shaped half-IgG by IPET. (A) Seven representative tilt images of an individual i-shaped particle are displayed in the first column from the left. Using IPET, the tilt images (after CTF correction) were gradually aligned to a common center for 3D reconstruction via iterative refinement. Projections of raw, intermediate and final 3D reconstructions at the corresponding tilt angles are displayed in the next five columns according to their corresponding tilt angles. **(B)** The final 3D density map. **(C)** The density map was flexibly docked with IgG crystal structure by using TMD simulation. **(D)** FSC analyses (from two density maps reconstructed from odd and even numbers of tilt images) showed that the resolution of the final 3D density map was ~12.6 Å. **(E)** Five snapshots illustrated the conformational changes of IgG model during TMD simulation. Scale bars=10 nm.

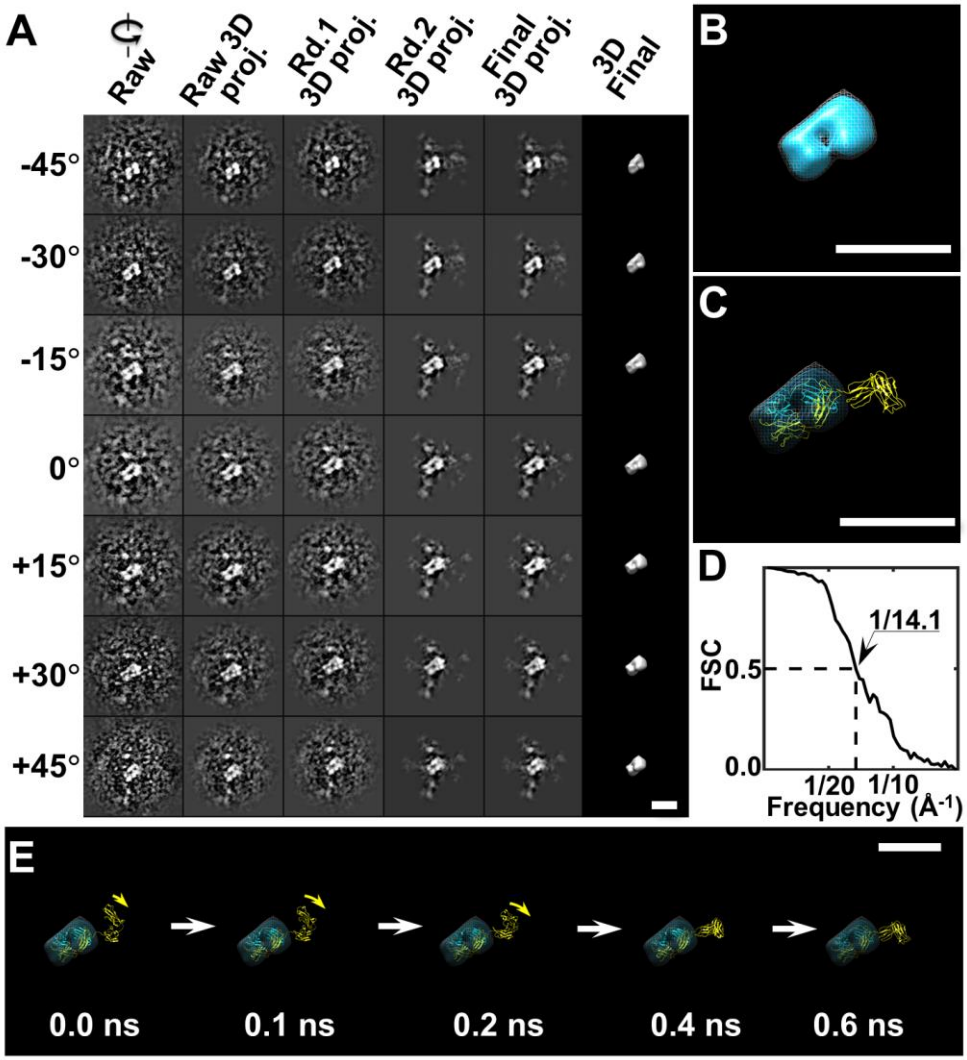

Supplementary Fig. 45 | 3D IPET reconstruction of the tenth i-shaped half-IgG by IPET. (A) Seven representative tilt images of an individual i-shaped particle are displayed in the first column from the left. Using IPET, the tilt images (after CTF correction) were gradually aligned to a common center for 3D reconstruction via iterative refinement. Projections of raw, intermediate and final 3D reconstructions at the corresponding tilt angles are displayed in the next five columns according to their corresponding tilt angles. **(B)** The final 3D density map. **(C)** The density map was flexibly docked with IgG crystal structure by using TMD simulation. **(D)** FSC analyses (from two density maps reconstructed from odd and even numbers of tilt images) showed that the resolution of the final 3D density map was ~14.1 Å. **(E)** Five snapshots illustrated the conformational changes of IgG model during TMD simulation. Scale bars=10 nm.

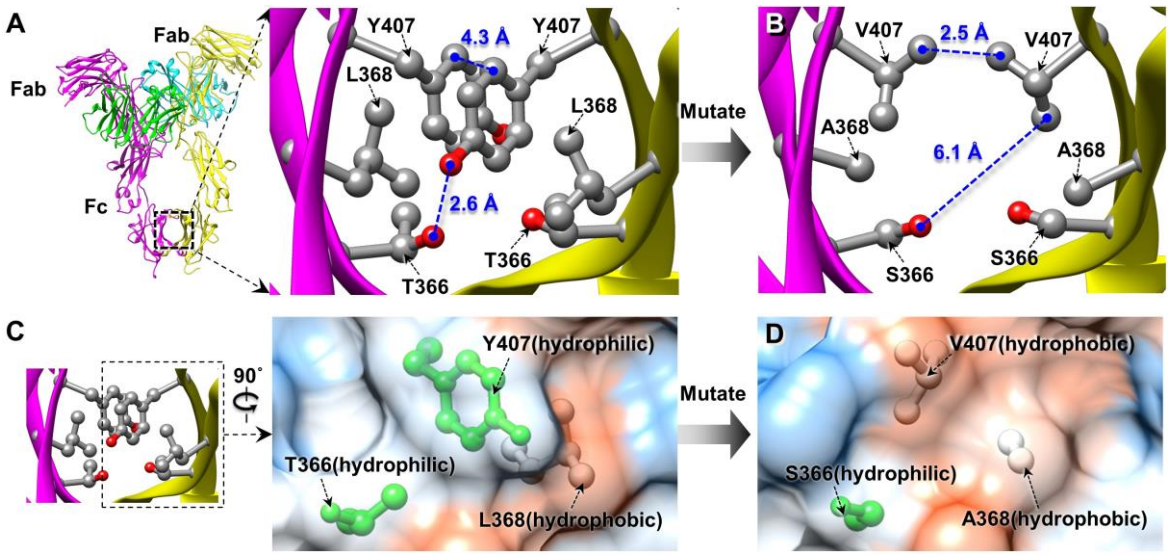

Supplementary Fig. 46 | The structural basis of CH_3-CH_3 interactions. (A) Overall view of the crystal structure of a native IgG (left, PDB entry 1HZH) and zoom-in view of the interface between two CH_3 domains (right). Residues T366, L368 and Y407, which are involved in hole mutations, are shown as ball-and-stick models and colored by element using Chimera. The protein is in ribbon representation, with heavy chains in yellow and magenta and light chains in cyan and green. **(B)** Zoom-in view of the interface between two CH_3 domains of a homology model of IgG homodimer (constructed based on crystal structures of normal IgG, and F_c fragments with hole mutations (PDB entry 1HZH and 4NQT); see Methods.) **(C)** Interface between two CH_3 domains of normal IgG (left) and zoom-in view of the protein surface near residues T366, L368 and Y407 (right). In the zoom-in view, residues T366, L368 and Y407 are shown as ball-and-stick models with hydrophobic residues in white and hydrophilic residues in green. Protein is shown as a transparent surface with most hydrophobic areas in orange and most hydrophilic areas in blue. **(D)** Hydrophobicity of the protein surface near residues S366, A368 and V407 with hole mutations.

Supplementary Video 1 | IPET 3D reconstruction and modeling of an individual X-shaped particle.